



UNIVERSIDADE FEDERAL DO RIO DE JANEIRO
INSTITUTO DE FÍSICA

**Quantum light-matter interactions in
low-dimensional materials**

Yuri Muniz de Souza

Tese de Doutorado apresentada ao Programa de Pós-Graduação em Física do Instituto de Física da Universidade Federal do Rio de Janeiro - UFRJ, como parte dos requisitos necessários à obtenção do título de Doutor em Ciências (Física).

Orientador: Carlos Farina de Souza

**Co-orientador: Wilton Júnior de Melo
Kort-Kamp**

Rio de Janeiro

Abril de 2021

Abstract

Quantum light-matter interactions in low-dimensional materials

Yuri Muniz de Souza

Advisor: Carlos Farina de Souza

Co-advisor: Wilton Júnior de Melo Kort-Kamp

In this thesis we investigate the two-quanta spontaneous emission (TQSE) phenomenon and the Casimir effect in low-dimensional materials. The first two chapters are dedicated to the theoretical study of one- and two-quanta spontaneous emission and the Purcell effect, including some applications that prepare the reader to better understand the subsequent discussion of TQSE near two-dimensional plasmonic materials. Chapter 3 is dedicated to the proposal of novel material platforms to harness the two-quanta decay and emission spectrum of a quantum emitter. First, we consider carbon nanotubes and graphene coated wires. We show how the efficient plasmon-emitter coupling offered by these systems substantially enhance the TQSE in the near-field through the plasmon-plasmon decay channel. We then investigate the TQSE in atomically thin plasmonic nanostructures, which not only provide an extreme enhancement of the decay rate of a quantum emitter, but also efficient generation of entangled photons and frequency selection due to the finite size of the materials. In chapter 4 we start the discussion of the Casimir effect, presenting its general theory and well-known applications. In chapter 5 we introduce topological insulators as excellent systems to achieve tunable Casimir forces, including changing its sign. We then consider the Casimir effect between graphene fam-

ily materials and show how their topological features, together with the quantum Hall effect, enable fine control of the force with external agents. We end the thesis with the conclusions and final remarks.

Keywords: Spontaneous emission, Purcell effect, Two-photon spontaneous emission, entangled photons, Plasmonics, two-dimensional materials, Graphene, Carbon nanotubes, Nanowires, Atomically thin nanostructures, Casimir effect, Lifshitz formula, Quantum Hall effect, Topological insulators, Graphene family materials, Casimir physics in the flatland.

Agradecimentos

Tomei a decisão de começar a escrita da tese pelos agradecimentos. Tenho duas razões para isso. A primeira é o fato de eu não ter escrito uma seção de agradecimentos em minha dissertação de mestrado. Isso pois, na época, fiquei um pouco tímido de registrar alguns detalhes de minhas relações pessoais em um documento público. Além disso, também senti receio de não ser capaz de me expressar da melhor forma e ser injusto com pessoas importantes para mim. A segunda razão é que minha vida mudou drasticamente de 2018 para cá, e algumas pessoas tiveram um impacto tão grande em minha vida desde então que me sinto na obrigação de formalizar esses agradecimentos ao concluir meu doutorado. Bom, vamos ao que interessa. “Senta que lá vem história”!

Dizem por aí que a família desempenha um papel crucial na formação de um indivíduo. E é claro que comigo não seria diferente. Sou extremamente grato a minha mãe Lucilene de Moraes que, mesmo diante das dificuldades, fez questão de me permitir focar exclusivamente em meus estudos e buscar atingir meus sonhos. Também sou grato a meu pai João Marcos por ter plantado em mim a semente da curiosidade, essencial para todo cientista. Como morei durante 15 anos junto a meus tios e primos, todos também foram muito importantes para meu desenvolvimento pessoal. Com certeza a vida durante a graduação, mestrado e doutorado teria sido bem mais sem graça não fosse os churrasquinhos frequentes aos fins de semana e histórias e piadas engraçadas da tia Zilda, que acredito não serem apropriadas para contar aqui. Também tenho familiares muito queridos fora de casa, os quais eu agradeço imensamente pela amizade. Meus tios Rita e Antonio e meu primo Rodrigo são pessoas fantásticas e, apesar da distância e ausência de contato no dia a dia, sempre fui muito bem recebido e acolhido em seu lar.

Também não poderia deixar de mencionar uma pessoa muito especial da família: minha avó Dulcinéa de Moraes. Não é exagero dizer que minha avó foi a pessoa mais importante na minha vida. Desde criança sempre fomos muito próximos e, digamos que eu também era um neto bastante mimado por ela. Mas aos meus 9 anos de idade, após um momento de dificuldade vivido pela minha mãe, minha avó abriu as portas de sua casa e nos acolheu. Minha avó contribuiu para minha educação dentro de casa, para meus estudos, para minha alimentação, para meu lazer, para toda a minha existência como ser humano. Além disso, era extremamente atenciosa e compreensiva. Quando comecei a me interessar por física, nós assistíamos “Cosmos” e “O Universo” juntos pela televisão. Quando trouxe a notícia de que cursaria física na UFRJ, me parabenizou e ficou nitidamente feliz. Enquanto estava na graduação, minha avó, que infelizmente não teve a mesma oportunidade de estudar, me perguntava como eram as aulas, os professores, as pessoas e o que eu havia aprendido. Adorava perguntar sobre o universo, as estrelas e também sobre partículas e essa tal da mecânica quântica. E claro que eu adorava passar horas tentando explicar o que entendia na época. Além de me ouvir, minha avó também falava dela e de seus pensamentos sobre o mundo, o que foi muito importante para meu desenvolvimento pessoal. Infelizmente, minha avó faleceu em 2015, um ano antes de eu concluir minha graduação. Mas tenho certeza que, onde quer que esteja, está em paz e tranquilidade, além de orgulhosa por seu neto concluir o doutorado, estar feliz e com saúde, que ela me ensinou ser o mais importante. Deixo registrado aqui meus agradecimentos a minha avó, por tudo que fez por mim.

Minha trajetória foi repleta de amigos fantásticos com quem compartilhei grandes momentos. Desde amigos de longa data como Christopher, Daniel, Flávio, Roberto e Wallace, os quais agradeço pela grande amizade, como também os parceiros da “Exekillte”, Higor, Carlos e Igor. Na universidade, devo agradecimentos a todos os amigos com quem estudei e aprendi tanto nesses anos: Tiago, Lucas, Ramon, Ilusca, Davi, Luis, Isadora, Arthur, Vinicius, Arouca, Patrícia, Marcíus, Larissa, e a lista poderia continuar. Fora os

amigos do grupo de pesquisa em fenômenos do vácuo quântico, que contribuíram muito para minha evolução como cientista. Além de amigos maravilhosos, também tive aula com os melhores professores que alguém poderia desejar. Agradeço ao grande mestre Jedi Anibal, por suas aulas simplesmente impecáveis e ao Marcus Venicius por ter me permitido enxergar a matemática com outros olhos. Diria que seu curso de álgebra linear fez com que o significado de tudo que estudei até hoje se tornasse mais claro e transparente. A professora Malena, com quem aprendi da melhor forma possível o tema que me motivou a estudar física, a mecânica quântica. Também agradeço aos professores Maurício, Ribamar, Clóvis, Zarro, Marcelo, Felipe e Rodrigo por seus excelentes cursos e pela atenção dada aos alunos. E não poderia me esquecer de agradecer meus professores do ensino médio, Leonardo e Fabiano. Ambos desempenharam um papel fundamental na minha decisão de estudar física na graduação.

Um professor que não poderia faltar nesses agradecimentos é meu próprio orientador, Carlos Farina. É até difícil sintetizar em poucas palavras o tamanho de sua influência e impacto em minha vida. A começar pelas belíssimas aulas e a facilidade com que explica problemas tão complexos de forma tão simples. Seu jeito de pensar a física e interpretá-la me fascinou desde as primeiras aulas de mecânica clássica, e não por acaso o pedi para me orientar. Como orientador, foi muito além de propor projetos e esclarecer dúvidas de física. Farina me proporcionou diversas experiências de ensino e pesquisa, dentro e fora da universidade, tanto no Brasil como no exterior. Nunca me esquecerei do que disse após eu o agradecer por ter me ajudado a participar de um congresso ainda na graduação: “está tranquilo meu camarada, apenas faça o mesmo para seus alunos no futuro”. Percebi rapidamente que Farina é benevolente para todas as pessoas ao seu redor, é alguém que se importa com seus alunos não somente no âmbito profissional, mas também pessoal. Mesmo quando o comuniquei que não me sentia mais feliz na academia e eventualmente decidi seguir outro caminho, Farina me deu apoio e continuou me orientando no doutorado da melhor forma possível, como faria com qualquer outro aluno. Por tudo isso, deixo aqui

meus mais sinceros agradecimentos. Também gostaria de agradecer meu co-orientador, Wilton Kort-Kamp, pela enorme dedicação e atenção necessária no andamento de meu mestrado e doutorado e nos trabalhos relacionados. Também o agradeço pela maravilhosa recepção durante minha curta passagem por Los Alamos, pois minha experiência longe de casa não teria sido tão agradável sem alguém para dar aquelas dicas de passeio e me salvar nos momentos de dificuldade (a famosa história do *overbooking!*). E por falar em experiências fora de casa, agradeço ao Diego Dalvit pelas discussões de física calorosas em Los Alamos e ao Luis Martín Moreno pela gentileza de receber eu, Farina e Patrícia na universidade de Saragoça, além da boa vontade e atenção que gerou ótimos frutos em nossa recente colaboração. Também gostaria de agradecer meus primeiros orientadores de iniciação científica, Nelson Velho e Ginette Jalbert, por me possibilitarem um primeiro contato com pesquisa já no segundo ano da graduação e não me deixarem esquecer que física não é somente uma disciplina teórica, mas uma ciência empírica.

Por último, mas não menos importante, gostaria de agradecer a minha amada noiva Leticia Cabanas. Obrigado por me proporcionar tantos momentos de alegria e descontração desde que nos conhecemos em 2015. Pelos passeios, os quais tenho certeza que não teria feito sem você, e também pelas aventuras gastronômicas. Finalmente, obrigado por todo apoio e suporte emocional nessa longa jornada de 9 anos de física, principalmente nos momentos mais difíceis e de reflexão. Foram nesses momentos mais críticos que entendi a importância de estar próximo das pessoas queridas e de um relacionamento pautado na amizade e companheirismo.

Contents

Summary	viii
List of Figures	xii
Introduction	xix
1 Spontaneous emission and the Purcell effect	1
1.1 One-photon spontaneous emission theory	2
1.1.1 One-photon spontaneous emission in free-space	3
1.1.2 Purcell effect: Field modes approach	4
1.1.3 An atom close to a perfect mirror	6
1.1.4 An emitter between two perfect mirrors	9
1.2 Green's tensor formalism	11
1.2.1 Theoretical framework	12
1.2.2 An emitter near a semi-infinite dispersive medium	14
2 Two-quanta spontaneous emission	19
2.1 Two-photon spontaneous emission in free-space	20
2.1.1 On the numerical evaluation of TQSE	21
2.1.2 On the TQSE selection rules	24
2.1.3 Resonant TQSE	25
2.1.4 Beyond hydrogenic atoms	25

2.2	Field modes approach	26
2.2.1	TPSE near a perfectly conducting plate	27
2.2.2	TPSE of an emitter between two perfect mirrors	30
2.3	Green's function approach	33
2.3.1	Green's function approach to the emitter-mirror system	34
2.4	The Purcell factors relation	35
2.4.1	An emitter near a half-space dielectric medium	36
3	Two-quanta spontaneous emission in low-dimensional plasmonic materials	38
3.1	Tunable two-quanta spontaneous emission with graphene	40
3.1.1	Graphene Fresnel coefficients and Purcell factors	41
3.1.2	Two-plasmon spontaneous emission	43
3.2	Two-plasmon spontaneous emission in one-dimensional carbon nanostructures	45
3.2.1	Quasi-static approximation modelling	45
3.2.2	Two-plasmon spontaneous emission near carbon nanotubes	49
3.2.3	Two-plasmon spontaneous emission in graphene coated wires	53
3.3	Two-photon spontaneous emission in two-dimensional plasmonic nanostructures	57
3.3.1	Plasmon wave function formalism	58
3.3.2	Purcell factors and spectral lineshapes	62
3.3.3	Two-photon spontaneous emission near a two-dimensional silver nanodisk	68
3.3.4	Two-photon spontaneous emission near a two-dimensional graphene nanodisk	71

4 The Casimir effect	75
4.1 Casimir force between two perfect mirrors	77
4.2 Lifshitz formula	79
4.2.1 Scattering approach for the zero-temperature Casimir effect	79
4.2.2 Wick rotation	82
4.2.3 Finite temperature Casimir energy	83
5 Casimir effect in the flatland	86
5.1 Casimir forces between graphene sheets	87
5.1.1 Repulsive quantized Casimir force with graphene	88
5.2 Casimir effect in graphene family materials	92
5.2.1 Topological phase transitions in the Casimir force	93
5.2.2 Interplay between photo-induced phase transitions and quantum Hall physics in the Casimir effect	97
5.2.3 Thermal effects in the graphene family Casimir forces	104
6 Conclusions and final remarks	108
A Plasmon wave functions of a nanodisk	136
B List of publications during Ph. D. thesis work	140

List of Figures

1.1	Schematics of an atom placed a distance z from a perfectly conducting plane.	6
1.2	Normalized SE rates of a quantum emitter close to a perfectly conducting plate as a function of the distance.	8
1.3	An atom between two perfectly conducting plates separated by a distance L .	9
1.4	Normalized SE rates of a quantum emitter placed exactly in the middle ($z = L/2$) of two perfectly conducting plates as a function of the distance between them.	10
1.5	Schematics of a point electric dipole of magnitude \mathbf{p} oscillating with frequency ω and placed at \mathbf{r}' with respect to the origin \mathcal{O} . For a given position \mathbf{r} , the dipole produces an electric field given by $\mathbf{E}(\mathbf{r})$	14
1.6	Normalized SE rates of a quantum emitter near a semi-infinite near a half-space Polystyrene medium as a function of distance. The Polystyrene resonance frequencies are given by $\omega_{R1} = 5.54 \times 10^{14}$ rad/s and $\omega_{R2} = 1.35 \times 10^{16}$ rad/s and the corresponding relaxation time by $\tau = 10^{-11}s^{-1}$ [1]. The emitter transition frequency was chosen as $\omega_{R2}/5$	18
2.1	γ_0 multiplied by a normalization constant as a function of the normalized frequency of emission. We considered a three-level system with intermediate transition frequency $\omega_{mf} = 3\omega_{if}/2$	22

2.2	Spectral density function $\gamma(\omega; z)$ of an emitter near a perfect mirror in terms of the dimensionless variable ω/ω_t for three different values of z . We also plot the spectral density function in free space (solid line).	28
2.3	Spectral enhancement $\gamma(\omega; z)/\gamma_0(\omega)$ of an emitter near a perfect mirror as a function of the separation distance z for three given frequencies.	29
2.4	Spectral enhancement of an emitter equidistant from two perfect mirrors as a function of ω/ω_t for three given values of L	31
2.5	Spectral enhancement in terms of the dimensionless variable $k_t L / \pi$ with the emitter equidistant to both mirrors for three given frequencies.	32
2.6	Spectral enhancement of an emitter near a half-space Polystyrene medium as a function of ω/ω_t for three given values of z . The Polystyrene resonance frequencies are given by $\omega_{R1} = 5.54 \times 10^{14}$ rad/s and $\omega_{R2} = 1.35 \times 10^{16}$ rad/s and the corresponding relaxation time by $\tau = 10^{-11} s^{-1}$ [1]. The emitter transition frequency was chosen as $3\omega_{R2}$	37
3.1	(a) Isotropic Purcell factor $P_{iso} = (P_x + P_y + P_z)/3$ of a quantum emitter placed a distance $z = 10$ nm from a suspended graphene sheet as a function of its transition energy. (b) Isotropic Purcell factor as a function of the distance between the emitter and the monolayer. The transition energy is given by the $6s \rightarrow 5p$ transition in hydrogen, $\hbar\omega_t \approx 166$ meV. Both plots were computed considering graphene at room temperature ($T = 300$ K) with an electron mobility of $\mu = 2500$ cm 2 V $^{-1}$ s $^{-1}$	42
3.2	Spectral enhancement of an emitter placed at a distance $z = 10$ nm from a suspended graphene monolayer as a function of ω/ω_t for three given values of E_F . The emitter transition energy was chosen as 166 meV, which corresponds to the $6s \rightarrow 5s$ transition frequency in hydrogen.	44

3.3 Schematics of the system under study. (a) A quantum emitter separated by a distance d from a SWCNT of radius R . (b) A quantum emitter separated by a distance d of a dielectric cylinder of relative electric permittivity ε and radius R , coated with graphene.	46
3.4 (a) Real part of the plasmon's wavevector k_p for the fundamental mode ($n = 0$) normalized by the free-space wavevector $k = \omega/c$ as a function of the light oscillation frequency for different values of the Fermi energy. (b) The ratio between the real and imaginary parts of k_p of the fundamental plasmonic mode versus the free-space frequency for different values of the Fermi energy.	50
3.5 (a) Normalized two-plasmon SE rate for the $6s \rightarrow 5s$ transition in hydrogen ($\hbar\omega_t \approx 166$ meV) as a function of the distance between the emitter and the surface of the SWCNT. Upper right inset: Normalized two-plasmon SE spectral density as a function of distance for three frequencies of emission. In this inset, the Fermi energy is given by $E_F = 1$ eV. Lower left inset: Normalized two-plasmon SE spectral density at $d = 10$ nm. Since only the fundamental plasmonic mode is present, we observe a broadband spectrum of emission without any resonance. The divergences at $\omega = 0$ and $\omega = \omega_t$ are solely due to the normalization by the free-space spectral density, which goes to zero at the boundaries of the spectrum. (b) Quantum efficiency given by Eq. (3.8) of two-plasmon SE for the $6s \rightarrow 5s$ transition in hydrogen as a function of distance. In both plots, $E_F = \{0.25, 0.5, 0.75, 1\}$ eV (dotted blue, dash-dotted purple, dashed green, and solid red lines, respectively)	51

3.6 (a) Dispersion relation for all the plasmonic modes supported with free-space oscillating light of frequency $\hbar\omega < 200$ meV. Each color is associated with a GCW of a different radius, while the linestyle characterize the order of the mode. (b) The ratio between the real and imaginary parts of k_p for each plasmonic mode as a function of frequency. In both plots we choose silicon as the dielectric medium, which has permittivity $\varepsilon = 11.68$ in the frequency range considered. Also, $R = \{20, 30, 42\}$ nm (blue, purple, and green lines, respectively), and the Fermi energy is $E_F = 1$ eV.	53
3.7 (a) Two-plasmon SE spectral density near a silicon ($\varepsilon = 11.68$) nanowire covered with graphene as a function of the wire radius and the frequency of the plasmon normalized by the transition frequency. The transition frequency considered is $\hbar\omega_t \approx 166$ meV. (b) two-plasmon SE spectral density for various dielectric coated nanowires of radius $R = 100$ nm. For $\varepsilon = 7.33$ ($\varepsilon = 15.66$), the minimum excitation frequency of the mode $m = 1$ ($m = 2$) is precisely at $\omega_t/2$, which results in a huge resonance in the middle of the spectrum. In both plots the Fermi energy is $E_F = 1$ eV.	54
3.8 (a) Normalized two-plasmon SE rate for the $6s \rightarrow 5s$ transition in hydrogen as a function of the inner dielectric cylinder permittivity. We choose a nanowire of radius 25 nm and Fermi energies of 0.5 eV (blue solid curve) and 1 eV (red dashed curve). Inset: plasmon dispersion relations for $\varepsilon = 3.11$ (left) and $\varepsilon = 5.15$ (right). (b) Two-plasmon SE rate for the same hydrogen transition as a function of distance. The Fermi energy is equal to 1 eV. Inset: Quantum efficiency (Eq. (3.8)) as a function of distance for the same parameters of the main plot.	56
3.9 Schematics of an atomically thin plasmonic nanostructure of arbitrary shape, size $D \sim \sqrt{A}$, where A is its surface area, and thickness t	58

5.3 Topological phase diagram of graphene family materials. The displayed topological phases are the band insulator (BI), quantum spin Hall insulator (QSHI), polarized-spin quantum Hall insulator (PS-QHI), and anomalous quantum Hall insulator (AQHI).	95
5.4 (a) Schematics of the system under study. Two graphene family monolayers separated by a distance d and subjected to externally applied electric (E_z) and magnetic (B_z) fields, and a circulary polarized laser (Λ); (b) Low-energy band structure of graphene family materials around a given Dirac point. For a non-zero magnetic field, the quantized Landau levels (red circles) are built on top of the Dirac cones.	97
5.5 Casimir energy in the (E_z, Λ) plane for (a) $\mu = \lambda_{SO}$ and $E_B = 1.2\lambda_{SO}$ and (b) $E_B = 0.8\lambda_{SO}$. (c) Normalized Casimir energy in the (E_z, μ) plane for $\Lambda = 0$ and $E_B = \lambda_{SO}$. (d) Normalized Casimir energy as a function of the chemical potential for $\Lambda = 0$. In all plots the distance between the plates is given by $d\lambda_{SO}/\hbar c = 10$ and the dissipation is set to zero.	100
5.6 Casimir energy as a function of the chemical potential of a single monolayer for $\{e\ell E_z, \mu_2\}/\lambda_{SO} = \{(1,0.5), (1,-0.5), (1.5,0.5)\}$ (solid blue, dashed red, and dash-dotted green, respectively) and $E_B = \lambda_{SO}$. For all curves, the distance between the plates is long enough so that Eq. (5.16) is valid and $\Lambda, \Gamma = 0$	102

- 5.7 (a) Long distance approximated expression given by Eq. (5.16) subtracted from the Casimir energy as a function of distance. The chosen parameters are $\Lambda = 0$, $\Gamma = 0$, $e\ell E_z = \lambda_{SO}$, and $\mu = \{0.5, 1.25, 1.5\}\lambda_{SO}$ (solid blue, dashed red, and dash-dotted green lines, respectively). The inset shows the longitudinal and Hall conductivity at frequency $\hbar\xi = 0.01\lambda_{SO}$ as a function of the chemical potential. (b). Casimir energy for $\Lambda = 0$, $e\ell E_z = \lambda_{SO}$, $\mu = 1.25\lambda_{SO}$, and $\hbar\Gamma = \{0, 0.01, 0.02\}\lambda_{SO}$ (solid, dashed, and dash-dotted lines, respectively) as a function of distance. The gray dotted lines are the approximated solutions in the long distance regime, given by the sum of Eqs. (5.16) and (5.19). 103
- 5.8 (a) Dissipationless Casimir energy as a function of temperature for a separation distance of $d\lambda_{SO}/\hbar c = 10$. The dotted lines correspond to the approximated value of the $n = 0$ Matsubara frequency contribution presented in Eq. (5.20). The left inset is a zoom of the plot, showing that each curve goes to its correspondent zero-temperature limit (dashed gray lines). The right inset shows the Casimir force in the region where it becomes attractive. (b) Casimir energy as a function of distance for $k_B T = 10^{-3}\lambda_{SO}$ and $\hbar\Gamma = 0.01\lambda_{SO}$. The gray line corresponds to the $n = 0$ Matsubara contribution (Eq. (5.21)). In both plots, $\Lambda = 0$, $e\ell E_z = \lambda_{SO}$, and $\mu = \{0.5, 1.25, 1.5\}\lambda_{SO}$ (solid blue, dashed red, and dash-dotted green lines, respectively). 105

Introduction

One of the most revolutionary ideas brought by the quantum theory in the beginning of the XX century was that the vacuum plays an important role in various physical phenomena. In quantum electrodynamics (QED), which describes the interaction between matter and radiation in the quantum physics context, the vacuum is characterized by ubiquitous fluctuations of the electromagnetic field and an infinite energy called the vacuum zero point energy [2]. Being considered one of the most successful physical theories, QED provides explanations for a variety of physical phenomena, as for instance the Casimir effect and dispersive forces, the Lamb shift, light absorption and emission, and the electron anomalous magnetic dipole moment [3]. In the latter two cases we have the greatest agreements between theory and experiment in physics up to date [4]. Each of the above mentioned phenomena still challenges physicists nowadays, and each of them could be a subject of extensive research. In this thesis we focused on two very important QED effects, namely, spontaneous emission (SE) and fluctuation induced forces, which we will discuss in the next paragraphs.

SE is the process in which an excited atom (or any other quantum emitter) decays even when isolated from all bodies in the universe and any external influences. This idea was introduced in a seminal work of A. Einstein [5], but fully understood only after the development of the quantum theory of radiation-matter interactions [6]. The quantum theory of matter alone can not explain the SE of an atom since the excited states are stationary states of the Hamiltonian of the system, but not of the total Hamiltonian of the atom-field system. But what is the purpose of studying the spontaneous decay of an

atom if it is already fully described by QED? To uncover the interest of the community on this subject we must first understand that SE is the process responsible for giving birth to most of the light we see. In general, there are only two ways for an excited atom to decay: spontaneously or stimulated by external fields. In a wide variety of situations, such as the visible light emitted by the sun, the SE decay rate is greater than the stimulated emission counterpart [7]. In addition, the lifetime of the emitter is not an intrinsic property. As shown by E. M. Purcell in 1946 [8], the decay rate of a quantum emitter depends on the environment of the emitter's position. This feature opens the possibility of controlling the generation and properties of light by proper choices of materials, geometrical configurations and, in some cases, external agents to modify the allowed electromagnetic field modes in the vicinities of the quantum emitter. Last, but not least, there is a wide variety of SE processes that can be enhanced through the influence of material bodies besides the most common one-photon electric dipole transition. Some of these processes cannot occur in free-space, while others are just negligibly small. As a simple example, an emitter very close to a metal may prefer to decay through the emission of a plasmon due to the strong coupling that these modes offer in the near-field [9]. Another unusual example is the case of multipolar transitions, which for some environments may present emission rates comparable to the usual electric dipole transition [10].

A SE process that has attracted great interest in the last years, and is the main topic of this thesis, is the two-quanta spontaneous emission (TQSE). TQSE is a second-order process in perturbation theory and, therefore, much slower than the one-quantum SE [11]. Despite its small decay rate, TQSE is a very rich phenomenon since it presents a broadband spectrum of emission, which is not the case for one-quantum SE processes due to energy conservation constraints. In the last century, this kind of decay was proved to be the correct explanation for the observed planetary nebulae spectrum [12]. But TQSE is far from being a subject from the past. In the case of two-photon spontaneous emission

(TPSE), it is known that the emitted photons are indistinguishable and entangled in time and frequency [13]. Hence, TPSE has a great potential of finding applications in novel quantum technologies. Furthermore, it has been recently shown that the TQSE can be the dominant decay channel of an emitter despite other existing one-quantum decay pathways [14]. For these reasons, a careful investigation of TQSE in different electromagnetic environments is worth studying and may lead to exciting developments in quantum optics.

Another phenomenon that can be attributed to the vacuum zero point energy is the Casimir effect, which was originally proposed by H. B. G. Casimir in 1948 [15] as the attraction between two parallel perfectly conducting plates. However, it is known that the Casimir effect exists between any material bodies [16, 17]. Essentially, Casimir forces are dispersive forces between two bodies at length scales where electromagnetic retardation becomes relevant. These ever-present interactions are one of the most intriguing kind of intermolecular forces and play an important role not only in different areas of physics, but also in chemistry, biology, and engineering [18]. For instance, dispersive forces are crucial to understand the stability of colloids [19], the drug binding in proteins and the double helix structure of DNA [20], and even the adhesion of geckos to walls [21, 22]. In the manufacturing and operation of devices at the micro- and nanoscales these forces also have severe consequences since they dominate at very small distances and may cause stiction due to their tipically attractive nature [23, 24]. Therefore, it is very important to study dispersive interactions and master their manipulation not only in magnitude but also in sign, i.e., to tune the attractive or repulsive character of the force. In this direction, real materials have shown to support a wealth of different dispersive interactions [25, 26], and the strong development of materials science over the last few decades has given a new impetus to the study of the Casimir force and its possible control [27, 28]. In particular, switching between repulsive and attractive Casimir forces using external agents can be realized with topological insulator plates [29, 30], and superparamagnetic metamamate-

rials [31]. Motivated by the above reasons, we have also dedicated a special attention to this effect.

This thesis is organized as follows: in chapters I and II we present the theory of one- and two-quanta SE and the Purcell effect. In chapter III we consider two particular environments of interest, namely, a carbon nanotube and two-dimensional plasmonic nanostructures. We explain why both systems are interesting for studying two-quanta transitions and describe the results we found in our work. We follow the same template for the Casimir effect chapters. In chapter IV we present the theoretical framework that sustains our further investigations. We then discuss in chapter V the Casimir effect between graphene family materials and show the main results we found when the photoinduced topological properties of these materials are combined with the quantum Hall effect induced by an applied magnetic field. The last chapter is left for the conclusions and final remarks.

Chapter 1

Spontaneous emission and the Purcell effect

In 1916, Einstein wrote a letter to his friend, Michele Besso, saying: “*A splendid light has dawned on me about the absorption and emission of radiation*”. He was referring to the idea that the spontaneous decay of an atom is fundamental to explain the emission spectrum of a black body in thermal equilibrium. This SE, which happens even when the emitter is isolated from all bodies in the universe, is responsible for most of the light we see since its corresponding rate is much greater than the one of stimulated emission in a wide range of temperatures and frequencies [7]. Despite the importance and intriguing character of the phenomenon, it was only in 1927 that a broader understanding of the SE process was established. In his seminal work [6], Paul Dirac derived for the first time an expression for the SE rate of an atom from first principles.

The fact that SE is a ubiquitous decay does not mean that it cannot be influenced by external conditions. Indeed, E. M. Purcell showed in 1946 that the SE rate of an emitter can be affected by its environment [8], and since then this phenomenon is referred to as the Purcell effect. This effect was experimentally verified by the first time by Drexhage, who showed that the lifetime of molecules close to a Ag mirror changed with respect to its value in free-space [32–34]. In extreme situations, the SE of an emitter can be even suppressed by the environment. This was first proposed by Kleppner *et al* for the case

of an atom between two parallel mirrors [35], and experimentally observed later with Rydberg atoms [36]. The pioneer work of Purcell can be considered as the landmark of a field that is called cavity quantum electrodynamics [37–39], which consists on the study of the interaction between quantum systems and photons confined in a reflective cavity.

The search for materials and quantum emitters that enable fine control of the SE has grown exponentially over the years [40]. And with the increasing progress of near-field optics, plasmonics, and materials science in general, the Purcell effect has been attracting more and more interest of the scientific community [41–51]. In this chapter, we will present an overview of the Purcell effect on the one-photon SE by single emitters. The key objective here is to provide a fundamental understanding on this phenomenon before discussing it in more general situations, such as the case of two-photon spontaneous emission. We start by presenting the SE theory within the context of quantum electrodynamics (QED). After that, we discuss two simple examples of Purcell effect, namely, the influence of a perfect mirror on the decay rate of an atom and the case of SE suppression for an atom inside a metallic cavity. Finally, we present the Green’s tensor formalism for calculating the SE rate of an emitter in an arbitrary environment, which is particularly useful since it allows one to find a solution by using common scattering problem methods.

1.1 One-photon spontaneous emission theory

The phenomenon of SE, just like many others, can be thought as a quantum transition between two states of a system consisting of charged particles (the quantum emitter) and the electromagnetic field. Since the excited states of a quantum emitter are stationary states of the emitter’s Hamiltonian, SE requires the quantization of the electromagnetic field in order to be correctly described. Throughout this thesis we assume the reader has some knowledge of QED, in particular, of atom-field interactions in the Coulomb gauge. For a good introduction to this subject, the reader is referred to [52], and references [53, 54] for further discussion and applications regarding quantum light-matter interactions.

Here we will present only the equations and physical quantities necessary to smooth the understanding of the subject.

1.1.1 One-photon spontaneous emission in free-space

In order to describe the SE process, we consider an emitter, initially in an excited state of its Hamiltonian H_E , placed in vacuum. The Hamiltonian of the emitter-field system can be written as $H = H_E + H_F + H_{int}$, where H_F is the electromagnetic field Hamiltonian and H_{int} is the emitter-field interaction term. We neglect the dynamics of the emitter's center of mass and consider transition wavelengths much larger than the emitter's dimensions, which is generally the case for optical and infrared transitions ($\lambda > 100$ nm, while the Bohr radius is ~ 0.05 nm), so that the electric dipole approximation is valid and we can write [2, 52]

$$H_{int} = -\mathbf{d} \cdot \mathbf{E}(\mathbf{r}) = -i \sum_{\mathbf{k}\lambda} \sqrt{\frac{\hbar\omega_k}{2\epsilon_0 V}} \left[a_{\mathbf{k}\lambda} e^{i\mathbf{k}\cdot\mathbf{r}} \mathbf{d} \cdot \boldsymbol{\epsilon}_{\mathbf{k}\lambda} - a_{\mathbf{k}\lambda}^\dagger e^{-i\mathbf{k}\cdot\mathbf{r}} \mathbf{d} \cdot \boldsymbol{\epsilon}_{\mathbf{k}\lambda}^* \right], \quad (1.1)$$

where $a_{\mathbf{k}\lambda}^\dagger$ and $a_{\mathbf{k}\lambda}$ are respectively the creation and annihilation operators of a photon with wavevector \mathbf{k} and polarization λ ($\lambda = 1, 2$), $\omega_k = kc$ is the photon frequency, \mathbf{d} is the dipole moment operator, $\boldsymbol{\epsilon}_{\mathbf{k}\lambda}$ is the polarization vector, and \mathbf{r} is the emitter's position. Also, for simplicity we are considering the electromagnetic field in a quantization box of volume V .

The interaction Hamiltonian can be treated by perturbative methods, and the eigenstates of $H_0 = H_E + H_F$ are supposed to be known. The initial state can be written as $|i\rangle = |e_i; 0\rangle$, where $|e_i\rangle$ is the emitter's initial state, and $|0\rangle$ is the vacuum field state. Since the field states in free-space are labeled by a continuous variable \mathbf{k} , the transition rate to a final state $|f\rangle$ can be obtained by Fermi's golden rule in first-order perturbation theory, namely [55]

$$\Gamma_{i \rightarrow f} = \frac{2\pi}{\hbar} |\langle f | H_{int} | i \rangle|^2 \delta(E_f - E_i). \quad (1.2)$$

Since H_{int} is linear in the creation and annihilation operators, the matrix element $\langle f | H_{int} | i \rangle$

does not vanish only for final states of the form $|e_f; 1_{\mathbf{k}\lambda}\rangle$, where $|e_f\rangle$ is the emitter's final state and $|1_{\mathbf{k}\lambda}\rangle$ is a one-photon state in the plane-wave representation. Hence, one-photon SE is generally the dominant transition since other field states can only be achieved in higher order processes. After calculating the matrix element in Eq. (1.2), and summing over all allowed final states for the field, we obtain

$$\Gamma_0 = \frac{\pi}{\epsilon_0 \hbar V} \sum_{\mathbf{k}\lambda} \omega_k |\mathbf{d}_t \cdot \boldsymbol{\epsilon}_{\mathbf{k}\lambda}|^2 \delta(\omega_k - \omega_t), \quad (1.3)$$

where $\omega_t = (E_f - E_i)/\hbar$ is the emitter's transition frequency, and $\mathbf{d}_t := \langle e_i | \mathbf{d} | e_f \rangle$ is the transition dipole moment. By taking the limit to the continuum, $\sum_{\mathbf{k}\lambda} \rightarrow \frac{V}{(2\pi)^3} \sum_{\lambda} \int d^3\mathbf{k}$, we have

$$\Gamma_0 = \frac{\pi}{\epsilon_0 \hbar} \frac{1}{(2\pi)^3} \int d^3\mathbf{k} \omega_k \delta(\omega_k - \omega_t) \sum_{\lambda} |\mathbf{d}_t \cdot \boldsymbol{\epsilon}_{\mathbf{k}\lambda}|^2. \quad (1.4)$$

By using the dispersion relation $\omega = kc$ and performing the previous integration using spherical coordinates, we obtain

$$\Gamma_0 = \frac{|\mathbf{d}_t|^2 \omega_t^3}{3\pi \epsilon_0 \hbar c^3}. \quad (1.5)$$

This result was first obtained by Dirac in his famous work, “The quantum theory of the emission and absorption of radiation” [6]. The one-photon SE rate of an atom depends on the transition frequency and on its internal electronic structure through the transition dipole moment. We can use this formula to have an idea of the typical time scale of the decay of an excited atom. Consider for instance the $2p \rightarrow 1s$ transition in hydrogen. The transition frequency is given by $\omega_t^{2p \rightarrow 1s} \approx 1.5 \times 10^{16} Hz$. By using the wavefunctions for the $2p$ and $1s$ hydrogen states, we are able to calculate the transition dipole moment and obtain a numerical value for (1.5). By carrying out these calculations we obtain $\Gamma_0 \approx 6 \times 10^8 s^{-1}$. The mean lifetime of a $2s$ hydrogen atom is then $\tau_0 = 1/\Gamma_0 \approx 1.6 ns$ [56].

1.1.2 Purcell effect: Field modes approach

In this subsection we discuss the influence of material boundaries in the spontaneous

emission, i.e., the Purcell effect. Our first approach is based on the quantization of the electromagnetic field subject to the boundary conditions imposed by the environment. For simplicity, we consider only dissipationless materials. In this case, it is sufficient to make the substitution $e^{i\mathbf{k}\cdot\mathbf{r}}\epsilon_{\mathbf{k}\lambda}/\sqrt{V} \rightarrow \mathbf{A}_\alpha(\mathbf{r})$, where $\{\mathbf{A}_\alpha\}$ is a complete set of solutions of the Helmholtz equation subjected to the given boundary conditions [2]. Following calculations analogous to those used in the previous section one can obtain the one-photon SE rate in the presence of a material body, namely

$$\Gamma(\mathbf{r}) = \frac{\pi}{\epsilon_0\hbar} \sum_\alpha \omega_\alpha |\mathbf{d}_t \cdot \mathbf{A}_\alpha(\mathbf{r})|^2 \delta(\omega_\alpha - \omega_t). \quad (1.6)$$

Eq. (1.6) explicitly shows the dependence of the one-photon SE rate on the environment. Since different materials and geometries result in different sets of field modes, the decay rate is modified by changing the vicinities of the quantum emitter. It is also clear how the density of states of the electromagnetic field impacts the one-photon SE by looking at this formula. Each field state that has the same energy as the emitter's transition energy contributes with a factor proportional to the coupling between the transition dipole moment and the corresponding field mode, $|\mathbf{d}_t \cdot \mathbf{A}_\alpha(\mathbf{r})|^2$. Field modes that are higher in magnitude than others in the same direction have a bigger contribution to the SE rate . Also, modes that are orthogonal to the transition dipole moment do not contribute to the decay. Hence, the one-photon SE rate is proportional to the electromagnetic field density of states projected in the direction of \mathbf{d}_t , also known as partial local density of states and given by

$$\rho(\hat{\mathbf{n}}; \mathbf{r}, \omega) = \hat{\mathbf{n}} \cdot \left[\sum_\alpha \mathbf{A}_\alpha^*(\mathbf{r}) \mathbf{A}_\alpha(\mathbf{r}) \delta(\omega_\alpha - \omega) \right] \cdot \hat{\mathbf{n}}, \quad (1.7)$$

where $\hat{\mathbf{n}}$ is a unit vector. Despite its simplicity, the field modes approach to the SE phenomenon can be applied in a variety of interesting examples, enabling us to get an intuition on the general behaviour of the one-photon SE rate of an atom close to a surface.

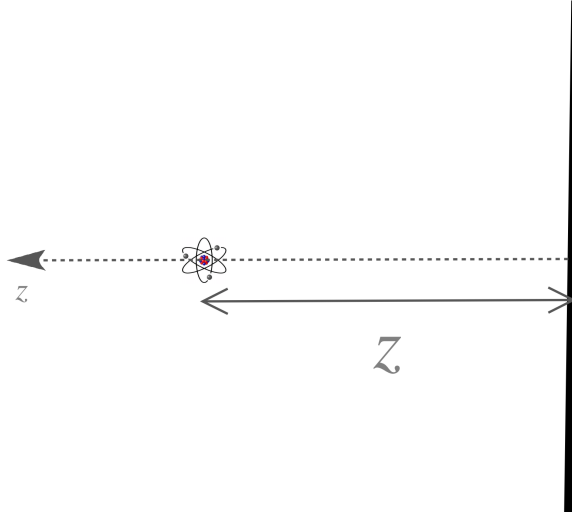


Figure 1.1: Schematics of an atom placed a distance z from a perfectly conducting plane.

1.1.3 An atom close to a perfect mirror

In this subsection we will apply Eq. (1.6) to a system constituted by an atom close to a metallic surface, which, as we previously mentioned, was used in the first experimental observation of the Purcell effect. For simplicity we consider an atom placed a distance z from a perfectly conducting infinite plane at $z = 0$, as shown in Fig. 1.1. The electro-magnetic field modes satisfying the boundary conditions $\mathbf{E} \times \hat{\mathbf{z}}|_{z=0} = 0$ and $\mathbf{B} \cdot \hat{\mathbf{z}}|_{z=0} = 0$ are given by [2, 57]

$$\mathbf{A}_{\mathbf{k},1}(\mathbf{r}) = \sqrt{\frac{2}{V}} \sin(k_z z) e^{i\mathbf{k}_{\parallel} \cdot \mathbf{r}} (\hat{\mathbf{k}}_{\parallel} \times \hat{\mathbf{z}}), \quad (1.8)$$

$$\mathbf{A}_{\mathbf{k},2}(\mathbf{r}) = \sqrt{\frac{2}{V}} \frac{1}{k} [k_{\parallel} \cos(k_z z) \hat{\mathbf{z}} - i k_z \sin(k_z z) \hat{\mathbf{k}}_{\parallel}] e^{i\mathbf{k}_{\parallel} \cdot \mathbf{r}}. \quad (1.9)$$

We can use Eq. (1.6) for calculating the one-photon SE rate of the atom as a function of the distance z . It is convenient to split the transition dipole moment into the sum of its parallel and perpendicular components with respect to the mirror. After integration over the \mathbf{k} space, one can show that the crossed terms do not contribute to the SE rate.

Therefore, Γ can be decomposed as

$$\Gamma = \frac{\mathbf{d}_t \cdot \hat{\mathbf{z}}}{|\mathbf{d}_t|} \Gamma_{\perp} + \left(1 - \frac{\mathbf{d}_t \cdot \hat{\mathbf{z}}}{|\mathbf{d}_t|}\right) \Gamma_{\parallel}, \quad (1.10)$$

where Γ_{\perp} and Γ_{\parallel} are the SE rates of an emitter with transition dipole moment perpendicular and parallel to the plate, respectively. For an isotropic atom, the transition dipole moment can be averaged over all directions and the SE rate can be cast as

$$\Gamma_{iso} = \frac{1}{3} \Gamma_{\perp} + \frac{2}{3} \Gamma_{\parallel}. \quad (1.11)$$

Let's calculate both SE rates, starting by the perpendicular term. After inserting the field modes given by Eqs. (1.8) and (1.9) into Eq. (1.6) we have

$$\Gamma_{\perp} = \frac{|\mathbf{d}_t|^2}{\epsilon_0 \hbar (2\pi)^2} \int d^3 \mathbf{k} \frac{k_{\parallel}^2}{k^2} \cos^2(k_z z) \omega_k \delta(\omega_k - \omega_t). \quad (1.12)$$

By using the dispersion relation $\omega_k = kc$, substituting $k_{\parallel}^2 = k^2 - k_z^2$, integrating in spherical coordinates, and normalizing the result by the free-space SE rate given by Eq. (1.5) we obtain

$$\frac{\Gamma_{\perp}}{\Gamma_0} = 3 \left[\frac{1}{3} - \frac{\cos(2k_t z)}{(2k_t z)^2} + \frac{\sin(2k_t z)}{(2k_t z)^3} \right], \quad (1.13)$$

where $k_t = \omega_t/c$. The normalized parallel SE rate can be calculated by similar procedures, yielding

$$\frac{\Gamma_{\parallel}}{\Gamma_0} = \frac{3}{2} \left[\frac{2}{3} - \frac{\sin(2k_t z)}{(2k_t z)} - \frac{\cos(2k_t z)}{(2k_t z)^2} + \frac{\sin(2k_t z)}{(2k_t z)^3} \right]. \quad (1.14)$$

In Fig. 1.2 we plot the SE rates of an emitter given by Eqs. (1.13), (1.14), and (1.11) as a function of z . We first notice that, when the emitter is very close to the mirror, the perpendicular SE rate is twice the free-space value, while the parallel component vanishes. Both results can be interpreted in terms of the image method if we replace the quantum emitter by a classical radiating dipole [37]. In the perpendicular configuration the image is equal to the real dipole, which results in a net electric dipole of $2\mathbf{d}_t$ at $k_t z = 0$. On the other hand, in the parallel configuration the real and image dipoles are out of

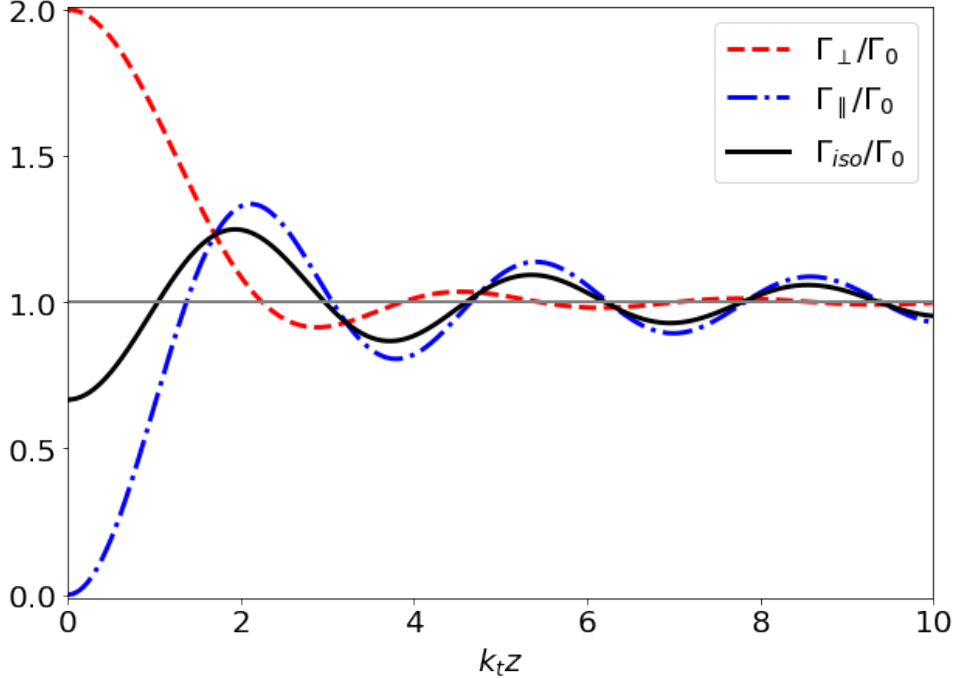


Figure 1.2: Normalized SE rates of a quantum emitter close to a perfectly conducting plate as a function of the distance.

phase and cancel each other at $k_t z = 0$, which results in the suppression of the dipole radiation. In all curves, we observe an oscillatory behaviour with respect to the distance from the atom to the mirror. This can be understood as an interference phenomenon if we decompose the modes given by Eqs. (1.8) and (1.9) as $\mathbf{A}_{\mathbf{k}\lambda} = \mathbf{A}_{\mathbf{k}\lambda}^{(0)} + \mathbf{A}_{\mathbf{k}\lambda}^{(sca)}$, where $\mathbf{A}_{\mathbf{k}\lambda}^{(0)}$ is the corresponding free-space mode and $\mathbf{A}_{\mathbf{k}\lambda}^{(sca)}$ is the reflection of $\mathbf{A}_{\mathbf{k}\lambda}^{(0)}$ by the surface. Since the field modes must be evaluated at the emitter's position, depending on the distance between the emitter and the mirror the free-space contribution may interfere constructively or destructively with the reflected mode. Finally, for $z \rightarrow \infty$ all curves tends to 1, i.e., far enough from the surface the decay rate converges to the free-space SE rate.

The insights we obtained so far can be used to understand the SE phenomenon in more complex situations. For instance, despite the difficulty of computing the electromagnetic field modes of a sphere, we can still expect an oscillatory behaviour of Γ as a function of

distance since the interference between the free-space and scattered waves will continue to play a role in this system.

1.1.4 An emitter between two perfect mirrors

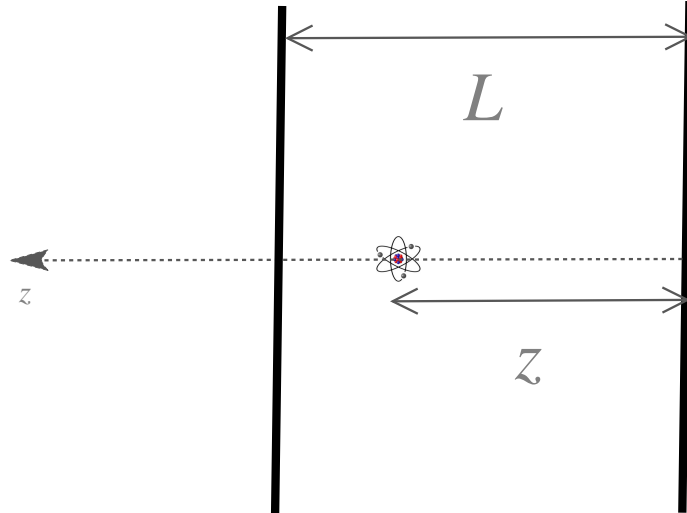


Figure 1.3: An atom between two perfectly conducting plates separated by a distance L .

In this subsection we investigate the one-photon SE of an atom between two perfectly conducting parallel plates, as shown in Fig. 1.3. The field modes of this configuration are also given by Eqs. (1.8) and (1.9), but in order to satisfy the boundary conditions at the second mirror, the z -component of the wavevector must be quantized. For a separation distance between the plates given by L we have $k_z = n\pi/L$, $n = 0, 1, 2, \dots$. The calculations can be carried out within the field modes approach. After performing all integrations, one can show that Eq. (1.11) is still valid, but with the parallel and perpendicular SE rates given by

$$\frac{\Gamma_{\perp}}{\Gamma_0} = \frac{3\pi}{kL} \sum_{n=0}^{[kL/\pi]}' \cos^2 \left(\frac{n\pi z}{L} \right) \left[1 - \frac{n^2\pi^2}{k^2L^2} \right], \quad (1.15)$$

$$\frac{\Gamma_{\parallel}}{\Gamma_0} = \frac{3\pi}{2kL} \sum_{n=1}^{[kL/\pi]} \sin^2 \left(\frac{n\pi z}{L} \right) \left[1 + \frac{n^2\pi^2}{k^2L^2} \right], \quad (1.16)$$

where $[kL/\pi]$ is the greatest integer smaller than kL/π and the prime in the summation indicates that the first term must be multiplied by $1/2$.

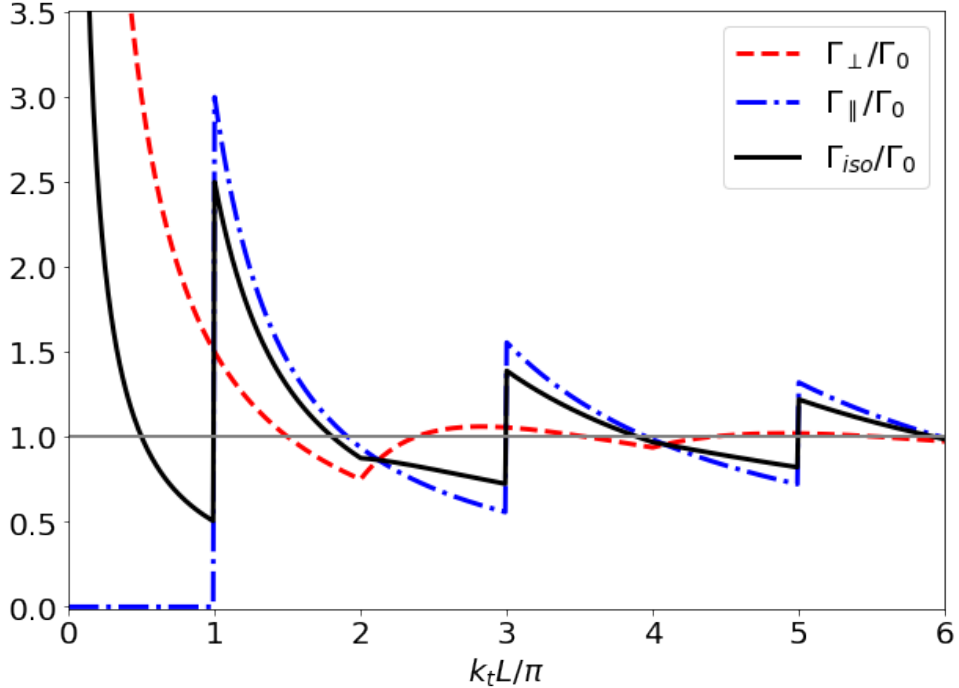


Figure 1.4: Normalized SE rates of a quantum emitter placed exactly in the middle ($z = L/2$) of two perfectly conducting plates as a function of the distance between them.

In Fig. 1.4 we plot the SE rates of an emitter equidistant from both plates ($z = L/2$) given by Eqs. (1.15), (1.16), and (1.11) as a function of L . We notice the presence of discontinuities in the parallel and perpendicular decay rates at $L = m\pi/k_t$ for $m = 1, 2, \dots$. We can interpret this feature by looking at Eqs. (1.15), (1.16) and noticing that a new mode starts contributing exactly at these values of L . Also, since the contribution of a mode is proportional to $\cos^2(\frac{m\pi}{2})$ ($\sin^2(\frac{m\pi}{2})$) for the perpendicular (parallel) component, only modes with even (odd) values of m show up as discontinuities in the plot. Last, but not least, we observe the suppression of Γ_{\parallel} for distances below π/k_t , which can be attributed to the fact that the only mode present in this regime ($n = 0$) is perpendicular to the plates and does not couple with a dipole oriented parallel to the mirrors.

The suppression of the SE is a remarkable phenomenon which opens the possibility

of manipulating excited atoms for large time intervals. But this phenomenon cannot be observed in this system for an isotropic atom, as can be seen in the figure. Hulet *et al* were the first ones to experimentally verify it by using large Rydberg atoms [36], which possess a well defined transition dipole moment. However, this is not the only situation where the SE suppression can be achieved. Any system that has negligible partial local density of states at the emitter's transition frequency will substantially diminish the decay rate of the quantum emitter. For instance, photonic crystals present band gaps where the electromagnetic field density of states is effectively zero [58], and can be used to suppress the SE, as it has been previously demonstrated by E. Yablonovitch [59].

A final remark it is worth mentioning in this subsection concerns the quantization of the field modes in a cavity. In the system we considered, only the z-component of the wavevector was discrete. However, if we have a full cavity (for instance, a metallic spherical shell), all components of the wavevector are quantized, which implies quantization of energy inside the cavity. In this situation, the emitter may resonate with the cavity if its transition frequency is equal to one of the cavity field modes frequencies. Depending on the time interval of observation, the atom can even reabsorb the emitted photon, resulting in oscillations in the transition probability known as Rabi oscillations [54, 60]. This kind of phenomenon allowed the investigation of fundamental questions in quantum mechanics through the precise manipulation of photons and atoms inside a cavity, in a field referred to as cavity QED [38]. However, this type of interaction is out of the scope of this thesis since it requires the usage of non-perturbative methods.

1.2 Green's tensor formalism

In this section we introduce the Green's function formalism for calculating SE rates. We have two main reasons for that. First, Eq. (1.6) may be inconvenient since it relies on finding a complete set of modes that satisfy the boundary conditions imposed by the environment. As we shall see, the Green's tensor formalism reformulates the problem

as a scattering problem, which can also be very complicated, but there are plenty of methods for finding the scattered field by different geometries and well known results that we can use to our advantage. Second, the field modes approach is not general since the definition of these modes are not clear when the considered materials present non-negligible dissipation [61]. In these situations, which are generally what we find in the real world, the Green's tensor approach is extremely convenient. We subdivided this section into two subsections, the first one is dedicated to the presentation of the general formalism, while in the second we present an application of it.

1.2.1 Theoretical framework

In this subsection we show how the SE rate can be obtained by the Green's tensor of the vectorial Helmholtz equation in frequency-space, namely [62]

$$\nabla \times \nabla \times \mathbb{G}(\mathbf{r}, \mathbf{r}', \omega) - \frac{\omega^2}{c^2} \mathbb{G}(\mathbf{r}, \mathbf{r}', \omega) = \mathbb{I}\delta(\mathbf{r} - \mathbf{r}'). \quad (1.17)$$

Such as the electromagnetic field modes, the Green's tensor must also satisfy the boundaries conditions imposed by the environment. The trick here is that the SE rate can be written directly in terms of the Green's tensor, and not necessarily into its (sometimes undefined) decomposition in terms of a particular set of field modes. Here, we will present a simplified derivation of the SE rate dependence on the Green's tensor. A more general demonstration requires a discussion of macroscopic QED [61, 63].

We start the derivation by expanding the Green's tensor in terms of a complete set of field modes that satisfy the vectorial Helmholtz equation (they could be the same of the field modes approach),

$$\mathbb{G}(\mathbf{r}, \mathbf{r}', \omega) = \sum_{\alpha} \mathbf{C}_{\alpha}(\mathbf{r}') \mathbf{A}_{\alpha}(\mathbf{r}). \quad (1.18)$$

By inserting this expansion into Eq. (1.17), taking the scalar product with $\mathbf{A}_{\alpha'}^*(\mathbf{r})$ in both sides of the equation and integrating over the whole space we find that

$$\mathbf{C}_{\alpha}(\mathbf{r}') = c^2 \frac{\mathbf{A}_{\alpha}^*(\mathbf{r}')}{\omega_{\alpha}^2 - \omega^2}, \quad (1.19)$$

and, consequently, we have

$$\mathbb{G}(\mathbf{r}, \mathbf{r}', \omega) = \sum_{\alpha} c^2 \frac{\mathbf{A}_{\alpha}^*(\mathbf{r}') \mathbf{A}_{\alpha}(\mathbf{r})}{\omega_{\alpha}^2 - \omega^2}, \quad (1.20)$$

which is the spectral representation of the Green's tensor. Now, by taking the imaginary part of the previous equation, moving the Green's tensor poles upwards in the complex plane with the substitution $\omega_{\alpha} \rightarrow \omega_{\alpha} - i\epsilon$, and using the identity [64]

$$\lim_{\epsilon \rightarrow 0^+} \frac{1}{\omega^2 - (\omega_{\alpha} - i\epsilon)^2} = P \frac{1}{\omega^2 - \omega_{\alpha}^2} - \frac{i\pi}{2\omega} [\delta(\omega - \omega_{\alpha}) - \delta(\omega + \omega_{\alpha})], \quad (1.21)$$

we find that

$$\text{Im}\mathbb{G}(\mathbf{r}, \mathbf{r}', \omega) = \frac{\pi c^2}{2\omega} \sum_{\alpha} \mathbf{A}_{\alpha}^*(\mathbf{r}') \mathbf{A}_{\alpha}(\mathbf{r}) \delta(\omega - \omega_{\alpha}). \quad (1.22)$$

Finally, by taking $\mathbf{r}' = \mathbf{r}$, using Eq. (1.6) to replace the summation in the right hand side of the previous equation by the emitter's decay rate, and normalizing it by the free-space SE rate given by Eq. (1.5), we obtain

$$\frac{\Gamma}{\Gamma_0} = \frac{6\pi c}{\omega_t} \hat{\mathbf{n}}_t^* \cdot [\text{Im}\mathbb{G}(\mathbf{r}, \mathbf{r}, \omega_t)] \cdot \hat{\mathbf{n}}_t, \quad (1.23)$$

where $\hat{\mathbf{n}}_t = \mathbf{d}_t / |\mathbf{d}_t|$. This equation shows us that the problem of calculating the normalized SE rate of a quantum emitter in a given environment is the same as inverting the vectorial Helmholtz equation and then evaluating the imaginary part of the inverse operator (i.e., the Green's tensor) at the emitter's position. In this approach, the difficulty of finding a complete set of field modes is encoded in a direct relation between the decay rate and the Green's tensor. Despite the fact that we have demonstrated Eq. (1.23) from Eq. (1.6), we emphasize that the Green's tensor approach is more general and does not depend on the existence of a complete set of field modes. Hence, we are allowed to use Eq. (1.23) when the emitter is close to a dissipative object.

Obtaining the Green's function of an equation is a task as difficult as finding a complete set of solutions satisfying the same equation and corresponding boundary conditions. However, there is an extensive literature dedicated to this problem that we can leverage

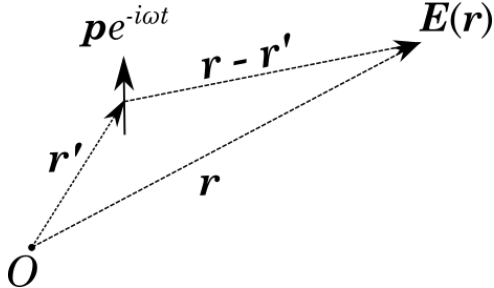


Figure 1.5: Schematics of a point electric dipole of magnitude \mathbf{p} oscillating with frequency ω and placed at \mathbf{r}' with respect to the origin \mathcal{O} . For a given position \mathbf{r} , the dipole produces an electric field given by $\mathbf{E}(\mathbf{r})$

to our benefit. In SE problems, it is very common to use the relation between the Green's tensor and the electric field of a point dipole \mathbf{p} oscillating with frequency ω and placed at \mathbf{r}' (depicted in Fig. 1.5) [62],

$$\mathbb{G}(\mathbf{r}, \mathbf{r}', \omega) \cdot \mathbf{p} = \frac{1}{\mu_0 \omega^2} \mathbf{E}(\mathbf{r}). \quad (1.24)$$

Since we can write $\mathbf{E} = \mathbf{E}^{(0)} + \mathbf{E}^{(sca)}$, where $\mathbf{E}^{(0)}$ is the electric field of an oscillating point dipole in free-space, and $\mathbf{E}^{(sca)}$ is the field scattered by the environment, this relation allows us to calculate the Green's tensor (and consequently the SE rate of a quantum emitter) by solving a scattering problem. Mathematically, we can substitute Eq. (1.24) into Eq. (1.23) to find

$$\frac{\Gamma}{\Gamma_0} = 1 + \frac{6\pi\epsilon_0 c^3}{\omega_t^3 d_t} \text{Im} [\hat{\mathbf{n}}_t \cdot \mathbf{E}^{(sca)}(\mathbf{r})], \quad (1.25)$$

where we used the fact that the contribution of $\mathbf{E}^{(0)}$ results in the free-space SE rate. We will use this powerful tool in the example of the next subsection (and in the next chapters).

1.2.2 An emitter near a semi-infinite dispersive medium

In this subsection we will calculate the SE rate of an atom separated by a distance z' from a semi-infinite dispersive medium. Our approach will be based on the formalism presented in the previous subsection, where the SE problem is mapped to the task of calculating the scattered field of an oscillating dipole by the semi-infinite medium.

In the Lorenz gauge, the electric field can be written in terms of the vector potential $\mathbf{A}(\mathbf{r})$ as

$$\mathbf{E}(\mathbf{r}) = i\omega \left[1 + \frac{1}{k^2} \nabla \nabla \cdot \right] \mathbf{A}(\mathbf{r}). \quad (1.26)$$

In order to find the scattered component, we must first find a representation for the electric field that matches the geometry of the system, i.e., facilitates the task of applying the boundary conditions by not coupling different expansion components. For the case of a semi-infinite medium, this is the Weyl representation [65]. In this basis, the vector potential of a dipole in free-space can be written as [62, 65]

$$\mathbf{A}^{(0)}(\mathbf{r}) = \mathbf{p} \frac{\mu_0 \omega}{8\pi^2} \int d\mathbf{k}_{\parallel} \frac{e^{i\mathbf{k}_{\parallel} \cdot (\mathbf{r}-\mathbf{r}') + ik_z|z-z'|}}{k_z}, \quad (1.27)$$

where $\mathbf{k}_{\parallel} = k_x \hat{\mathbf{x}} + k_y \hat{\mathbf{y}}$ and

$$k_z = \begin{cases} \sqrt{k^2 - k_{\parallel}^2} =: \xi, & \text{if } k_{\parallel} \leq k, \\ i\sqrt{k_{\parallel}^2 - k^2} =: i\zeta, & \text{if } k_{\parallel} > k. \end{cases} \quad (1.28)$$

We notice that this representation consists of a superposition of plane and evanescent waves, i.e., waves that propagates in a direction parallel to the surface of the semi-infinite medium but with amplitudes that decay exponentially with respect to its distance from the interface. These waves are extremely relevant in the so called near-field regime ($kz \ll 1$) where the coupling between these modes and the dipole becomes strong. As we will see next, this regime is generally characterized by huge enhancements of the SE. When $kz \gtrsim 1$, however, these evanescent modes decay and the coupling with plane waves dominate the SE emission, resulting in smaller variations of the decay rate.

For simplicity, let's consider a dipole oriented perpendicular to the dispersive medium surface, i.e., in the z direction. The free-space electric field can be obtained by inserting Eq. (1.27) into (1.26), which yields

$$\mathbf{E}^{(0)}(\mathbf{r}) = p \frac{i\mu_0 c^2}{8\pi^2} \int d\mathbf{k}_{\parallel} \begin{bmatrix} \mp k_x \\ \mp k_y \\ k_{\parallel}^2/k_z \end{bmatrix} e^{i\mathbf{k}_{\parallel} \cdot \mathbf{r} + ik_z|z-z'|}. \quad (1.29)$$

In the previous equation we used a column vector representation for the electric field, where the upper sign should be used for $z > z'$, while the lower sign for $z < z'$. One can inspect the integrand of the right-hand side of this equation and notice that each wave of the superposition is a p-wave, i.e., the vector inside brackets is parallel to the incidence plane. Hence, the scattered field is given by the same superposition, but weighted by the corresponding Fresnel reflection and transmission coefficients [64]. Since we need to evaluate the field at the position of the dipole, we need only to consider the reflected field, which has a phase difference of π in its z-component and is given by

$$\mathbf{E}^{(sca)}(\mathbf{r}) = p \frac{i\mu_0 c^2}{8\pi^2} \int d\mathbf{k}_{\parallel} [-r^p(k_{\parallel})] \begin{bmatrix} k_x \\ k_y \\ -k_{\parallel}^2/k_z \end{bmatrix} e^{i\mathbf{k}_{\parallel} \cdot \mathbf{r} + ik_z(z+z')}, \quad (1.30)$$

where r^p is the Fresnel reflection coefficient of a p-wave. At coincidence ($z = z'$), the parallel components of the field vanish after integration, and only the z-component is left. After separating the integral into two terms, one consisting of the integral for $k_{\parallel} < k$ and the other for $k_{\parallel} > k$, we have

$$\mathbf{E}^{(sca)}(z) = p\hat{\mathbf{z}} \frac{i\mu_0 c^2}{4\pi} \int_0^k dk_{\parallel} r^p(k_{\parallel}) \frac{k_{\parallel}^3}{\xi} e^{2i\xi z'} + \hat{\mathbf{z}} \frac{\mu_0 c^2}{4\pi} \int_k^\infty dk_{\parallel} r^p(k_{\parallel}) \frac{k_{\parallel}^3}{\zeta} e^{-2\zeta z}. \quad (1.31)$$

Finally, after redefining $p \rightarrow d_t$ and inserting the scattered field into (1.25) we find

$$\frac{\Gamma_{\perp}}{\Gamma_0} = 1 + \frac{3}{2} \int_0^{k_t} dk_{\parallel} \frac{k_{\parallel}^3}{k_t^3 \xi} \text{Re}[r^p(k_{\parallel}) e^{2i\xi z}] + \frac{3}{2} \int_{k_t}^\infty dk_{\parallel} \frac{k_{\parallel}^3}{k_t^3 \zeta} \text{Im}[r^p(k_{\parallel})] e^{-2\zeta z}, \quad (1.32)$$

which is the SE rate of a quantum emitter in front of any semi-infinite linear and isotropic dispersive medium. The parallel contribution can be obtained by similar calculations, resulting in [62, 66]

$$\begin{aligned} \frac{\Gamma_{\parallel}}{\Gamma_0} &= 1 + \frac{3}{4} \int_0^{k_t} dk_{\parallel} \frac{k_{\parallel}}{k_t^3 \xi} \text{Re}[(k_t^2 r^s(k_{\parallel}) - \xi^2 r^p(k_{\parallel})) e^{2i\xi z}] \\ &+ \frac{3}{4} \int_{k_t}^\infty dk_{\parallel} \frac{k_{\parallel}}{k_t^3 \zeta} \text{Im}[k_t^2 r^s(k_{\parallel}) + \zeta^2 r^p(k_{\parallel})] e^{-2\zeta z}, \end{aligned} \quad (1.33)$$

where r^s is the Fresnel reflection coefficient for s-waves, which have polarization vectors perpendicular to the incidence plane. Once the dispersive medium is chosen, the Fresnel

coefficients can be written as [62, 64]

$$r^s(\omega, k_{\parallel}) = \frac{k_z(\omega, k_{\parallel}) - k_{z1}(\omega, k_{\parallel})}{k_z(\omega, k_{\parallel}) + k_{z1}(\omega, k_{\parallel})}, \quad (1.34)$$

$$r^p(\omega, k_{\parallel}) = \frac{\epsilon(\omega)k_z(\omega, k_{\parallel}) - \epsilon_0k_{z1}(\omega, k_{\parallel})}{\epsilon(\omega)k_z(\omega, k_{\parallel}) + \epsilon_0k_{z1}(\omega, k_{\parallel})}, \quad (1.35)$$

where $\epsilon(\omega)$ is its dielectric permittivity of the medium, $k_z(\omega, k_{\parallel})$ is given by Eq. (1.28), and $k_{z1} := \sqrt{\mu_0\epsilon(\omega)\omega^2 - k_{\parallel}^2}$.

As an example for numerical evaluation, let's consider a Polystyrene medium described by a Lorentz model, namely [64],

$$\frac{\epsilon(\omega)}{\epsilon_0} = 1 + \sum_i \frac{\omega_{p_i}^2}{\omega_{R_i}^2 - \omega^2 - i\omega/\tau} \quad (1.36)$$

where ω_{p_i} are the plasma frequencies of the medium, ω_{R_i} are the resonance frequencies, and τ is the relaxation time. In Fig. 1.6(a) we plot separately the contributions to the SE rate of the parallel and perpendicular components of the transition dipole moment of a quantum emitter as a function of distance in the near-field. As we mentioned before, in this regime the SE rate is very high in comparison to the free-space value due to the coupling with evanescent modes. It is important to notice, however, that the main decay pathway is through the emission of evanescent surface waves that are dissipated by the material, not through photons. The functional dependence of Γ with z is a power law, as can be seen by noticing the linear dispersion in the log-scale plot. This power law is given by z^{-3} , and has its origins in the coulombian interaction between the atomic transition electric dipole and the bulk. In Fig. 1.6(b) we have the same plot, but for $kz \gtrsim 1$. At these large separations, we are able to observe oscillations in the SE rate similar to those found in the atom-mirror system (see Fig. 1.2). However, the Purcell effect is not as nearly as high as in the near-field regime.

The message that we take from this subsection is that the standard coupling with photons can be modified, but hardly made as efficient as with confined modes such as the lossy surface waves of dielectrics. Indeed, the path to harness the SE via Purcell

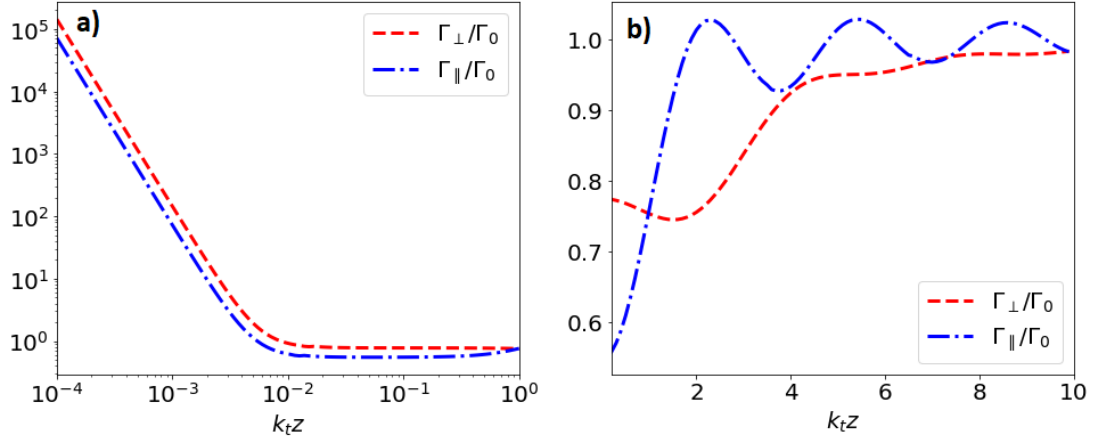


Figure 1.6: Normalized SE rates of a quantum emitter near a semi-infinite near a half-space Polystyrene medium as a function of distance. The Polystyrene resonance frequencies are given by $\omega_{R1} = 5.54 \times 10^{14} \text{ rad/s}$ and $\omega_{R2} = 1.35 \times 10^{16} \text{ rad/s}$ and the corresponding relaxation time by $\tau = 10^{-11} \text{ s}^{-1}$ [1]. The emitter transition frequency was chosen as $\omega_{R2}/5$.

effect is the same as the one of finding materials that exhibit high light confinement, as it was already demonstrated by Rivera *et. al* [10]. We can also realize that by looking at the huge development of this field over recent years and noticing that the majority of articles related to SE follow this exact path. In the next chapter we start our discussion of two-quanta spontaneous emission, and, as we shall see, most of the results presented here will be extremely useful in our understanding of this higher-order phenomenon.

Chapter 2

Two-quanta spontaneous emission

In this chapter we present the general theory of two-quanta spontaneous emission (TQSE) by a quantum emitter. We start with a derivation of the two-photon spontaneous emission (TPSE) rate of an atom in free-space and a discussion of its importance in the quantum theory of light. In order to better understand the relevance of the TQSE phenomenon, we dedicate a few paragraphs to compare it with the one-quantum SE presented in the previous chapter. We discuss the Purcell effect in the TQSE, i.e., the influence of the environment in the emission spectrum and decay rate of the emitter. In order to develop a basic understanding of the problem and its singular features, our first study is in the scope of non-dissipative materials, where the field mode approach is suitable for calculating the TPSE in an arbitrary environment. With this theory we investigate the TPSE of an emitter near a perfectly conducting plate and between two parallel mirrors, which are perfect examples to develop an intuition on the phenomenon. We then expand the scope of possible environments to dissipative materials with the Green function formalism. Within this framework, we revisit the example of an emitter near a perfect mirror, which is important to highlight the differences between both methods. We finish this chapter with a demonstration of an important relation between the TQSE spectral density and the one-photon SE Purcell factors. This relation and its subsequent insights will be the basis for the study of TQSE near low-dimensional plasmonic nanostructures presented in chapter 3.

2.1 Two-photon spontaneous emission in free-space

Consider an atom or molecule in free space, i.e., approximately isolated from all bodies in the universe. For transition wavelengths much larger than the emitter dimensions, the interaction Hamiltonian is given by Eq. (1.1). The TPSE can be described as a quantum transition from an initial state $|i\rangle = |e_i; 0\rangle$ to a final state $|e_f; 1_{\mathbf{k}\lambda}, 1_{\mathbf{k}'\lambda'}\rangle$, where $|e_i\rangle$ and $|e_f\rangle$ are the initial and final atomic states, respectively, $|0\rangle$ is the vacuum field state, and $|1_{\mathbf{k}\lambda}, 1_{\mathbf{k}'\lambda'}\rangle$ is a particular two-photon state in the plane-wave representation. Since the interaction Hamiltonian does not connect the initial with the final state, the transition rate between both states cannot be calculated with first-order perturbation theory as can be done in the case of one-photon emission. Thus, TPSE (and TQSE in general) is a second-order process. The TPSE rate can be obtained by second order Fermi's golden rule, namely [3, 55]

$$\Gamma_{i \rightarrow f} = \frac{2\pi}{\hbar} |M_{fi}|^2 \delta(E_f - E_i), \quad (2.1)$$

where

$$M_{fi} = \sum_I \frac{\langle f | H_{int} | I \rangle \langle I | H_{int} | i \rangle}{E_i - E_I}. \quad (2.2)$$

The intermediate states $|I\rangle$ that connect the vacuum with the final states are $|m; 1_{\mathbf{k}\lambda}\rangle$ or $|m; 1_{\mathbf{k}'\lambda'}\rangle$, where m indexes the emitter intermediate states. In order to obtain the transition rate between the atomic states $|e_i\rangle$ and $|e_f\rangle$, we must sum over all possible two-photon states. Defining

$$\mathbb{D}(\omega_\alpha, \omega_{\alpha'}) := \sum_m \left[\frac{\mathbf{d}_{im} \mathbf{d}_{mf}}{\omega_{im} - \omega_\alpha} + \frac{\mathbf{d}_{mf} \mathbf{d}_{im}}{\omega_{im} - \omega_{\alpha'}} \right], \quad (2.3)$$

where $\mathbf{d}_{ab} := \langle a | \mathbf{d} | b \rangle$ and $\omega_{ab} := \frac{E_a - E_b}{\hbar}$, one can show that [67]

$$\Gamma_0 = \frac{\pi}{4\epsilon_0^2 \hbar^2 V^2} \sum_{\mathbf{k}\lambda, \mathbf{k}'\lambda'} \omega_k \omega_{k'} |\boldsymbol{\epsilon}_{\mathbf{k}\lambda} \cdot \mathbb{D}(\omega_k, \omega_{k'}) \cdot \boldsymbol{\epsilon}_{\mathbf{k}'\lambda'}|^2 \delta(\omega_k + \omega_{k'} - \omega_t). \quad (2.4)$$

By taking the limit to the continuum, rewriting the integrals in spherical coordinates, and

using the Einstein notation for summation, we have

$$\begin{aligned}\Gamma_0 &= \frac{\pi}{4\epsilon_o^2\hbar^2} \frac{1}{(2\pi)^6} \int_0^\infty dk k^2 \omega_k \int_0^\infty dk' k'^2 \omega_{k'} \mathbb{D}_{ij}(\omega_k, \omega_{k'}) \mathbb{D}_{ln}^*(\omega_k, \omega_{k'}) \delta(\omega_k + \omega_{k'} - \omega_t) \\ &\times \int d\Omega \sum_\lambda (\boldsymbol{\epsilon}_{\mathbf{k}\lambda})_i (\boldsymbol{\epsilon}_{\mathbf{k}\lambda})_l \int d\Omega' \sum_{\lambda'} (\boldsymbol{\epsilon}_{\mathbf{k}'\lambda'})_j (\boldsymbol{\epsilon}_{\mathbf{k}'\lambda'})_n.\end{aligned}\quad (2.5)$$

The angular integrals can be solved by using the relation $\sum_\lambda (\boldsymbol{\epsilon}_{\mathbf{k}\lambda})_i (\boldsymbol{\epsilon}_{\mathbf{k}\lambda})_j = \delta_{ij} - \hat{k}_i \hat{k}_j$.

After some standard calculations, we find the free space TPSE rate as [3, 11]

$$\Gamma_0 = \int_0^{\omega_t} d\omega \gamma_0(\omega), \quad (2.6)$$

where γ_0 is defined as the spectral distribution of emitted photons in free space and it is given by

$$\gamma_0(\omega) = \frac{\mu_0^2}{36\pi^3\hbar^2c^2} \omega^3 (\omega_t - \omega)^3 |\mathbb{D}(\omega, \omega_t - \omega)|^2, \quad (2.7)$$

with $|\mathbb{D}(\omega, \omega_t - \omega)|^2 := \mathbb{D}_{ij}(\omega, \omega_t - \omega) \mathbb{D}_{ij}^*(\omega, \omega_t - \omega)$. Note that $\gamma_0(\omega)d\omega$ gives the number of emitted photons per unit of time in the interval $[\omega, \omega + d\omega]$. We notice that, in contrast to the one-photon SE, which is a narrow band phenomenon, TPSE is a broadband process. We plot $\gamma_0(\omega)$ in Fig. 2.1. One important feature of the spectral distribution is its symmetry with respect to $\omega_t/2$, namely, $\gamma_0(\omega) = \gamma_0(\omega_t - \omega)$, which is a direct consequence of energy conservation.

2.1.1 On the numerical evaluation of TQSE

In Fig. 2.1 we plotted the spectral density for an idealized three-level system. However, in order to obtain the right numerical values for the TQSE spectrum and decay rate one has to calculate the tensor \mathbb{D} . Since this tensor encodes the emitter's internal electronic structure, this calculation is as difficult as the solution of the Schrodinger's equation for the emitter. Once the wavefunctions are obtained, we are left with the task of calculating the matrix elements \mathbf{d}_{im} and \mathbf{d}_{mf} and perform the summation in Eq. (2.3), which can be done numerically. We notice that this summation must be made not only for the bound

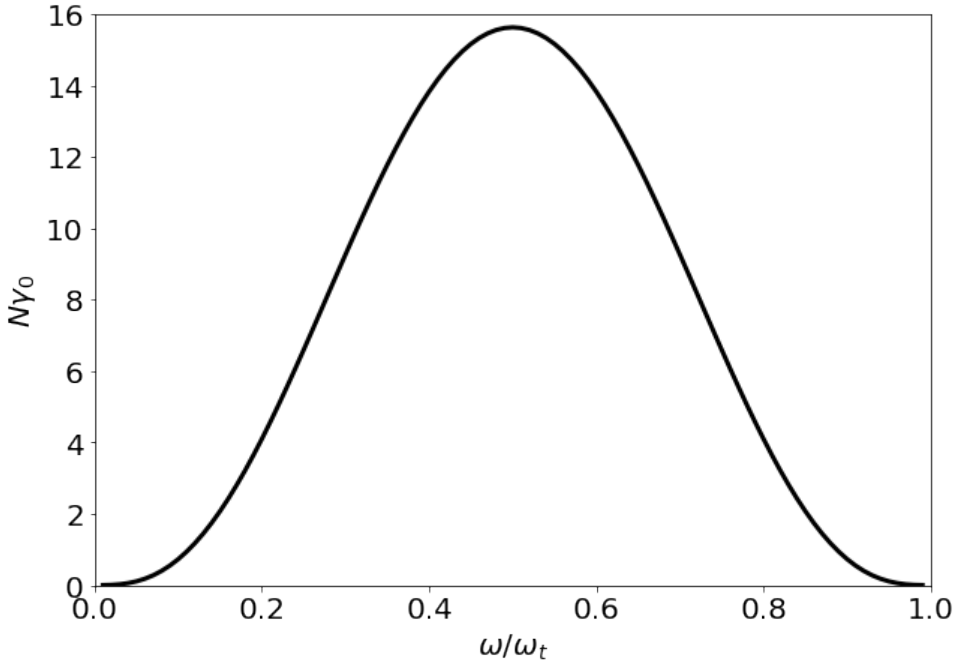


Figure 2.1: γ_0 multiplied by a normalization constant as a function of the normalized frequency of emission. We considered a three-level system with intermediate transition frequency $\omega_{mf} = 3\omega_{if}/2$.

states but also for states in the continuum [3]. This is drastically different from calculating one-photon SE rates, where the internal properties of the emitter manifests only through the transition dipole moment between the initial and final states.

The first numerical calculation of the TPSE rate in free space was made by Breit and Teller in 1940 [12], for the $2s_{1/2} \rightarrow 1s_{1/2}$ transition in hydrogen. In this case, a one-photon transition is not possible due to selection rules¹. In their work, the tensor \mathbb{D} was calculated using the well-known hydrogen wavefunctions, and a lifetime of $\sim 1/7$ s was found for this transition. We notice that this lifetime is much higher than the standard one-photon decays, such as the $2p \rightarrow 1s$ transition, which has a lifetime of the order of a few nanoseconds. Therefore, TPSE is much more difficult to observe experimentally

¹Actually a one-photon dipolar transition between the $2s_{1/2}$ and $2p_{1/2}$ is possible due to the Lamb Shift. However, since the $2s_{1/2}$ is only about 1040 MHz above the $2p_{1/2}$ state, which is 10^7 times smaller than the transition frequency between the $2s$ and $1s$ states, the corresponding lifetime is extremely high, being of the order of thousands of years [3]. Also, magnetic dipole and other higher-order multipolar transitions are not forbidden, but their importance are negligible for single quantum emitters such as atoms and molecules [10]

than its first order counterpart, and the first direct measure of the phenomenon was done only in 1965 by M. Lipeles and co-authors for the $2s \rightarrow 1s$ transition in He^+ [68]. Since the TPSE rate of an hydrogenic atom is proportional to Z^6 [69], where Z is the atomic number, the $2s \rightarrow 1s$ transition in hydrogen is much slower than for He^+ , and its first measure only occurred in 1975 [70]

In this thesis, we will not carry out explicit calculations of the tensor \mathbb{D} . However, it will be very useful to obtain the functional form of \mathbb{D} when the initial and final states are s states. This was already investigated in previous works [12, 71] even for other transitions such as $d \rightarrow s$. Considering the one electron states $|e_i\rangle = |n_i, l = 0, m = 0\rangle$ and $|e_f\rangle = |n_f, l = 0, m = 0\rangle$, the intermediate states which the matrix elements of \mathbf{d} do not vanish are p states and can be written as $|k\rangle = |n, l = 1, m = 0, \pm 1\rangle$. The corresponding wave functions can be written as a product of a radial function by the spherical harmonics. We have $\psi_i(\mathbf{r}) = R_{n_i 0}(r)Y_{00}$, $\psi_f(\mathbf{r}) = R_{n_f 0}(r)Y_{00}$ and $\psi_{nm}(\mathbf{r}) = R_{n 1}(r)Y_{1m}(\theta, \phi)$, so the intermediate transition dipole moments are given by

$$\mathbf{d}_{i,nm} = eY_{00}^* \int_0^\infty dr r^3 R_{n_i 0}^*(r) R_{n 1}(r) \int d\Omega \hat{\mathbf{r}} Y_{1m}(\theta, \phi), \quad (2.8)$$

$$\mathbf{d}_{f,nm} = eY_{00}^* \int_0^\infty dr r^3 R_{n_f 0}^*(r) R_{n 1}(r) \int d\Omega \hat{\mathbf{r}} Y_{1m}(\theta, \phi). \quad (2.9)$$

From these expressions, we note that the directions of these vectors depend only on the angular integrals, while their magnitude depend on the quantum numbers n_i , n_f and n . As l is fixed, the directions depend only on m . Using the expansion

$$\hat{\mathbf{r}} = \sqrt{\frac{4\pi}{3}} \left\{ \frac{(Y_{1-1} - Y_{11})}{\sqrt{2}} \hat{\mathbf{x}} + i \frac{(Y_{1-1} + Y_{11})}{\sqrt{2}} \hat{\mathbf{y}} + Y_{10} \hat{\mathbf{z}} \right\}, \quad (2.10)$$

and calculating explicitly the angular integral for all values of m , we obtain

$$\mathbf{d}_{i,nm} = d_{in} \hat{\epsilon}_m, \quad (2.11)$$

$$\mathbf{d}_{f,nm} = d_{fn} \hat{\epsilon}_m, \quad (2.12)$$

where d_{in} and d_{fn} are proportional to their corresponding radial integrals and the set

$\{\hat{\epsilon}_{-1}, \hat{\epsilon}_0, \hat{\epsilon}_1\}$ is an orthonormal basis in three dimensions given by

$$\hat{\epsilon}_{-1} = -\frac{(\hat{\mathbf{x}} + i\hat{\mathbf{y}})}{\sqrt{2}}; \quad \hat{\epsilon}_1 = \frac{\hat{\mathbf{x}} - i\hat{\mathbf{y}}}{\sqrt{2}}; \quad \hat{\epsilon}_0 = \hat{\mathbf{z}}. \quad (2.13)$$

With this result, we obtain

$$\mathbb{D}(\omega_\alpha, \omega_{\alpha'}) = \sum_n d_{in} d_{nf} \left[\frac{1}{\omega_{in} - \omega_\alpha} + \frac{1}{\omega_{in} - \omega_{\alpha'}} \right] \sum_m \hat{\epsilon}_m \hat{\epsilon}_m^*. \quad (2.14)$$

Due to the fact that the vectors $\hat{\epsilon}_m$ form a basis, we have $\sum_m \hat{\epsilon}_m \hat{\epsilon}_m^* = \mathbb{I}$ and \mathbb{D} takes the form $\mathbb{D}(\omega_\alpha, \omega_{\alpha'}) = D(\omega_\alpha, \omega_{\alpha'})\mathbb{I}$, where

$$D(\omega_\alpha, \omega_{\alpha'}) = \sum_n d_{en} d_{ng} \left[\frac{1}{\omega_{en} - \omega_\alpha} + \frac{1}{\omega_{en} - \omega_{\alpha'}} \right]. \quad (2.15)$$

This expression simplifies the task of considering the emitter's internal structure since the summation over states is now reduced to a summation over energy levels. As a consequence, field modes with orthogonal polarization vectors are decoupled. This feature will be very useful when considering the influence of the environment in the TQSE.

2.1.2 On the TQSE selection rules

Selection rules are constraints on the possible transitions from one quantum state to another. For one-quantum dipolar electronic transitions, it is well known that the initial and final states must differ by one unit of the square orbital angular momentum quantum number, i.e. $\Delta l_{if} = \pm 1$ [72, 73]. For this reason, in first order in perturbation theory a s state is only allowed to transition to a $2p$ state and vice-versa. This constraint is a direct consequence of the condition $\mathbf{d}_{if} \neq 0$, which is necessary for obtaining a non-trivial one-quantum SE rate.

The selection rules for a dipolar TQSE are different from its first order counterpart. In fact, both rules are mutually exclusive. The TQSE selection rules can be derived from the condition $\mathbb{D}(\omega_\alpha, \omega_{\alpha'}) \neq 0$. Since this tensor is a summation of terms proportional to $\mathbf{d}_{im} \mathbf{d}_{mf}$, this condition is satisfied when there is at least one intermediate state such that \mathbf{d}_{im} and \mathbf{d}_{mf} do not vanish. This is satisfied when $\Delta l_{if} = 0, \pm 2$, which is the case for $s \rightarrow s$

and $s \rightarrow d$ transitions, for instance. Therefore, a TQSE transition never competes with a one-quantum transition between the same states. We emphasize, however, that once the emitter is in a given quantum state, it is allowed to decay to any other available lower energy state, some of them by one-quantum SE, others via TQSE. For example, an atom in the $4s$ state is allowed to decay to the $3s$, $2s$, $1s$, and $3d$ states only through TQSE. However, there is also the possibility of one-quantum decay to the $3p$ and $2p$ states, which, in free-space, are dominant transitions. For hydrogenic atoms, the free-space TQSE is only dominant if the emitter is in the $2s$ state since a $1p$ state does not exist.

2.1.3 Resonant TQSE

Until this point we only discussed TQSE as a process where the two quanta are emitted simultaneously. Nevertheless, our calculation also contemplates cascade transitions, consisting of a sequence of two one-quantum transitions, $i \rightarrow m_r \rightarrow f$. Indeed, in Fermi's golden rule summation over intermediate states, multiple processes may contribute to the final TQSE rate. Whenever there exists an emitter state $|m_r\rangle$ such that $E_i > E_{m_r} > E_f$ and $\mathbf{d}_{im}, \mathbf{d}_{mf} \neq 0$, we have a resonant term in Eq. (2.3), and, as a consequence, two resonances in the emission spectrum precisely at frequencies ω_{i,m_r} and $\omega_{if} - \omega_{i,m_r}$. These resonances are related to the one-quantum SE processes, and must be properly taken into account. In order to deal with the infinities in the spectrum, one has to consider the linewidths of the quantum states, which are related to the lifetime of the emitter. Furthermore, the task of separating the contribution of the simultaneous two-quanta emission process is not easy since the resonant states contribute to both processes and cannot be disregarded [74]. Altough this is also an interesting problem, in this thesis we will not consider resonant TQSE and restrict ourselves to the simultaneous emission of two quanta.

2.1.4 Beyond hydrogenic atoms

Due to the difficultes in experimental observations of TQSE in laboratory, for a long

time the study of this phenomenon was restricted to hydrogenic atoms in free space, in particular, of the $2s \rightarrow 1s$ transition. The first work outside this scope was made in 1982, where the TPSE of many electron atoms was considered [75, 76]. This kind of emitter is of interest since one can observe other transitions besides the $2s \rightarrow 1s$ due to the presence of occupied electronic states and the Pauli exclusion principle. In materials science, in 2007 the TPSE from a semiconductor was measured for the first time [13, 77], and was pointed as an efficient source of entangled photon pairs [78]. The TPSE was also studied in quantum dots [79], which are solid state emitters with an internal structure similar to atoms. In this thesis we will always try to present our main equations independently of the chosen emitter. In the numerical calculations we work with hydrogen for proof of concept.

2.2 Field modes approach

In this section we start considering the influence of material boundaries in the TQSE, i.e., the TQSE Purcell effect. As in the case of one-quantum SE, in our first approach we will compute the spectral distribution of the TQSE by using an expression written in terms of the field modes of the electromagnetic field. In this case, it is sufficient to make the substitution $e^{i\mathbf{k}\cdot\mathbf{r}}\epsilon_{\mathbf{k}\lambda}/\sqrt{V} \rightarrow \mathbf{A}_\alpha$ in Eq. (2.4). By carrying out the same calculations done in the previous section one can easily obtain the TQSE rate in the presence of a material body, namely [67]

$$\Gamma(\mathbf{r}) = \frac{\pi}{4\epsilon_0^2\hbar^2} \sum_{\alpha,\alpha'} \omega_\alpha \omega_{\alpha'} |\mathbf{A}_\alpha(\mathbf{r}) \cdot \mathbb{D}(\omega_\alpha, \omega_{\alpha'}) \cdot \mathbf{A}_{\alpha'}(\mathbf{r})|^2 \delta(\omega_\alpha + \omega_{\alpha'} - \omega_t). \quad (2.16)$$

This equation can be used to compute the Purcell effect in the TQSE rate for any dissipationless material. In the next subsections we shall consider two situations, namely, an emitter close to a perfectly conducting plate and between two perfect mirrors, and compare the results with the ones found in the previous chapter. The study of these problems will allow us to discuss many important aspects of the TQSE Purcell effect.

Also, we shall take the opportunity to showcase some of the few advantages of the field modes approach in TQSE with respect to the Green's tensor formalism to be presented later.

2.2.1 TPSE near a perfectly conducting plate

Consider the case of an emitter close to a perfectly conducting plate at $z = 0$ (see Fig. 1.1). The electromagnetic field modes are given by Eqs. (1.8) and (1.9). One of the advantages of Eq. (2.16) is the simple interpretation of the Purcell effect as a consequence of the coupling with the different allowed field modes. For this reason, it is easy to calculate the influence of a particular set of modes in the TQSE. In particular, one is able to extract the angular spectrum of emission. Substituting Eqs. (1.8) and (1.9) into Eq. (2.16) and performing the integrals in the azimuthal angles ϕ and ϕ' we obtain

$$\Gamma(z) = \int_0^{\omega_t} d\omega \int_0^\pi d\theta d\theta' S(\omega, \theta, \theta'; z), \quad (2.17)$$

where $S(\omega, \theta, \theta'; z)$ is the angular distribution of emitted photons, with θ and θ' being the respective angles of the propagation vectors of the two emitted photons with respect to the $\mathcal{O}z$ axis, and given by

$$S = \frac{\mu_0^2}{16\hbar^2\pi^3} \omega^3 (\omega_t - \omega)^3 (S_{\parallel}' + S_{\perp}' + S_c'), \quad (2.18)$$

where

$$\begin{aligned} S_{\parallel}' &= \frac{1}{4} \sum_{i,j=1,2} |\mathbb{D}_{ij}(\omega, \omega_t - \omega)|^2 [\sin^2(kz \cos \theta) \sin \theta (1 + \cos^2 \theta)] \times \\ &\quad \times [\sin^2(kz \cos \theta') \sin \theta' (1 + \cos^2 \theta')], \end{aligned} \quad (2.19)$$

$$S_{\perp}' = |\mathbb{D}_{33}(\omega, \omega_t - \omega)|^2 \cos^2(kz \cos \theta) \sin^3 \theta \cos^2(kz \cos \theta') \sin^3 \theta', \quad (2.20)$$

$$\begin{aligned} S_c' &= \frac{1}{2} \sum_{i=1,2} \left\{ |\mathbb{D}_{i3}(\omega, \omega_t - \omega)|^2 [\sin^2(kz \cos \theta) \sin \theta (1 + \cos^2 \theta)] \cos^2(kz \cos \theta') \sin^3 \theta' + \right. \\ &\quad \left. + |\mathbb{D}_{3i}(\omega, \omega_t - \omega)|^2 \cos^2(kz \cos \theta) \sin^3 \theta [\sin^2(kz \cos \theta') \sin \theta' (1 + \cos^2 \theta')] \right\}. \end{aligned} \quad (2.21)$$

For an observer in the far field, the angular distribution gives the number of emitted photon-pairs with frequencies between ω and $\omega + d\omega$ and within the angular intervals

$[\theta, \theta + d\theta]$ and $[\theta', \theta' + d\theta']$. After integrating the angular distribution in θ and θ' it is straightforward to show that the TPSE rate can be written in the form

$$\Gamma(z) = \int_0^{\omega_t} d\omega \gamma(\omega; z), \quad (2.22)$$

where the spectral distribution is now given by

$$\gamma(\omega; z) = \gamma_0(\omega) \sum_{i,j} \frac{|\mathbb{D}_{ij}(\omega, \omega_t - \omega)|^2}{|\mathbb{D}(\omega, \omega_t - \omega)|^2} P_i(\omega; z) P_j(\omega_t - \omega; z), \quad (2.23)$$

with P_1 and P_2 given by Eq. (1.14) and P_3 by Eq. (1.13) being the Purcell factors associated with the one-photon SE of an emitter with a transition dipole moment oriented parallel or perpendicular to the plate, respectively. Since the presence of the plate breaks the translational symmetry along the z direction, the spectral distribution function depends not only on the frequency but also on the distance from the emitter to the surface.

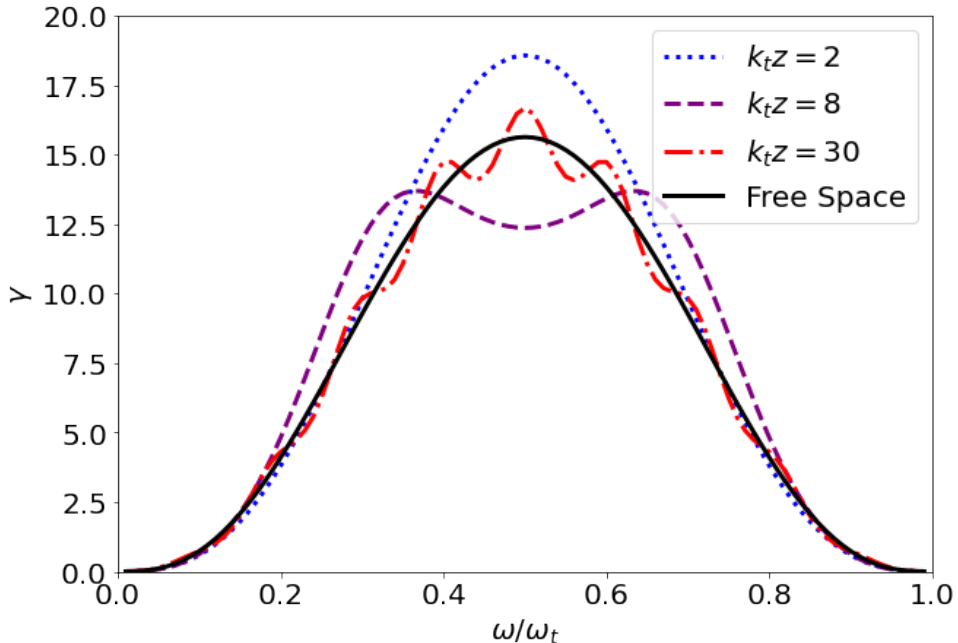


Figure 2.2: Spectral density function $\gamma(\omega; z)$ of an emitter near a perfect mirror in terms of the dimensionless variable ω/ω_t for three different values of z . We also plot the spectral density function in free space (solid line).

In Figure 2.2 we plot $\gamma(\omega; z)$ *versus* ω for different distances between the emitter

and the plate. We considered a $s \rightarrow s$ transition and only one intermediate state in Eq. (2.3). As expected, note the symmetry of all spectral distributions with respect to $\omega_t/2$. Observe, also, that the spectral distribution may acquire forms quite different from the parabolical shape of the corresponding one in free space and its maximum may not necessarily occur at $\omega_t/2$. Moreover, as the distance between the emitter and the plate increases, the spectral distribution tends to the free space one, as expected.

In order to trace out the intermediate states in Eq. (2.3), it is convenient to work with the ratio $\gamma(\omega; \mathbf{r})/\gamma_0(\omega)$, sometimes referred to as spectral enhancement [14]. For $s \rightarrow s$ transitions, we can insert the simple form of \mathbb{D} given by Eq. (2.15) into (2.16) and show that

$$\frac{\gamma(\omega, \mathbf{r})}{\gamma_0(\omega)} = \frac{1}{3} \sum_i P_i(\omega, \mathbf{r}) P_i(\omega_t - \omega, \mathbf{r}). \quad (2.24)$$

Since the spectral enhancement depends only on the transition frequency of the emitter

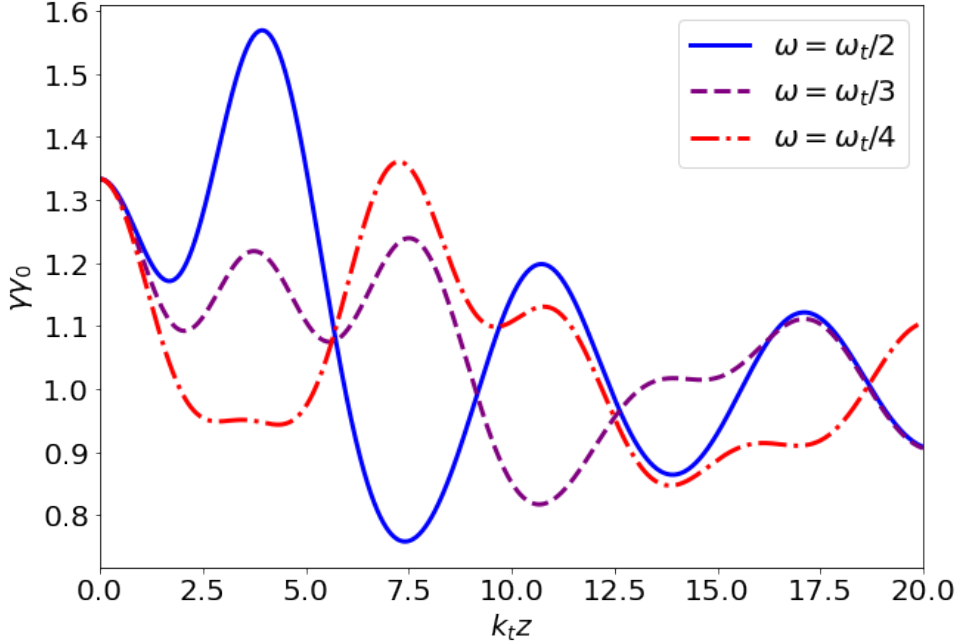


Figure 2.3: Spectral enhancement $\gamma(\omega; z)/\gamma_0(\omega)$ of an emitter near a perfect mirror as a function of the separation distance z for three given frequencies.

one can generalize the previous discussion to any quantum emitter. In Figure 2.3 we plot the spectral enhancement as a function of the distance between the emitter and the

mirror for three given frequencies. As in the one-photon SE rate of an emitter near a perfectly conducting plate, $\gamma(\omega; z)$ also exhibits oscillations with the distance between the emitter and the plate. However, since in the TPSE there is an additional length scale, the oscillations are not as regular as in the one-photon SE, except when $\omega = \omega_t/2$, a particular case in which the two emitted photons are twins.

We finish this section by emphasizing that the TPSE spectral density function was written in terms of the one-photon Purcell factors of an emitter near a perfectly conducting mirror. Although this has been done in this particular case, this can be generalized, as we show in section 1.4.

2.2.2 TPSE of an emitter between two perfect mirrors

The suppression of spontaneous emission that was shown in the previous chapter is remarkable. However, what we referred to as suppression of spontaneous emission is, in fact, the suppression of the dipolar one-photon emission. Without a one-photon decay channel, in principle, the emitter can decay by the emission of a photon pair (here we are ignoring magnetic dipole transitions, electric quadrupole transitions and so on). However, since the TPSE is a second order process, the ratio between the lifetimes of an emitter which decays by two-photon emission and by the emission of a single photon is about 10^8 in free-space. Hence, when the one-photon SE is suppressed, the atom has a much greater lifetime.

In this subsection we investigate the TPSE in this same situation, namely, with the emitter between two perfectly conducting parallel plates (see Fig. 1.3). The field modes of this configuration are also given by Eqs. (1.8) and (1.9), but with $k_z = n\pi/L$, $n = 0, 1, 2, \dots$. The calculations can be carried out with the field modes approach, where the sum over k_z is now a discrete sum over the quantization indexes n . After performing all possible integrations, one can show that the spectral density for a $s \rightarrow s$ transition has exactly the form of Eq. (2.24), where the Purcell factors are now given by Eqs. (1.16)

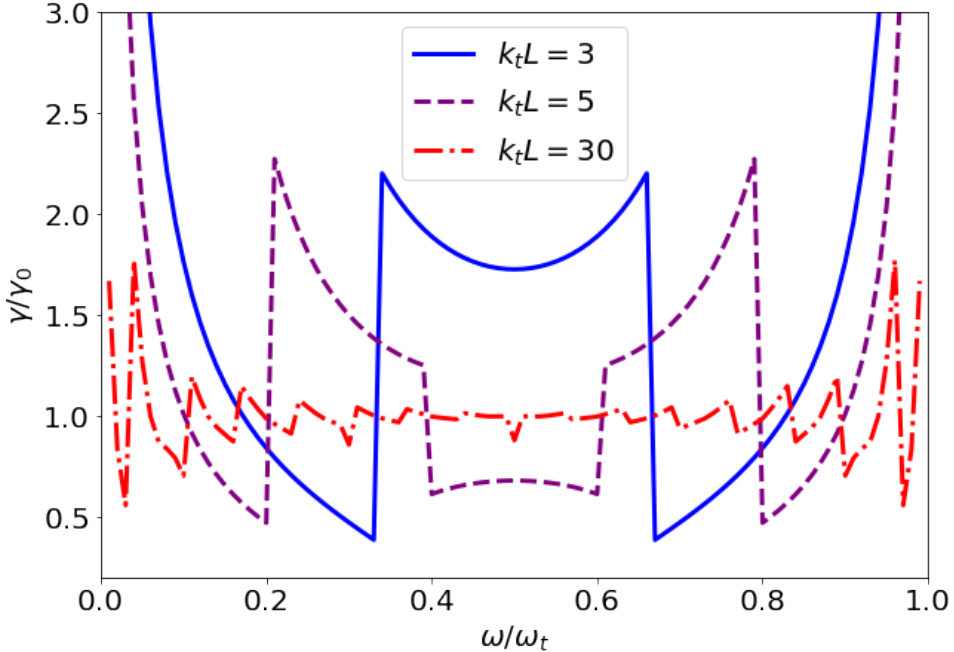


Figure 2.4: Spectral enhancement of an emitter equidistant from two perfect mirrors as a function of ω/ω_t for three given values of L .

and (1.15). We remember that P_1 and P_2 (or equivalently, Γ_{\parallel}) vanish for $L < \pi/k$, which means that the one-photon emission will be suppressed if the transition dipole moment is parallel to the plates. However, Eq. (2.24) shows that γ also depends on P_3 , which increases for small values of L . Therefore, it is clear that the TPSE is not completely suppressed in this situation unless $\mathbb{D}_{33} = 0$. For $s \rightarrow s$ and $d \rightarrow s$ transitions, which are the most common two-photon transitions, this can not be true due to the general form of \mathbb{D} [71]. Consequently, for these type of transitions complete suppression of the TPSE can never occur for an emitter between two parallel conducting plates.

In Figure 2.4 we plot the spectral enhancement for a $s \rightarrow s$ transition with the emitter equidistant from both plates, $\gamma(\omega, z = L/2)/\gamma_0(\omega)$, as a function of ω/ω_t for different values of L . Observe that complete suppression never occurs. Note also that the spectral enhancement diverges for $\omega \rightarrow 0$ and $\omega \rightarrow \omega_t$. This is a consequence of the fact that both $\gamma(\omega; z = L/2)$ and $\gamma_0(\omega)$ go to zero at these frequencies, but with different power laws. Furthermore, note that as L increases the spectral density function tends to the free space

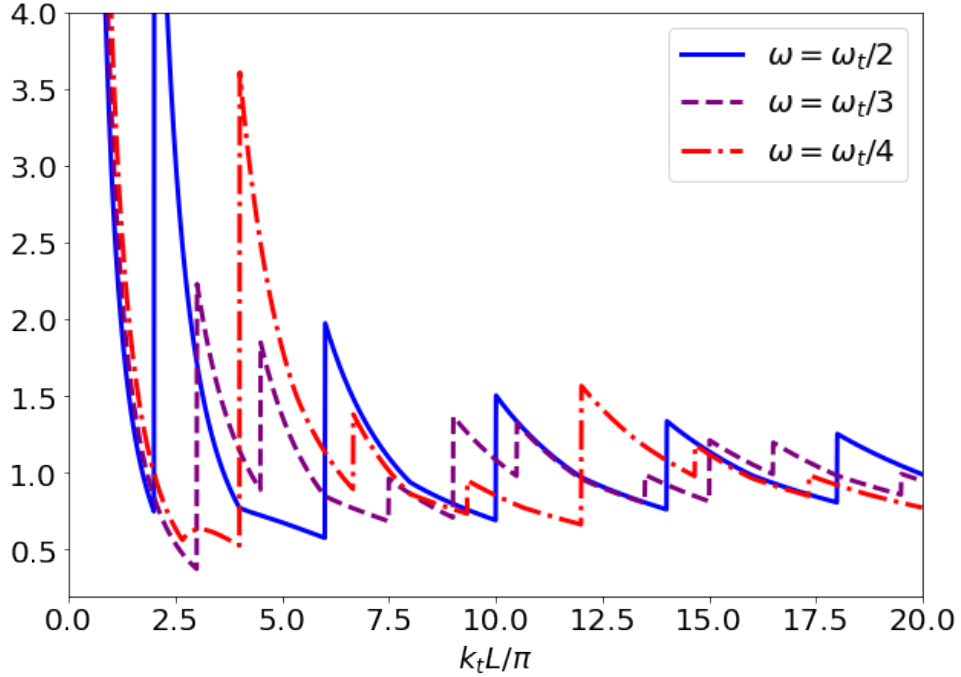


Figure 2.5: Spectral enhancement in terms of the dimensionless variable $k_t L / \pi$ with the emitter equidistant to both mirrors for three given frequencies.

spectral density function (dotted-dashed line), as expected, since in this case the plates do not influence the emitter anymore.

In Figure 2.5 we plot the spectral enhancement with the emitter equidistant from both plates, $\gamma(\omega, z = L/2) / \gamma_0(\omega)$, as a function of L for three given values of frequency. In analogy to what happens in the one-photon SE case, as the distance between the plates crosses certain multiples of kL/π , the number of available modes changes abruptly, giving rise to the discontinuities in the spectral density function. However, contrary to what happens in the one-photon SE case, total suppression never occurs. The non-suppression of the TPSE in this situation is a consequence of the fact that the spectral density function is not proportional to the partial LDOS, in contrast to what happens in the one-photon SE case [62]. As we can see from Eq. (2.3), the TPSE rate does not depend explicitly on the transition dipole moment, but on all the intermediate transition dipole moments.

2.3 Green's function approach

As shown in the previous chapter, another scheme for obtaining SE rates is by using the Green's function formalism. Here we follow a similar path to rewrite the TQSE rate given by Eq. (2.16) in terms of the Green's function, thus establishing an equivalence between our formula and the literature [10, 80]. With this purpose, first we recall that the dyadic Green's function admits a spectral representation where its imaginary part is given by Eq. (1.22). Noting that from Eq. (2.16) the TQSE rate can be written as

$$\begin{aligned} \Gamma(\mathbf{r}) = & \frac{\pi}{4\epsilon_0^2\hbar^2} \sum_{\alpha} \omega_{\alpha} (\omega_t - \omega_{\alpha}) \mathbf{A}_{\alpha}(\mathbf{r}) \cdot \mathbb{D}(\omega_{\alpha}, \omega_t - \omega_{\alpha}) \\ & \cdot \left[\sum_{\alpha'} \mathbf{A}_{\alpha'}(\mathbf{r}) \mathbf{A}_{\alpha'}^*(\mathbf{r}) \delta(\omega_{\alpha} + \omega_{\alpha'} - \omega_t) \right] \cdot \mathbb{D}^{\dagger}(\omega_{\alpha}, \omega_t - \omega_{\alpha}) \cdot \mathbf{A}_{\alpha}^*(\mathbf{r}) \end{aligned} \quad (2.25)$$

and using, for convenience, a simplified notation in which the \mathbf{r} dependence in the arguments of Γ , $\text{Im}\mathbb{G}$ and \mathbf{A}_{α} is implicit, we obtain from Eqs. (1.22) and (2.25)

$$\begin{aligned} \Gamma = & \frac{1}{2c^2\epsilon_0^2\hbar^2} \sum_{\alpha} \omega_{\alpha} (\omega_t - \omega_{\alpha})^2 \mathbb{D}_{ij}(\omega_{\alpha}, \omega_t - \omega_{\alpha}) \\ & \times \mathbb{D}_{lk}^*(\omega_{\alpha}, \omega_t - \omega_{\alpha}) \text{Im}\mathbb{G}_{jk}(\omega_t - \omega_{\alpha}) (\mathbf{A}_{\alpha})_i (\mathbf{A}_{\alpha}^*)_l. \end{aligned} \quad (2.26)$$

Using that $f(\omega_{\alpha}) = \int_{-\infty}^{\infty} d\omega f(\omega) \delta(\omega - \omega_{\alpha})$ we get

$$\begin{aligned} \Gamma = & \frac{\mu_0^2}{\pi\hbar^2} \int_0^{\omega_t} d\omega \omega^2 (\omega_t - \omega)^2 \text{Im}\mathbb{G}_{il}(\omega) \text{Im}\mathbb{G}_{jk}(\omega_t - \omega) \times \\ & \times \mathbb{D}_{ij}(\omega, \omega_t - \omega) \mathbb{D}_{lk}^*(\omega, \omega_t - \omega), \end{aligned} \quad (2.27)$$

where we used again Eq. (1.22) and constrained the limits of integration since $\text{Im}\mathbb{G}(\omega) = 0$ for $\omega < 0$. This equation can be viewed as an equivalent of (1.23) for the case of TQSE.

Although Eq. (2.27) has been derived from (2.16), which depends on the existence of a complete set of field modes, it is completely general and can be used to calculate the TQSE of an atom near any real material [80]. It is important to notice that Eq. (2.27)

also gives a general formula for the spectral density function $\gamma(\omega; \mathbf{r})$, namely.

$$\gamma(\omega; \mathbf{r}) = \frac{\mu_0^2}{\pi \hbar^2} \omega^2 (\omega_t - \omega)^2 \text{Im} \mathbb{G}_{il}(\omega) \text{Im} \mathbb{G}_{jk}(\omega_t - \omega) \mathbb{D}_{ij}(\omega, \omega_t - \omega) \mathbb{D}_{lk}^*(\omega, \omega_t - \omega). \quad (2.28)$$

2.3.1 Green's function approach to the emitter-mirror system

In order to compare the field modes approach with the Green's function method, we reobtain in this subsection the TPSE spectral density of an emitter close to a perfect mirror. With this purpose, it is convenient to write the Green function as $\mathbb{G}(\omega; \mathbf{r}, \mathbf{r}') = \mathbb{G}^{(0)}(\omega; \mathbf{r}, \mathbf{r}') + \mathbb{G}^{(sca)}(\omega; \mathbf{r}, \mathbf{r}')$, where $\mathbb{G}^{(0)}$ is the free space Green function and $\mathbb{G}^{(sca)}$ is a homogeneous solution of (1.17) satisfying the appropriate boundary conditions at the conducting surface. The calculation of the TPSE rate demands only the knowledge of the imaginary part of the Green's function at coincident points ($\mathbf{r}' = \mathbf{r}$). In this case, the free space Green function is given by $\text{Im} \mathbb{G}^{(0)}(\omega; \mathbf{r}, \mathbf{r}) = (\omega/6\pi c)\mathbb{I}$ and due to the translational symmetry of the system along any direction parallel to the Oxy plane, the scattered Green's function can be written as [62]

$$\begin{aligned} \mathbb{G}^{(sca)}(\omega; \mathbf{r}, \mathbf{r}) = & \frac{i}{8\pi k^2} \int_0^\infty dk_{\parallel} \frac{k_{\parallel}}{k_z} e^{2ik_z z} \times \\ & \times \begin{bmatrix} k^2 r^s - k_z^2 r^p & 0 & 0 \\ 0 & k^2 r^s - k_z^2 r^p & 0 \\ 0 & 0 & k_{\parallel}^2 r^p \end{bmatrix}, \end{aligned} \quad (2.29)$$

where $k_z = \sqrt{k^2 - k_{\parallel}^2}$ for $k_{\parallel} < k$, $k_z = i\sqrt{k_{\parallel}^2 - k^2}$ for $k_{\parallel} > k$ and r^p and r^s are the Fresnel reflection coefficients for p-polarized and s-polarized waves, respectively. For a perfect reflector, the Fresnel coefficients are given by $r^p = 1$ and $r^s = -1$. Taking the imaginary part of the previous equation and performing the integration in k_{\parallel} , we obtain

$$\begin{aligned} \text{Im} \mathbb{G}_{xx}(\omega) &= \text{Im} \mathbb{G}_{yy}(\omega) = \frac{\omega}{4\pi c} \times \\ &\times \left[-\frac{\sin(2kz)}{(2kz)} - \frac{\cos(2kz)}{(2kz)^2} + \frac{\sin(2kz)}{(2kz)^3} \right], \end{aligned} \quad (2.30)$$

$$\text{Im} \mathbb{G}_{zz}(\omega) = \frac{\omega}{2\pi c} \left[-\frac{\cos(2kz)}{(2kz)^2} + \frac{\sin(2kz)}{(2kz)^3} \right]. \quad (2.31)$$

Using previous expressions into Eq. (2.27) and identifying the integrand as the spectral density function, we recover the result given by equation (2.23).

Though the two methods are equivalent, it is worth noting that to identify the angular distribution of the emitted photons by using the Green's function method is not an easy task as it is in the framework of the field modes approach. Besides, although the calculation of the TPSE rate by using the Green's function method is in principle straightforward, this procedure may obscure the basic underlying physics of the problem. For some systems, the field modes approach may even emphasize some physical aspects that are not evident in the Green's function method, as for instance when the system supports different types of modes and the emitter might de-excite by different pathways. However, in more general situations the field modes framework is not suitable, such as the case of plasmonic materials and dissipative systems in general.

2.4 The Purcell factors relation

Now, we shall relate the TQSE spectral density function of an emitter near a surface to the one-photon SE rate in the same situation. In a previous work, this has been shown by considering the emitter near a planar interface [14]. In the following derivation we will not assume this restriction and will consider the emitter near a surface with an arbitrary shape. This is possible by noting that $\text{Im}\mathbb{G}(\omega)$ is a real and symmetric matrix [63], which means it can be diagonalized. For systems where the basis which diagonalizes the imaginary part of the Green's function does not depend on frequency, one can rewrite Eq. (2.27) as

$$\Gamma = \int_0^{\omega_t} d\omega \gamma_0(\omega) \sum_{a,b} t_{ab}(\omega) P_a(\mathbf{r}, \omega) P_b(\mathbf{r}, \omega_t - \omega), \quad (2.32)$$

where $t_{ab}(\omega) = |\mathbb{D}_{ab}(\omega, \omega_t - \omega)|^2 / |\mathbb{D}(\omega, \omega_t - \omega)|^2$ and we defined the Purcell factors P_a 's, $a = 1, 2, 3$, as

$$P_a(\mathbf{r}, \omega) := \frac{6\pi c}{\omega} \text{Im}\mathbb{G}_{aa}(\omega; \mathbf{r}, \mathbf{r}). \quad (2.33)$$

This equation is a generalization of Eq. (2.23) for an arbitrary material body. Note that the Purcell factors coincide with the ratio (1.23) if we choose $\hat{\mathbf{n}}_t = \hat{\mathbf{e}}_a(\mathbf{r})$, i.e., the transition dipole moment oriented along one of the basis vectors. It is important to note that when the basis which diagonalizes the Green's function is frequency-dependent Eq. (2.32) does not hold. On the other hand, this equation establishes an explicit relation between TQSE and one-quantum SE, hence, showing in a very clear way the dependence of the TQSE rate on the local density of states.

2.4.1 An emitter near a half-space dielectric medium

Using the Purcell factors relation just presented, we determine as an example the spectral enhancement of the TQSE of an emitter near a semi-infinite homogeneous dielectric dispersive medium ($z < 0$). It is clear that Eq. (2.32) gives a straightforward way to compute $\gamma(\omega; \mathbf{r})$ since, in this situation, the cartesian basis diagonalizes the Green's function and the corresponding formulas for the one-quantum SE rates are well known. Moreover, as before, we consider only $s \rightarrow s$ transitions. In this case, the corresponding spectral enhancement is given by equation (2.24) with P_x and P_y given by Eq. (1.33) and P_z by Eq. (1.32). Here, we restrict ourselves to the near-field regime. Evoking the Lorentz model for dielectrics given by Eq. (1.36), we expect a strong dependence of the LDOS on the dielectric resonance frequencies, as a dielectric behaves like a metal for waves with frequencies close to the resonances. Hence, applying Eq. (2.32) we expect a substantial enhancement in the spectral density function near the resonance frequencies.

In Figure 2.6 we plot the spectral enhancement for three given distances between the emitter and the dielectric for an $s \rightarrow s$ transition. We considered a Polystyrene medium described by a Lorentz model with two resonance frequencies. First, note the huge changes on the spectral density function near the resonance frequencies ω_{R1} and ω_{R2} . Since the relaxation time is such that $1/\tau \ll \omega_{R1}, \omega_{R2}$, the transition between the two frequency regimes (before and after each resonance) occurs in a very narrow interval.

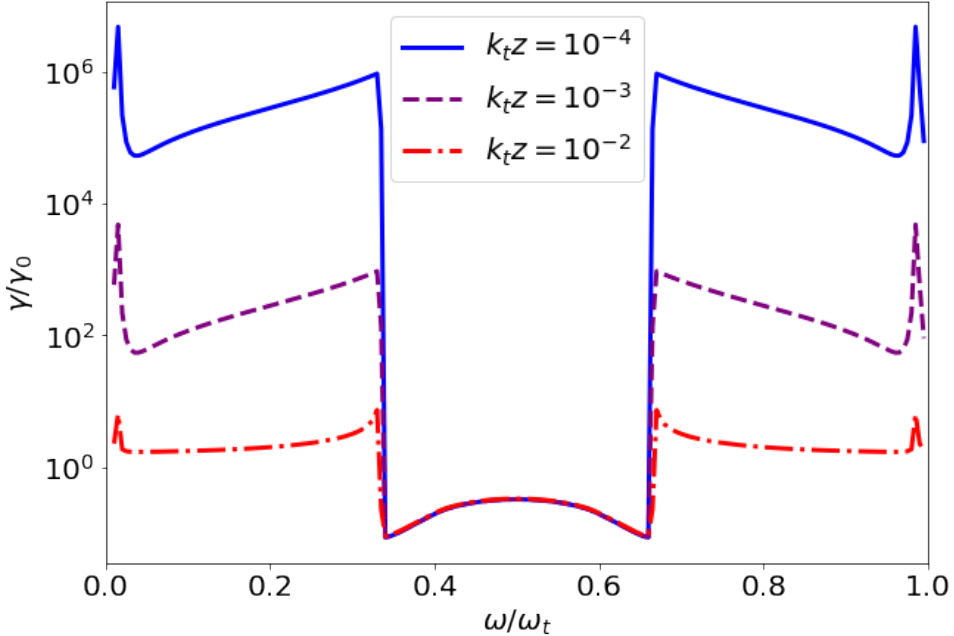


Figure 2.6: Spectral enhancement of an emitter near a half-space Polystyrene medium as a function of ω/ω_t for three given values of z . The Polystyrene resonance frequencies are given by $\omega_{R1} = 5.54 \times 10^{14}$ rad/s and $\omega_{R2} = 1.35 \times 10^{16}$ rad/s and the corresponding relaxation time by $\tau = 10^{-11} s^{-1}$ [1]. The emitter transition frequency was chosen as $3\omega_{R2}$.

Due to the symmetry of the spectral distribution with respect to $\omega_t/2$, the same behavior occurs near the complementary frequencies $\omega_t - \omega_{R1}$ and $\omega_t - \omega_{R2}$. As it is evident from the figure, the spectral distribution may be orders of magnitude greater than its free space value, since we are in the near field regime. Furthermore, as the frequency of the emitted quantum excitation approaches a given resonance frequency from below, the spectral density increases monotonically until it reaches a maximum value, and then suffers an abrupt decrease as it crosses the resonance frequency. This result highlights the possibility of controlling the spectral distribution of TQSE by tuning the resonance frequencies of a medium. In the next chapter, we benefit of this basic understanding of TQSE in order to explore more complex systems. In all cases, we will use the Purcell factors relation together with the idea of enhancing the TQSE by tuning the resonances of the material obtained by studying this simple situation.

Chapter 3

Two-quanta spontaneous emission in low-dimensional plasmonic materials

Plasmonics is the study of interaction processes between electromagnetic radiation and conduction electrons in metallic interfaces [9]. It also plays an important role on the fascinating field of nanophotonics, which focus on the behavior of light at the nanoscale and its interaction with nanoparticles. The field of plasmonics is more than a hundred years old, with the first description of surface plasmon polaritons and localized surface plasmons dating back to the beginning of the 20th century [81–83]. In his seminal paper [81, 84], A. Sommerfeld developed a rigorous theory of waves traveling on a resistive wire of finite radius and revealed the existence of surface waves that decay exponentially with the radial distance from the wire, the so called surface plasmons. Despite its age, research in plasmonics has witnessed a fast-growing expansion in the last decades due to its wide range of potential applications, such as solar cells [85, 86], high-resolution microscopy [87, 88], and biosensors [89–92].

Regarding the SE phenomenon, it is well known that the subwavelength light confinement offered by surface plasmon-polaritons (SPPs) significantly enhances the decay rate of a quantum emitter in the near field [93–96]. Therefore, the potential of plasmonic materials to achieve high two-plasmon decay rates is undeniable and deserves a careful study. Indeed, an impressive increase of the TQSE rate is observed by engineering the local density

of optical states (LDOS) in nanostructured electromagnetic environments, such as planar photonic systems [77], optical cavities [97], phonon-polaritons dielectric systems [14], and aperiodic bandgap structures [98]. For instance, plasmon-assisted collective TQSE has been observed in bulk semiconductors coupled to nanoantenna arrays [99] with radiative emission enhancement of a few tens. Remarkably, by tailoring the LDOS in plasmonic and polaritonic sub-wavelength electromagnetic nanostructures one may achieve TQSE rates that are orders of magnitude larger than one-photon spontaneous emission rates [14].

Meanwhile, low-dimensional materials like graphene have emerged in this century and attracted the scientific community towards them [100]. Graphene is a two-dimensional material made of carbon atoms in a honeycomb structure that possess tunable and adjustable intrinsic plasmons [101, 102]. Furthermore, these plasmons present some unusual properties and offer an extremely high efficiency for light-matter interactions, which was already exploited to increase and tailor one- [47, 103] and two-plasmon [10] SE. Beyond extended monolayers, graphene nanostructures and carbon nanotubes [104] show even more interesting properties such as localized and guided surface plasmons that may resonate with a quantum emitter in the near field [49, 105]. But low-dimensional plasmonic materials are not restricted to graphene. Recent advances in the fabrication of metallic thin films brought low-dimensional noble metals to the game [106, 107]. For these atomically thin metallic materials, plasmons may exist in the optical frequency domain [108], and exciting ideas for controlling the generation of visible light are at hand.

In this chapter we propose novel approaches for enhancing and tuning the TQSE using low-dimensional plasmonic materials. In the first section we introduce the key features of one- and two-plasmon SE by considering the well known example of a quantum emitter close to a graphene monolayer. In section II we study TQSE in carbon based nanowires such as single-walled carbon nanotubes and graphene coated dielectric wires. In section III we take a step further by investigating the TQSE of a quantum emitter near finite-sized atomically thin plasmonic nanostructures. In this case, we go beyond graphene and also

consider metallic nanostructures. As we demonstrate, this is an excellent material platform to harness the two-photon spontaneous emission and generate on-demand entangled photons.

3.1 Tunable two-quanta spontaneous emission with graphene

In this section we present a brief study of TQSE near a graphene monolayer. In order to investigate this phenomenon we must first discuss the electromagnetic properties of graphene, which derive from its unique band structure. Graphene's band structure is such that the valence and conduction bands touch each other in six points of the Brillouin zone, also known as Dirac Points [109]. For energies close to these points, the valence and conduction bands are conical, and the electronic dispersion relation is approximately given by $E_{\pm}(\mathbf{q}) \approx \pm 3ta|\mathbf{q}|/2 = v_F\hbar q$, where $t \approx -2.7$ eV is the hopping coupling energy, $a \approx 1.42$ Å is the lattice constant, and $v_F \approx c/300$ the Fermi velocity. For this reason, electrons in graphene can be thought as massless electrons and satisfy the Dirac equation [110] with $m = 0$. This feature has important consequences, some of them related to the dispersion relation of plasmons in graphene, which has the unique property of being proportional to $n_e^{1/4}$ [111], with n_e being the electronic carrier density.

Graphene conductivity is a key ingredient to understand its optical properties since it contains all relevant information to describe electromagnetic interactions. An analytical expression for the conductivity can be obtained within the context of linear response theory [112] and computed using the Kubo formula [113–116]. The conductivity can be written as $\sigma = \sigma_{\text{intra}} + \sigma_{\text{inter}}$, where σ_{intra} is the contribution of intraband transitions, i.e., electronic transitions between states belonging to the same band (valence or conduction), and σ_{inter} is the contribution of interband transitions. The intra- and interband contributions are given by

$$\sigma_{\text{intra}}(\omega) = \frac{\sigma_0}{\pi} \frac{4}{\hbar\gamma - i\hbar\omega} [E_F + 2k_B T \log(1 + e^{-E_F/k_B T})], \quad (3.1)$$

$$\sigma_{\text{inter}}(\omega) = \sigma_0 \left[G(\hbar\omega/2) + i \frac{\hbar\omega}{\pi} \int_0^\infty dE \frac{G(E) - G(\hbar\omega/2)}{(\hbar\omega/2)^2 - E^2} \right], \quad (3.2)$$

where E_F is the Fermi energy, k_B is the Boltzmann constant, T is the temperature, and the relaxation rate is given by $\gamma = ev_F^2/\mu E_F$, with μ being the electron mobility. Also, $\sigma_0 = e^2/(4\hbar)$ is the conductivity of a zero-temperature undoped ($E_F = 0$) graphene monolayer and

$$G(x) = \frac{\sinh\left(\frac{x}{k_B T}\right)}{\cosh\left(\frac{E_F}{k_B T}\right) + \cosh\left(\frac{x}{k_B T}\right)}. \quad (3.3)$$

We notice that, for sufficiently small temperatures ($k_B T \ll E_F$), the intraband contribution is given by

$$\sigma_{\text{intra}}(\omega) \approx \frac{\sigma_0}{\pi} \frac{4E_F}{\hbar\gamma - i\hbar\omega}, \quad (3.4)$$

which is the Drude conductivity of graphene with plasma frequency $\omega_p = \sqrt{e^2 n_e / m_e \epsilon_0}$, with m_e being the electron mass. Furthermore, the interband contribution is negligible at small frequencies ($\hbar\omega < 2E_F$), which derives from the fact that, in this regime, there is not enough energy to excite an electron from the valence band to the conduction band. As a consequence, graphene behaves as a conductive material and supports surface plasmon-polaritons (SPPs). On the other hand, for $\hbar\omega > 2E_F$ the interband term is higher, which results in electron-hole pair excitations instead of SPPs. Finally, we notice that the conductivity depends on the Fermi energy, which can be modified with chemical doping or by an applied gate voltage [101, 117, 118]. For this reason, graphene is an active material whose optical response can be dynamically controlled.

3.1.1 Graphene Fresnel coefficients and Purcell factors

Consider a quantum emitter separated by a distance z from an infinite graphene sheet. Due to the plane geometry of the system, the Purcell factors are given by the same expres-

sions derived in section 1.2.2, namely, Eqs. (1.32) and (1.33). Nevertheless, the Fresnel coefficients must be replaced by the graphene reflection coefficients. As usual, these coefficients can be derived by solving a plane-wave reflection problem. Since graphene is a 2D material, its presence can be modelled by considering its induced charge and current densities as the boundary conditions, namely, $\mathbf{K}(\mathbf{r}, \omega) = \sigma(\omega)\mathbf{E}_{\parallel}(\mathbf{r}, \omega)$ (Ohm's law) and $i\omega\rho_{2D}(\mathbf{r}, \omega) = \nabla_{\mathbf{r}} \cdot \mathbf{K}(\mathbf{r}, \omega)$ (continuity equation). Considering a graphene monolayer over a dielectric substrate of permittivity ϵ , the Fresnel coefficients can be written as [109]

$$r^s = \frac{k_z - k_{z1} + \mu_0\omega\sigma}{k_z + k_{z1} + \mu_0\omega\sigma}, \quad (3.5)$$

$$r^p = \frac{\epsilon k_z - \epsilon_0 k_{z1} + k_z k_{z1}/\epsilon_0\omega}{\epsilon k_z + \epsilon_0 k_{z1} + k_z k_{z1}\sigma/\epsilon_0\omega}, \quad (3.6)$$

where k_z is given by Eq. (1.28), and $k_{z1} = \sqrt{\mu_0\epsilon\omega^2 - k_{\parallel}^2}$.

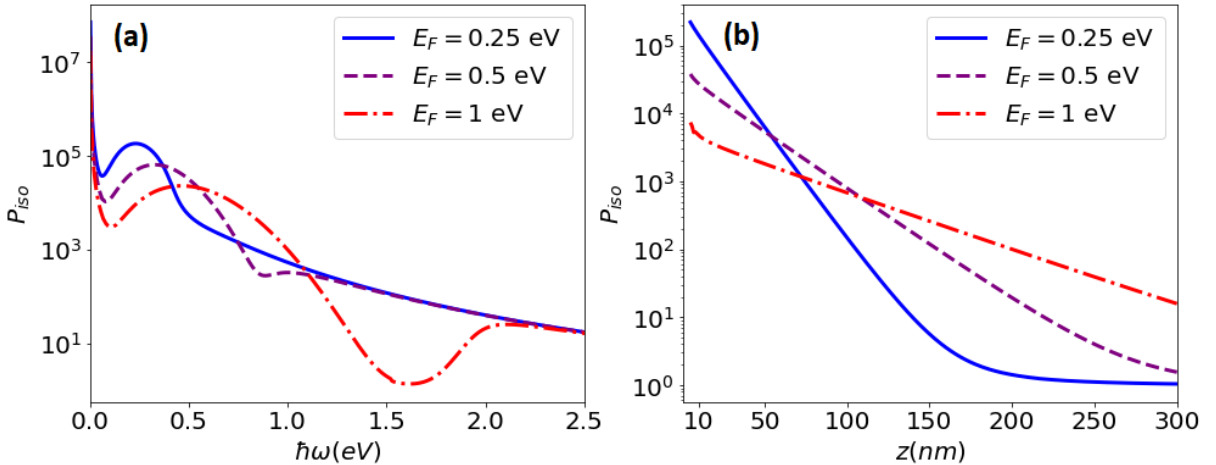


Figure 3.1: **(a)** Isotropic Purcell factor $P_{iso} = (P_x + P_y + P_z)/3$ of a quantum emitter placed a distance $z = 10$ nm from a suspended graphene sheet as a function of its transition energy. **(b)** Isotropic Purcell factor as a function of the distance between the emitter and the monolayer. The transition energy is given by the $6s \rightarrow 5p$ transition in hydrogen, $\hbar\omega_t \approx 166$ meV. Both plots were computed considering graphene at room temperature ($T = 300$ K) with an electron mobility of $\mu = 2500$ cm 2 V $^{-1}$ s $^{-1}$.

In Fig. 3.1a we plot the Purcell factor of an isotropic atom 10 nm distant from a suspended ($\epsilon = \epsilon_0$) graphene monolayer as a function of the transition energy. We observe two important regimes. For $\hbar\omega < 2E_F$ the emitter couple with the graphene

SPPs and the SE is significantly enhanced in this region. Moreover, the enhancement in the low-frequency regime is higher at smaller values of the Fermi energy. However, since graphene plasmons do not exist for $\hbar\omega > 2E_F$, the most relevant decay pathway available in this regime is the electron-hole pair creation. As a result, the Purcell factor decays exponentially with the transition frequency. Since we are interested in the plasmon-emitter coupling, in the subsequent discussions we will always consider the first case (unless stated otherwise). In Fig. 3.1b we plot the Purcell factor as a function of distance for the $6s \rightarrow 5p$ transition in hydrogen ($\hbar\omega_t \approx 166$ meV). We observe an exponential decay of the Purcell factor with the distance, which is a well-known behaviour of the plasmon-emitter interaction in metals. Also, the decay is faster for small doping values.

3.1.2 Two-plasmon spontaneous emission

Now we turn our attention to the two-plasmon SE of a quantum emitter close to suspended graphene. In order to obtain the two-plasmon SE spectrum and global decay rate, we can use Eq. (2.32) together with the Fresnel coefficients and Purcell factors calculated in the previous section. In Fig. 3.2 we plot the normalized spectrum of emission of the $6s \rightarrow 5s$ transition in hydrogen for $E_F = 0.25, 0.5, 1$ eV. We notice that the two-plasmon emission spectrum is broadly enhanced since the graphene SPPs exist in all possible frequencies of emission. As a consequence, the two-plasmon decay rate is also significantly enhanced. Indeed, one can observe that the spectral enhancement of the two-plasmon emission is roughly the square of the one-plasmon SE increase presented in Fig. 3.1a, which derives from the fact that $\gamma \sim P^2$.

The TQSE rate of this configuration can be calculated with a numerical integration of the spectral enhancement multiplied by the free-space $6s \rightarrow 5s$ spectral density, namely, γ_0 . This quantity can be obtained after inserting the numerical expressions of the hydrogen wavefunctions into Eq. (2.15). After doing that, we find a two-plasmon emission rate $\sim 5.3 \times 10^{10}$ times higher than the free-space one for $E_F = 0.25$ eV, which corresponds

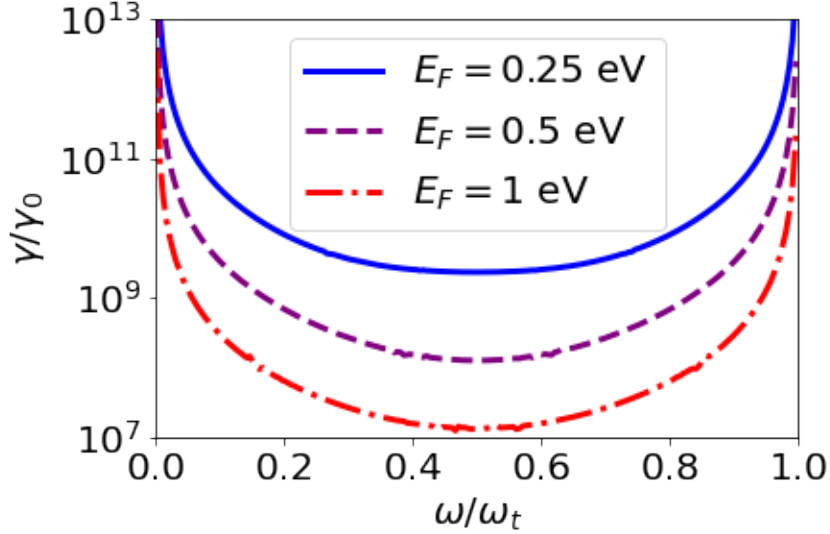


Figure 3.2: Spectral enhancement of an emitter placed at a distance $z = 10$ nm from a suspended graphene monolayer as a function of ω/ω_t for three given values of E_F . The emitter transition energy was chosen as 166 meV, which corresponds to the $6s \rightarrow 5s$ transition frequency in hydrogen.

to a lifetime of ~ 400 ns that contrasts with the free-space lifetime of a few days for this specific transition.

A comment is in order here. The $6s \rightarrow 5s$ transition is not the only possible decay pathway available. There are competing one-plasmon transitions and even other possible two-plasmon paths that could also be enhanced and dominate the spontaneous decay. For this reason, it is convenient to define a quantity called the quantum efficiency as

$$\text{QE}_{n_il_i \rightarrow n_f l_f} = \frac{\Gamma_{n_il_i \rightarrow n_f l_f}}{\Gamma_{n_il_i \rightarrow n_f l_f} + \sum_{n'l'} \Gamma_{n_il_i \rightarrow n'l'} + \Gamma_{n_il_i \rightarrow n'l'}^{1q}}, \quad (3.7)$$

where $\Gamma_{n_il_i \rightarrow n_f l_f}$ is the TQSE rate of the considered transition, $\Gamma_{n_il_i \rightarrow n'l'}$ are the TQSE rates to other $n'l'$ available decay pathways, and $\Gamma_{n_il_i \rightarrow n'l'}^{1q}$ are the competing one-quantum SE rates. Notice that, due to selection rules, $\Gamma_{n_il_i \rightarrow n'l'}$ and $\Gamma_{n_il_i \rightarrow n'l'}^{1q}$ cannot be different from zero for the same states. The quantum efficiency can be interpreted as the probability of emission through the chosen pathway taking into account all other relevant decays. Since the most relevant alternative decay pathways correspond to one-photon spontaneous emission decays, we can ignore the contribution of other TQSE processes and calculate

the quantum efficiency of the $6s \rightarrow 5s$ transition as

$$QE_{6s \rightarrow 5s} \approx \frac{\Gamma_{6s \rightarrow 5s}}{\Gamma_{6s \rightarrow 5s} + \Gamma_{6s \rightarrow 5p}^{1q} + \Gamma_{6s \rightarrow 4p}^{1q} + \Gamma_{6s \rightarrow 3p}^{1q} + \Gamma_{6s \rightarrow 2p}^{1q}}, \quad (3.8)$$

For the considered case of an atom 10 nm distant from a suspended graphene with $E_F = 0.25\text{eV}$ we have a quantum efficiency of $\sim 1.9\%$, which is similar to the value reported in [10]. The meaning of this result is that if we repeat the experiment of exciting an atom close to graphene to the $6s$ state multiple times, we should measure two-plasmon emission to the $5s$ state only in approximately 2% of the experiments. Nevertheless, we must mention that the quantum efficiency in free-space is of the order of $10^{-8}\%$ for this transition. Therefore, the strong interaction offered by graphene plasmons brings both phenomena (one- and two-plasmon SE) much more closer to each other regarding their probabilities. This feature will be explored even more in the next sections.

3.2 Two-plasmon spontaneous emission in one-dimensional carbon nanostructures

In this section we introduce two carbon-based nanomaterial platforms to tailor two-plasmon SE processes, namely single-walled carbon nanotubes (SWCNT) and graphene-coated wires (GCWs). Given their lower dimensionality, these systems are even more efficient for generating and detecting entangled plasmons in comparison to extended graphene. Indeed, we demonstrate that the strong coupling between tunable guided plasmons and the quantum emitter allows for efficient generation of two-plasmon guided entangled states [119]. These carbon nanostructures also enable unprecedented control over spectral lineshapes of emission due to the coupling with different plasmonic modes supported by their cylindrical geometry, and may be useful for applications to on-chip quantum information technologies.

3.2.1 Quasi-static approximation modelling

Consider a quantum emitter separated by a distance d from an infinitely long nanowire

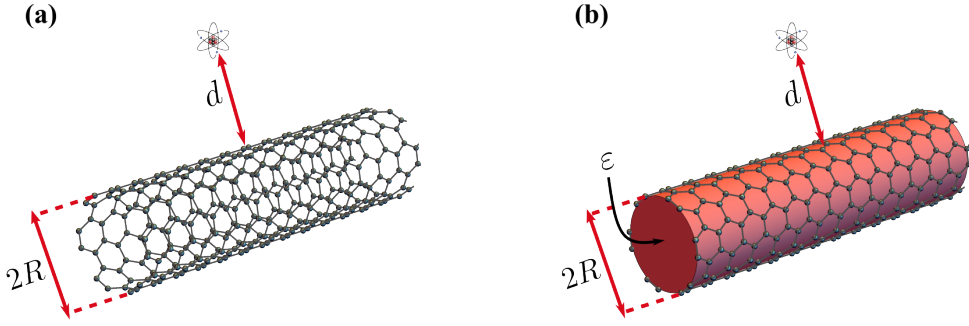


Figure 3.3: Schematics of the system under study. (a) A quantum emitter separated by a distance d from a SWCNT of radius R . (b) A quantum emitter separated by a distance d of a dielectric cylinder of relative electric permittivity ε and radius R , coated with graphene.

of radius R . The surface of the wire is graphene while its inner region may be empty (for the case of a SWCNT) or filled with a dielectric medium of relative electric permittivity ε (for a GCW), as shown in Figs. 3.3a and 3.3b. The rotational and translational symmetries with respect to the nanowire axis allow for the diagonalization of the imaginary part of the electromagnetic Green's tensor in the frequency-independent basis $\{\hat{\rho}, \hat{z}, \hat{\phi}\}$ (the basis vectors in cylindrical coordinates). Hence, we are allowed to use Eq. (2.32) and calculate the TQSE spectrum in terms of the Purcell factors of the system.

The Purcell factors can be obtained using Eq. (1.25), i.e., by calculating the electric field of an oscillating dipole near the nanowire. The scattered field can be split as $\mathbf{E}^{(sca)}(\mathbf{r}) = \mathbf{E}_R(\mathbf{r})$ for $\rho > R$ and $\mathbf{E}^{(sca)}(\mathbf{r}) = \mathbf{E}_T(\mathbf{r})$ for $\rho < R$. Here, \mathbf{E}_R and \mathbf{E}_T are the fields reflected and transmitted by the carbon nanostructure, respectively. The task of finding the general expression of the electric field is hard, but not impossible [105]. However, here we shall calculate the field in the quasi-static approximation, which is sufficient since we are considering transitions with wavelengths much larger than the geometrical parameters of the system, i.e., $\lambda \gg R, d$ [102, 120, 121]. In this approximation, the dynamical terms of the Maxwell equations are neglected and we can use the relation between the electrostatic field of a point dipole and the scalar electrostatic potential of a

unitary electric charge (Φ), namely $\mathbf{E}(\mathbf{r}) = -\nabla(\mathbf{p}_a \cdot \nabla)\Phi(\mathbf{r})$. Here, Φ satisfies the Poisson equation $\nabla^2\Phi(\mathbf{r}) = \delta(\mathbf{r} - d\hat{\rho})/\varepsilon_0$ and the boundary conditions regarding the continuity of the parallel component of the electric field, $[\mathbf{E}_0(R) + \mathbf{E}_R(R) - \mathbf{E}_T(R)] \times \hat{\rho} = \mathbf{0}$ with \mathbf{E}_0 being the electrostatic field of the point dipole in free-space, and the discontinuity of its perpendicular component due to the induced surface charge density, $[\mathbf{E}_0(R) + \mathbf{E}_R(R) - \varepsilon\mathbf{E}_T(R)] \cdot \hat{\rho} = \rho_{2D}/\varepsilon_0$. The induced surface charge can be obtained by combining Ohm's law, $\mathbf{K}(\mathbf{r}, \omega) = \sigma(\omega)\mathbf{E}_{\parallel}(\mathbf{r}, \omega)$, with the continuity equation, $i\omega\rho_{2D}(\mathbf{r}, \omega) = \nabla_{\mathbf{r}} \cdot \mathbf{K}(\mathbf{r}, \omega)$, which yields

$$\rho_{2D}(\mathbf{r}) = \frac{-i\sigma}{\omega} \nabla \cdot [f(\mathbf{r})\mathbf{E}_{\parallel}(\mathbf{r})], \quad (3.9)$$

where σ is the graphene conductivity and $f(\mathbf{r})$ is a filling function which is equal to 1 when the position vector \mathbf{r} lies within the surface of the nanowire and 0 elsewhere. We assume that R is sufficiently large ($\gtrsim 1$ nm) so that we can neglect finite-size and chirality effects of the nanotube [102]. By expanding the potential in cylindrical coordinates and applying the boundary conditions one finds

$$\Phi_0(\mathbf{r}) = \sum_{m=0}^{\infty} \frac{b_m \cos(m\theta)}{2\pi^2\varepsilon_0} \int_0^{\infty} dk \cos(kz) I_m(k\rho) K_m(k\rho_d), \quad (3.10)$$

$$\Phi_R(\mathbf{r}) = \sum_{m=0}^{\infty} \frac{b_m \cos(m\theta)}{2\pi^2\varepsilon_0} \int_0^{\infty} dk r_m \cos(kz) K_m(k\rho) K_m(k\rho_d), \quad (3.11)$$

$$\Phi_T(\mathbf{r}) = \sum_{m=0}^{\infty} \frac{b_m \cos(m\theta)}{2\pi^2\varepsilon_0} \int_0^{\infty} dk t_m \cos(kz) I_m(k\rho) K_m(k\rho_d), \quad (3.12)$$

where $b_m = 2 - \delta_{m0}$, $\rho_d = R + d$, I_m and K_m are the modified Bessel functions of the first and second kind, respectively, and the reflection (r_m) and transmission (t_m) Fresnel coefficients are given by

$$r_m = -\frac{(\varepsilon - 1)I_m I'_m kR + \Delta_m I_m^2}{(\varepsilon I'_m K_m - I_m K'_m)kR + \Delta_m I_m K_m}, \quad (3.13)$$

$$t_m = 1 + \frac{K_m}{I_m} r_m, \quad (3.14)$$

with $\Delta_m = (i\sigma/\varepsilon_0\omega R)(m^2 + k^2R^2)$, the Bessel functions being evaluated at kR , and the prime represents derivative with respect to the argument. Finally, we can use the

previous expression for the reflected scalar potential to calculate the reflected electric field and obtain the Purcell factors from Eq. (1.25) for each relevant dipolar orientation as follows

$$P_\rho(d, \omega) = 1 - \sum_{m=0}^{\infty} \frac{3c^3 b_m}{\pi \omega^3} \int_0^{\infty} dk k^2 \text{Im}\{r_m\} [K'_m(k\rho_d)]^2, \quad (3.15)$$

$$P_z(d, \omega) = 1 - \sum_{m=0}^{\infty} \frac{3c^3 b_m}{\pi \omega^3} \int_0^{\infty} dk k^2 \text{Im}\{r_m\} K_m^2(k\rho_d), \quad (3.16)$$

$$P_\phi(d, \omega) = 1 - \sum_{m=1}^{\infty} \frac{6c^3 m^2}{\pi \rho_d^2 \omega^3} \int_0^{\infty} dk \text{Im}\{r_m\} K_m^2(k\rho_d). \quad (3.17)$$

It is important to mention that the previous equations apply to both SWCNT and GCW cases considered here, with SWCNTs being the particular case of $\varepsilon = 1$. By using the Wronskian identity $I'_m(x)K_m(x) - I_m(x)K'_m(x) = 1/x$ [122], we can reobtain the simpler expression of the reflection coefficient of a SWCNT derived in [105], namely

$$r_m = -\frac{\Delta_m I_m^2}{1 + \Delta_m I_m K_m}. \quad (3.18)$$

The plasmon dispersion relations are given by the poles of the Fresnel coefficients [123], which can be obtained by solving the following transcendental equation,

$$\frac{(m^2 + k^2 R^2) I_m K_m}{(\varepsilon I'_m K_m - I_m K'_m) k R} = \frac{i \varepsilon_0 \omega R}{\sigma(\omega)}. \quad (3.19)$$

When we consider the Drude model for the graphene conductivity given by Eq. (3.4), in the limit of small dissipation ($\gamma \rightarrow 0$), the free-space oscillation frequency can be directly expressed in terms of the plasmon wavevector as

$$\hbar \omega_m(k) = \sqrt{\frac{e^2 E_F}{\pi \varepsilon_0 R} \times \frac{(m^2 + k^2 R^2) I_m K_m}{(\varepsilon I'_m K_m - I_m K'_m) k R}}. \quad (3.20)$$

This equation gives the energy required to excite the plasmonic mode m with propagation wavevector k . Since each guided plasmon can be supported regardless of the value of k , by taking the limit $k \rightarrow 0$ we get the minimum amount of energy required to excite the plasmonic mode m . Using the appropriate Taylor expansions for the modified Bessel

functions and taking this limit, we find

$$\hbar\omega_m^{(\min)} = \sqrt{\frac{e^2 E_F m}{(1 + \varepsilon) \pi \varepsilon_0 R}}. \quad (3.21)$$

From the previous equation, we conclude that the fundamental mode ($m = 0$) can be excited at any oscillation frequency, while other modes require some amount of energy to exist. Such a difference can be explained by their non-trivial angular profile [124], which imposes a constraint over the plasmon's wavelength λ_g^ϕ across the ϕ -direction, namely, $m\lambda_g^\phi = 2\pi R$. This can be demonstrated by inserting $k_g = 2\pi/\lambda_g^\phi = m/R$ into the plasmon's dispersion relation of the extended graphene in the quasi-static approximation, given by $\hbar\omega_g = \sqrt{e^2 E_F k_g / (1 + \varepsilon) \pi \varepsilon_0}$ [125]. As a consequence of Eq. (3.21), depending on the geometric and material properties of the wire, different plasmonic modes contribute to the TPSE spectrum of emission. In short, every mode with $\omega_m^{(\min)} < \omega_t$ contributes to the spectrum, which can be tuned by modifying the system's properties such as the wire radius, the Fermi energy, or even the relative permittivity by a proper choice of the inner dielectric medium.

3.2.2 Two-plasmon spontaneous emission near carbon nanotubes

In this section, we consider the case of an emitter near a SWCNT ($\varepsilon = 1$), shown in Fig. 3.3a. SWCNTs typically have diameters in the range of a few nanometers [126], which imposes constraints regarding the appearance of non-fundamental plasmonic modes in the two-plasmon SE spectrum. Indeed, let us consider a large nanotube of radius $R = 5$ nm, which is at the limit of what can be achieved with the state-of-the-art nanofabrication techniques [127]. From Eq. (3.21) the minimum excitation energy of the 1st-order mode for $E_F = 500$ meV is given by $\hbar\omega^{(\min)} \sim 537$ meV, which may induce interband transitions in the nanotube instead of exciting plasmons. Even if the Fermi energy is increased to 1 eV, the first mode only exists above 760 meV, which is near the limit of the mid-infrared spectral range where plasmons have been shown to exist for graphene. Any other mode

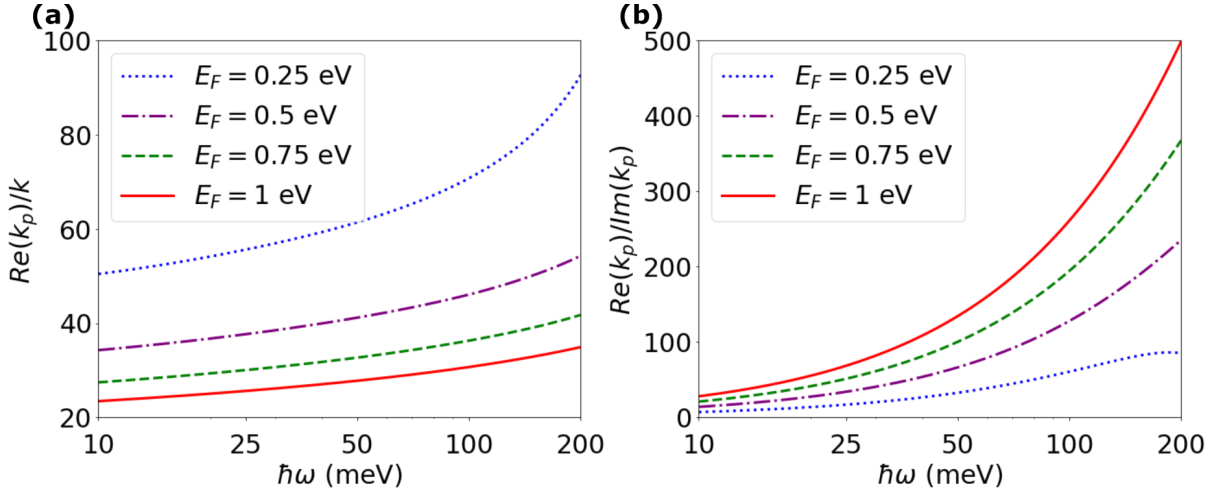


Figure 3.4: **(a)** Real part of the plasmon’s wavevector k_p for the fundamental mode ($n = 0$) normalized by the free-space wavevector $k = \omega/c$ as a function of the light oscillation frequency for different values of the Fermi energy. **(b)** The ratio between the real and imaginary parts of k_p of the fundamental plasmonic mode versus the free-space frequency for different values of the Fermi energy.

has an excitation frequency in the regime dominated by interband transitions for any value of the Fermi energy and, consequently, would not show up in the two-plasmon SE spectral lineshapes. For this reason, the fundamental mode dominates the two-plasmon SE spectrum of an emitter near a SWCNT. In all subsequent discussion, we consider a SWCNT with 2 nm of radius and electron mobility of $10^4 \text{ cm}^2\text{V}^{-1}\text{s}^{-1}$, which has been previously demonstrated in graphene samples [128, 129]. In Fig. 3.4a we show the light confinement, which is the ratio between the free-space wavelength $\lambda = 2\pi/k$ and the plasmon wavelength $\lambda_p = 2\pi/\text{Re}(k_p)$, of the fundamental plasmonic mode for frequencies below 200 meV. In this regime, we notice higher confinements for smaller values of the chemical potential, which leads to higher spontaneous emission enhancements due to the direct impact of confinement on the local density of states [10]. On the other hand, Fig. 3.4b shows the ratio between the real and imaginary components of the propagation wavevector, which is typically employed as the figure of merit (FOM) to characterize the relationship between a plasmon’s wavelength and its propagation length $d = 1/\text{Im}(k_p)$ in the SWCNT. Note that this FOM increases with the Fermi energy, corresponding to a

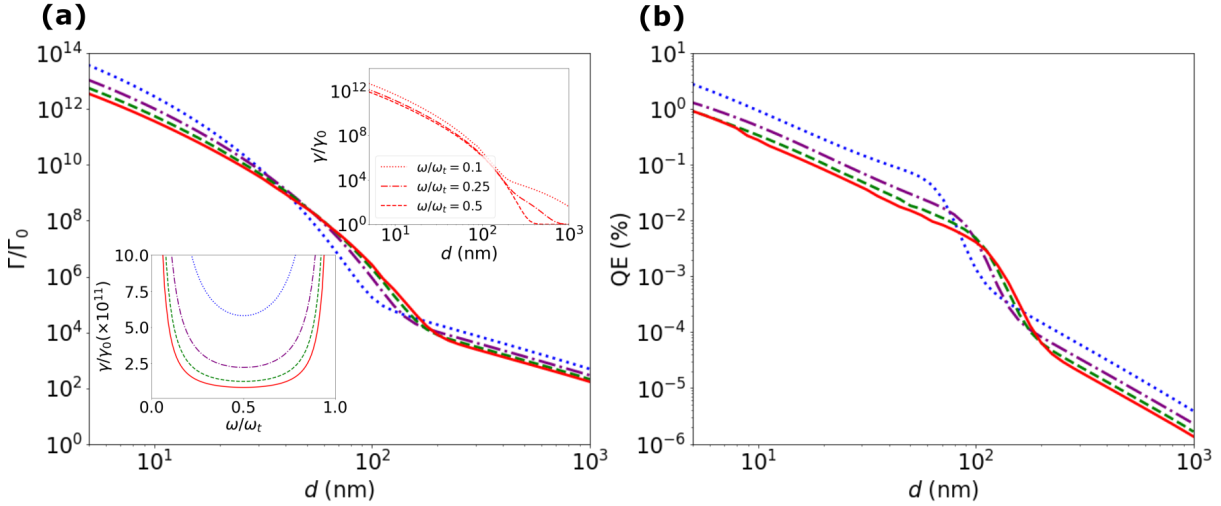


Figure 3.5: (a) Normalized two-plasmon SE rate for the $6s \rightarrow 5s$ transition in hydrogen ($\hbar\omega_t \approx 166$ meV) as a function of the distance between the emitter and the surface of the SWCNT. Upper right inset: Normalized two-plasmon SE spectral density as a function of distance for three frequencies of emission. In this inset, the Fermi energy is given by $E_F = 1$ eV. Lower left inset: Normalized two-plasmon SE spectral density at $d = 10$ nm. Since only the fundamental plasmonic mode is present, we observe a broadband spectrum of emission without any resonance. The divergences at $\omega = 0$ and $\omega = \omega_t$ are solely due to the normalization by the free-space spectral density, which goes to zero at the boundaries of the spectrum. (b) Quantum efficiency given by Eq. (3.8) of two-plasmon SE for the $6s \rightarrow 5s$ transition in hydrogen as a function of distance. In both plots, $E_F = \{0.25, 0.5, 0.75, 1\}$ eV (dotted blue, dash-dotted purple, dashed green, and solid red lines, respectively)

trade-off between light confinement and plasmon propagation in SWCNTs. Nevertheless, the fundamental plasmonic mode still offers strong confinements and long propagation lengths in this frequency regime.

In Fig. 3.5a we plot the two-plasmon SE rate normalized by the free-space two-photon decay rate as a function of the distance between the emitter and the nanotube surface. As an example, we consider the $6s \rightarrow 5s$ transition in hydrogen ($\hbar\omega_t \sim 166$ meV). We notice an extreme enhancement, $\sim 10^{12}$, of the two-plasmon SE rate in the near-field regime at $d = 10$ nm and higher at smaller distances. Hence, for a quantum emitter near a SWCNT, one expects to observe two-plasmon SE decay with a mean lifetime ~ 20 ns, which is smaller than for an emitter close to a graphene sheet. We also note

that the dependence of the emitter's two-plasmon emission rate on the distance to the SWCNT surface presents a noticeable change of behavior for $d \sim 100$ nm. This contrasts with the one-plasmon emission rate [105], which approximately follows an exponential decay with the distance [130] such as the case of extended graphene, as shown in Fig. 3.2b. This difference occurs because the two-plasmon SE rate involves an integral over a broad spectrum of frequencies below ω_t , and the exponential coefficient of $P(d, \omega)$ is not a constant. In the upper right inset we plot the spectral density as a function of distance for three frequencies of emission. We notice that γ goes to zero faster at frequencies close to $\omega_t/2$. Furthermore, exactly at $\omega_t/2$ there is no change of behavior in the far field since $\gamma(d, \omega_t/2) \sim P^2(d, \omega_t/2)$, which follows an exponential decay with the distance. The corresponding spectral lineshapes are shown in the lower left inset of Fig 3.5a. For any value of the Fermi energy, there exists a similar broadband spectrum where no particular frequency of emission is favoured. This is a consequence of the fact that the two-plasmon SE is only affected by the fundamental plasmonic mode of the SWCNT. In Fig. 3.5b we plot the quantum efficiency given by Eq. (3.8). We observe that when the emitter is placed in the vicinities of a SWCNT, the quantum efficiency can reach values of $\sim 1\%$ in the near-field ($d \lesssim 20$ nm), which is about the same order we found for an emitter close to an extended graphene monolayer. It is important to emphasize that this significant increase in the probability of second-order decay is achieved through the emission of plasmons, not photons, as in the case of an atom in free-space. However, since the one-dimensional geometry of a SWCNT limits the possible directions in which the plasmons are allowed to propagate, it may be possible to achieve higher conversion rates of the entangled plasmons into photons by scattering processes due to the presence of defects. Finally, we notice in the plot that the two-plasmon SE efficiency keeps above 0.01 % until $d \sim 100$ nm. This robustness of the efficiency of emission may be of practical interest in situations where one does not have precise control over the distance between the emitter and the nanotube.

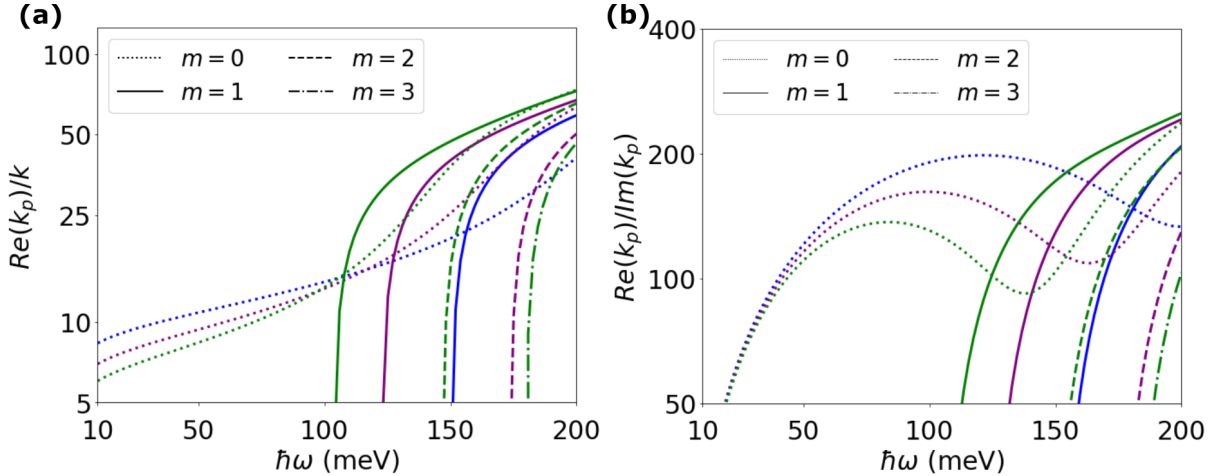


Figure 3.6: (a) Dispersion relation for all the plasmonic modes supported with free-space oscillating light of frequency $\hbar\omega < 200$ meV. Each color is associated with a GCW of a different radius, while the linestyle characterize the order of the mode. (b) The ratio between the real and imaginary parts of k_p for each plasmonic mode as a function of frequency. In both plots we choose silicon as the dielectric medium, which has permittivity $\varepsilon = 11.68$ in the frequency range considered. Also, $R = \{20, 30, 42\}$ nm (blue, purple, and green lines, respectively), and the Fermi energy is $E_F = 1$ eV.

3.2.3 Two-plasmon spontaneous emission in graphene coated wires

Now we investigate the case of an emitter close to a cylindrical waveguide coated with graphene, as shown in Fig. 3.3b. Unlike SWCNTs, graphene-coated wires are more stable and do not have strict constraints on their radius [130–132]. As a consequence, a multitude of entangled plasmonic modes can be excited in the two-plasmon SE process in the infrared region. In Fig. 3.6a we consider a silicon cylinder ($\varepsilon \simeq 11.68$) covered with graphene and plot the dispersion relation for all supported plasmonic modes with frequencies below 300 meV. For fixed radius, each $m \neq 0$ mode exists only above its minimum excitation frequency given by Eq. (3.21), while the fundamental mode, such as the case of a SWCNT, can be excited at any frequency. The number of modes present in the frequency range depends on the radius of the nanotube (and also on the Fermi energy and the inner dielectric medium), and some of them are degenerate at specific frequencies. This can be identified when two dispersion curves of the same color in the plot cross each

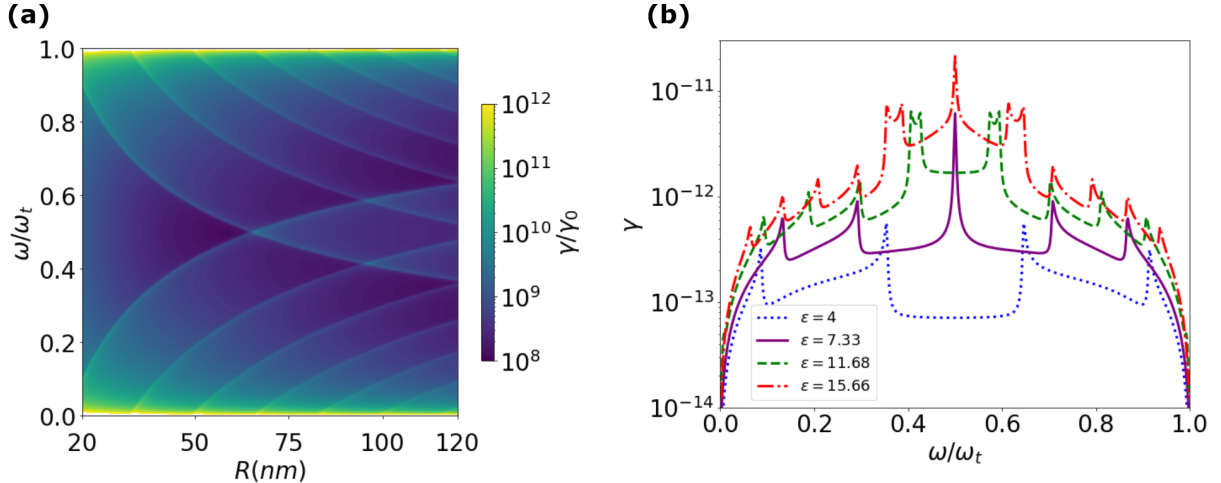


Figure 3.7: (a) Two-plasmon SE spectral density near a silicon ($\epsilon = 11.68$) nanowire covered with graphene as a function of the wire radius and the frequency of the plasmon normalized by the transition frequency. The transition frequency considered is $\hbar\omega_t \approx 166$ meV. (b) two-plasmon SE spectral density for various dielectric coated nanowires of radius $R = 100$ nm. For $\epsilon = 7.33$ ($\epsilon = 15.66$), the minimum excitation frequency of the mode $m = 1$ ($m = 2$) is precisely at $\omega_t/2$, which results in a huge resonance in the middle of the spectrum. In both plots the Fermi energy is $E_F = 1$ eV.

other, which can be seen, for instance, for the fundamental and first-order plasmonic modes. We also demonstrate strong light confinement for the non-fundamental plasmonic modes, which increases for higher values of the radius. The fundamental mode, however, presents slightly smaller confinement, which decreases (increases) with the radius for small (high) frequencies with the change of behavior occurring around ~ 150 nm. This same reasoning also explains the variations of $\text{Re}(k_p)/\text{Im}(k_p)$ versus frequency, as presented in Fig. 3.6b. We notice that no trade-off exists between light confinement and propagation length with respect to the radius. In contrast to the effect that increasing the chemical potential has on both quantities, larger wires present smaller FOMs and propagation lengths due to the propagation of plasmons around the wire.

In Fig. 3.7a we plot the normalized two-plasmon SE spectral density for a transition frequency of $\hbar\omega_t \sim 166$ meV as a function of the normalized frequency of emission (vertical axis) and the silicon GCW radius (horizontal axis). The most flashy aspect of the figure is the multitude of resonances present in the spectrum, which can be accounted by the high

degree of degeneracy of the plasmonic modes at their minimum excitation frequencies (as shown in Fig. 3.6a). Therefore, these resonance curves follow precisely the square root relation given by Eq (3.21). Due to the symmetric aspect of $\gamma(\omega)$, the resonances appear at $\omega_m^{(\min)}$ and at $\omega_t - \omega_m^{(\min)}$. Hence, cross-talks between modes of different orders exist when their minimum frequencies are complementary, i.e., when $\omega_m^{(\min)} + \omega_{m'}^{(\min)} = \omega_t$. In the particular case where $\omega_m^{(\min)} = \omega_t/2$, a stronger resonance takes place precisely in the middle of the spectrum, where both entangled plasmons are indistinguishable and emitted with the same frequency. In Fig. 3.7b we fix the radius at 100 nm and plot the spectral density for different dielectric materials. Since $\omega_m^{(\min)} \sim (1 + \varepsilon)^{-1/2}$, higher values of the relative permittivity also increase the number of plasmonic modes contributing to the spectral enhancement. One is able to tailor the dominant modes and frequencies of the emitted entangled plasmons. For $\varepsilon = 4$, only one plasmonic mode besides the fundamental is present on the two-plasmon SE spectrum, and $\varepsilon = 7.33$ and $\varepsilon = 15.66$ are chosen such that $\omega_1^{(\min)} = \omega_t/2$ and $\omega_2^{(\min)} = \omega_t/2$, respectively. In both latter cases, a stronger resonance takes place at half of the transition frequency in comparison to the resonances at other frequencies of emission. The curve of a GCW with $\varepsilon = 11.68$ is a vertical cut of Fig. 4a for $R = 100$ nm but without the normalization by γ_0 .

Despite the increase in γ as a function of the permittivity shown in Fig. 3.7b, the average spectral enhancement varies slowly with ε . As a consequence, the order of magnitude of the two-plasmon SE rate, which is the integral of $\gamma(\omega)$, is not substantially affected by changes of the inner dielectric medium for a wide range of values of ε . This allows one to tune the spectrum of emission without significantly affecting the desired high two-plasmon decay rate of the emitter. Indeed, this can be seen in Fig. 3.8a where we plot the two-plasmon SE rate for the hydrogen $6s \rightarrow 5s$ transition as a function of the relative permittivity. Lowering the Fermi energy, however, increases the plasmonic density of states in the whole spectrum of emission, which results in a higher two-plasmon SE rate. This can be seen by comparing the solid ($E_F = 0.5$ eV) with the dashed curve

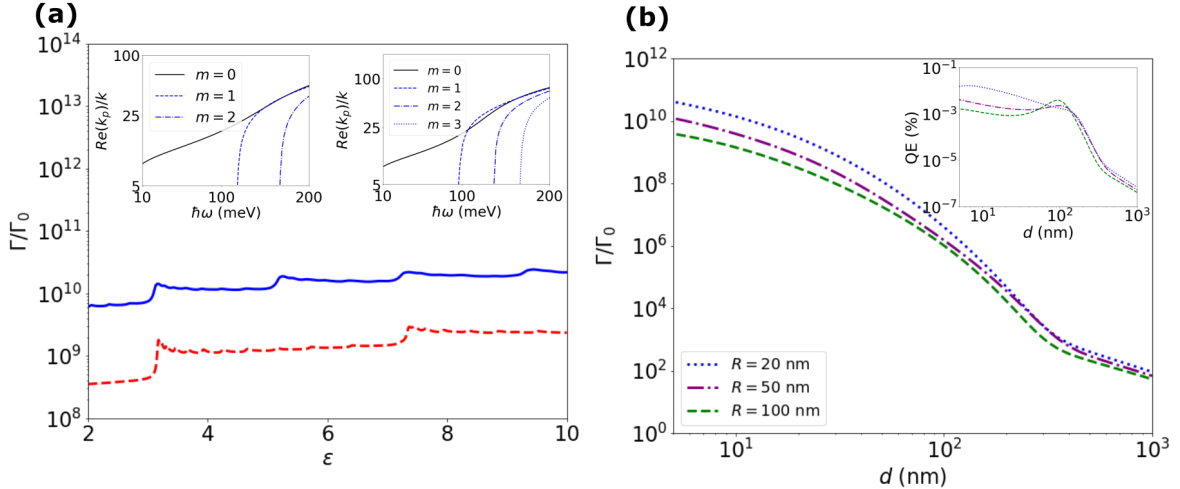


Figure 3.8: (a) Normalized two-plasmon SE rate for the $6s \rightarrow 5s$ transition in hydrogen as a function of the inner dielectric cylinder permittivity. We choose a nanowire of radius 25 nm and Fermi energies of 0.5 eV (blue solid curve) and 1 eV (red dashed curve). Inset: plasmon dispersion relations for $\varepsilon = 3.11$ (left) and $\varepsilon = 5.15$ (right). (b) Two-plasmon SE rate for the same hydrogen transition as a function of distance. The Fermi energy is equal to 1 eV. Inset: Quantum efficiency (Eq. (3.8)) as a function of distance for the same parameters of the main plot.

($E_F = 1$ eV). For some specific values of the permittivity, we notice resonances in the emission rate, a direct consequence of the degeneracy between the fundamental and first-order plasmonic modes. In the inset of Fig. 3.8a, we plot the plasmon dispersion relations for $\varepsilon \sim 3.11$ and $\varepsilon \sim 5.15$, which are the values for the first and second resonances for $E_F = 0.5$ eV. We notice that in contrast to Fig. 3.6a, where the modes are degenerate at two well-defined frequencies, for these values of ε the degeneracy occurs in a quasi-continuous range of frequencies. Fig. 3.8b shows the two-plasmon SE rate and quantum efficiency as a function of distances for different radii. We identify features similar to those in the emitter-SWCNT system analyzed in Fig. 3.5. In comparison to that case, we conclude that two-plasmon SE efficiency in GCW is more robust to distance variations than in the case of a SWCNT, with a small increase in magnitude right before starting to approach its free-space value. This can be explained by the fact that the one-plasmon SE rates in the denominator of Eq. (3.8) decay to their free-space values more rapidly than

the two-plasmon SE rate in the numerator.

3.3 Two-photon spontaneous emission in two-dimensional plasmonic nanostructures

Single photons - the most elementary states of light - can be generated on-demand in atomic and solid state emitters. However, achieving two-photon states in individual emitters is challenging because their generation rate is much smaller than competing one-photon processes. Typically, the two-photon spontaneous emission (TPSE) rate is eight to five orders of magnitude smaller than competing one-photon decay rates. On the other hand, spontaneous decay into two-plasmon polaritons in bulk metals [97], graphene monolayers [10] and nanowires [119] is predicted to be more than ten orders of magnitude larger than two-photon transitions, as discussed in the two previous sections. Polar dielectrics have also been proposed to enable two-phonon polariton emission faster than competing single-phonon processes [14]. However, these conventional surface wave polaritons yield a rather simple broadband emission spectrum and are intrinsically non-radiative since they do not propagate indefinitely due to absorption. Furthermore, out-coupling them into far-field radiation by, *e.g.*, defect engineering, while maintaining a high Purcell factor is challenging [95] and generally leads to inefficient photon production. For these reasons, we asked ourselves the following question: is there any material platform that significantly enhance not only the TQSE but also the radiative emission channels? The answer is that any system that supports a natural mechanism of scattering surface modes into the far field is suitable for enhancing radiative decay channels. For instance, one-photon emission near a metallic nanocube is significantly high due to plasmon scattering by the boundaries of the system [133]. Inspired by this example, we decided to study TQSE in atomically thin finite-sized plasmonic nanostructures [134], which is a material platform that presents extreme light confinement in the near field, and is amenable to analytical treatment by employing the plasmon wave function formalism [135]. In the next subsec-

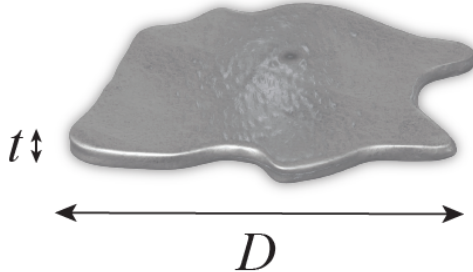


Figure 3.9: Schematics of an atomically thin plasmonic nanostructure of arbitrary shape, size $D \sim \sqrt{A}$, where A is its surface area, and thickness t .

tions we shall present a comprehensive description of these 2D plasmonic nanostructures using the plasmon wave function theory and then develop a methodology for calculating the Purcell factors and spectral lineshapes of a quantum emitter in the near-field. We end this section and chapter by applying this toolbox in two situations, namely, a quantum emitter close to a silver and a graphene nanodisk [134].

3.3.1 Plasmon wave function formalism

In this subsection we present the plasmon wave function (PWF) formalism [135, 136], which allows us to obtain the electric field and charge distribution induced on a ultra-thin metallic nanostructure (Fig. 3.9) due to an external field $\mathbf{E}^{ext}(\mathbf{r}, \omega)$. This approach assumes a large mismatch between the characteristic size (D) of the metallic nanostructures, typically in the range of a few tens of nanometers, and their resonant wavelengths (λ_α), in which case the optical response of the system can be described in the quasi-static approximation. In this limit, the parallel component of the electric field over the surface of the nanostructure satisfies

$$\mathbf{E}_{\parallel}(\mathbf{r}_{\parallel}, \omega) = \mathbf{E}_{\parallel}^{ext}(\mathbf{r}_{\parallel}, \omega) + \frac{i\sigma(\omega)}{4\pi\epsilon_0\omega} \nabla_{\mathbf{r}_{\parallel}} \int \frac{d^2\mathbf{r}'_{\parallel}}{|\mathbf{r}_{\parallel} - \mathbf{r}'_{\parallel}|} \nabla_{\mathbf{r}'_{\parallel}} \cdot [f(\mathbf{r}'_{\parallel}) \mathbf{E}_{\parallel}(\mathbf{r}'_{\parallel}, \omega)], \quad (3.22)$$

where we used the Coulomb law to write the induced field in terms of the charge distribution given by Eq. (3.9). Here, \mathbf{r}'_{\parallel} is the 2D in-plane position vector. It is convenient to re-write the above equation in terms of the dimensionless variable $\mathbf{u} = \mathbf{r}_{\parallel}/D$ and of

$\mathcal{E}(\mathbf{u}, \omega) = D\sqrt{f(D\mathbf{u})}\mathbf{E}_{\parallel}(D\mathbf{u}, \omega)$, namely

$$\mathcal{E}(\mathbf{u}, \omega) = \mathcal{E}^{ext}(\mathbf{u}, \omega) + \eta(\omega) \int d^2\mathbf{u}' \mathbb{M}(\mathbf{u}, \mathbf{u}') \cdot \mathcal{E}(\mathbf{u}', \omega), \quad (3.23)$$

where we defined

$$\eta(\omega) = \frac{i\sigma(\omega)}{4\pi\epsilon_0\omega D} \text{ and } \mathbb{M}(\mathbf{u}, \mathbf{u}') = -\sqrt{f(\mathbf{u})f(\mathbf{u}')} \nabla_{\mathbf{u}} \nabla_{\mathbf{u}'} \frac{1}{|\mathbf{u} - \mathbf{u}'|}. \quad (3.24)$$

$\mathbb{M}(\mathbf{u}, \mathbf{u}')$ is a real and symmetric operator which depends only on the geometry of the nanostructure. Therefore, \mathbb{M} admits a complete set of eigenmodes $\mathbf{V}_\alpha(\mathbf{u})$ and real eigenvalues $1/\eta_\alpha$ defined by the eigenvalue equation

$$\int d^2\mathbf{u}' \mathbb{M}(\mathbf{u}, \mathbf{u}') \cdot \mathbf{V}_\alpha(\mathbf{u}') = \frac{1}{\eta_\alpha} \mathbf{V}_\alpha(\mathbf{u}). \quad (3.25)$$

These eigenmodes are the solutions of Eq. (3.23) in the absence of an external electromagnetic field, and give the electric field profile over the surface of the nanostructure. They also satisfy the following closure and orthogonality relations, respectively

$$\sum_{\alpha} \mathbf{V}_\alpha^*(\mathbf{u}) \otimes \mathbf{V}_\alpha(\mathbf{u}') = \delta(\mathbf{u} - \mathbf{u}') \mathbb{I}_2 \text{ and } \int d^2\mathbf{u} \mathbf{V}_\alpha^*(\mathbf{u}) \cdot \mathbf{V}_{\alpha'}(\mathbf{u}) = \delta_{\alpha\alpha'}. \quad (3.26)$$

By expanding \mathcal{E} and \mathcal{E}^{ext} in terms of $\mathbf{V}_\alpha(\mathbf{u})$ and using Eq. (3.23) one obtains

$$\mathcal{E}(\mathbf{u}, \omega) = \sum_{\alpha} \frac{c_{\alpha}}{1 - \eta(\omega)/\eta_{\alpha}} \mathbf{V}_{\alpha}(\mathbf{u}), \quad (3.27)$$

where

$$c_{\alpha} = \int d^2\mathbf{u} \mathbf{V}_{\alpha}^*(\mathbf{u}) \cdot \mathcal{E}^{ext}(\mathbf{u}, \omega). \quad (3.28)$$

Eq. (3.27) establishes that for any external field \mathcal{E}^{ext} the electric field over the nanostructure is a superposition of the eigenmodes \mathbf{V}_α . Each eigenmode can be excited if the frequency of the external field matches one of the resonance frequencies of the system, given by $\text{Re}[\eta(\omega_{\alpha})] = \eta_{\alpha}$. The charge density distribution can be derived by inserting Eq. (3.27) into Eq. (3.9). Hence,

$$\rho_{2D}(\mathbf{u}, \omega) = \frac{4\pi\epsilon_0}{D} \sum_{\alpha} \frac{c_{\alpha}}{1/\eta_{\alpha} - 1/\eta(\omega)} v_{\alpha}(\mathbf{u}), \quad (3.29)$$

where we defined the plasmon wavefunction $v_\alpha(\mathbf{u}) = \nabla_{\mathbf{u}} \cdot [\sqrt{f(\mathbf{u})} \mathbf{V}_\alpha(\mathbf{u})]$, which corresponds to the normalized charge distribution of the plasmon mode α . By taking the divergence of $\sqrt{f(\mathbf{u})}$ times Eq. (3.25) one can show that the plasmon wave functions satisfy the Poisson equation:

$$\nabla_{\mathbf{u}}^2 \int d^2 \mathbf{u}' \frac{v_\alpha(\mathbf{u}')}{|\mathbf{u} - \mathbf{u}'|} = \eta_\alpha^{-1} v_\alpha(\mathbf{u}). \quad (3.30)$$

Also, it follows from the previous equation that \mathbf{V}_α can be written in terms of the corresponding PWF as

$$\mathbf{V}_\alpha(\mathbf{u}) = \sqrt{f(\mathbf{u})} \eta_\alpha \int d^2 \mathbf{u}' \frac{v_\alpha(\mathbf{u}')(\mathbf{u} - \mathbf{u}')}{|\mathbf{u} - \mathbf{u}'|^3}, \quad (3.31)$$

and by taking into consideration the orthogonality condition for the eigenmodes, given in Eq. (3.26), one can then show that the PWFs must obey the following relation:

$$\int d^2 \mathbf{u} \int d^2 \mathbf{u}' \frac{v_\alpha(\mathbf{u}) v_{\alpha'}(\mathbf{u}')}{|\mathbf{u} - \mathbf{u}'|} = -\frac{\delta_{\alpha\alpha'}}{\eta_\alpha}. \quad (3.32)$$

Let's discuss a particular geometry amenable to analytical treatment, namely a plasmonic nanodisk [108]. In this case the various eigenmodes and eigenvalues supported by the nanodisk have a closed form [137, 138], and we derive them in appendix A. We consider a bilayer Ag(111) nanodisk described by a Drude model conductivity, namely

$$\sigma(\omega) = \frac{i\epsilon_0\omega_p^2 t}{\omega + i/\tau}, \quad (3.33)$$

where $\hbar\omega_p = 2\pi\hbar c/\lambda_p = 9.1$ eV and $\hbar\tau^{-1} = 18$ meV are the plasma frequency and relaxation rate of bulk Ag, and $t \approx 0.47$ nm is the thickness of the nanostructure [106, 107]. By inserting the Drude conductivity in Eq. (3.24) and solving $\text{Re}[\eta(\omega_\alpha)] = \eta_\alpha$ we find analytical expressions for the resonance frequencies of the nanostructures,

$$\omega_\alpha = \sqrt{\frac{-\omega_p^2 t}{4\pi D \eta_\alpha}}, \quad (3.34)$$

We notice that these resonance frequencies are well defined, i.e., plasmons do not exist in a continuum. This is a consequence of the finite-size of the system, which implies the existence of localized surface plasmons (LSPs) instead of propagative SPPs.

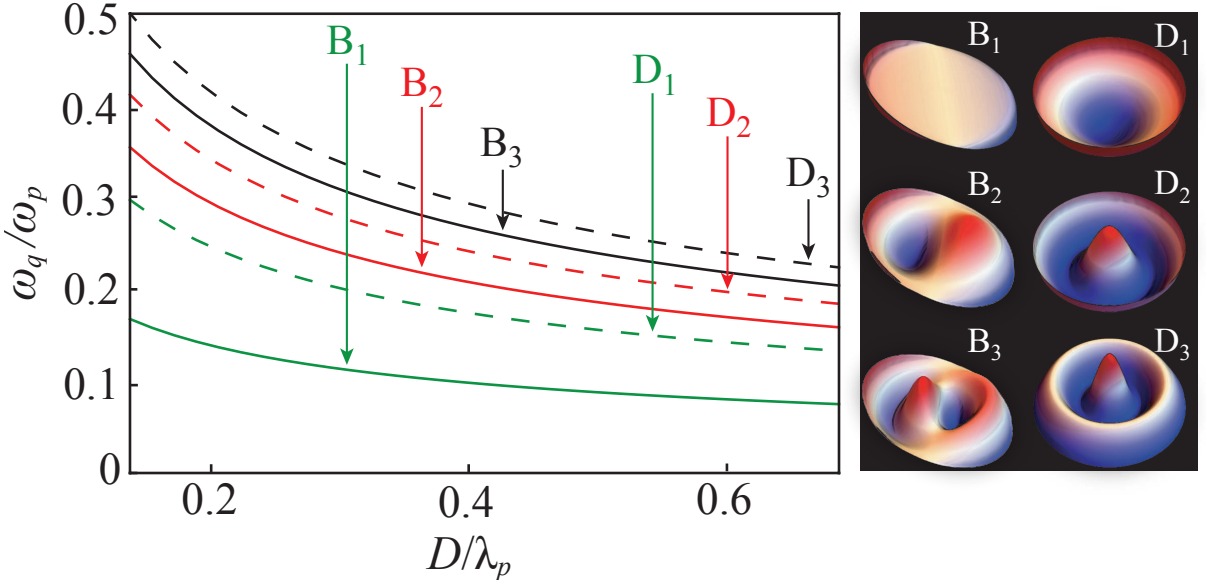


Figure 3.10: Resonant frequencies ω_q for the three lowest energy bright (B_q) and dark (D_q) modes versus the diameter D of a bilayer Ag(111) nano-disk. The corresponding spatial charge distributions at a given time are shown on the right panel. In this panel, the charge density is higher in the red regions and smaller in the blue regions.

Fig. 3.10 depicts the resonant frequencies of the six lowest energy azimuthally symmetric dark (D_q) and dipolar bright (B_q) field modes versus the diameter of a Ag nanodisk. Due to their different angular profiles, the dark modes do not radiate while the bright ones are able to leak into the far-field by emitting dipolar radiation [139]. As we shall discuss later, this feature will be useful for generating far-field photons through plasmon-emitter coupling in the near-field. Since the plasmon excitation frequencies goes with $\sim D^{-1/2}$, we highlight the controlled optical response we can achieve in these nanostructures by properly choosing their sizes. The associated spatial charge distributions are also presented. We observe that higher resonance frequencies are correlated with more oscillations in the radial and angular profile of the PWF. Finally, we notice that these LSPs exist in the near-infrared to the optical domain since $\lambda_p \sim 270$ nm, in contrast to plasmons in graphene that live only in the mid-infrared region.

3.3.2 Purcell factors and spectral lineshapes

We now turn our attention to the TQSE phenomenon and consider a quantum emitter close to an atomically thin plasmonic nanostructure. In the most general situation, we cannot use Eq. (2.32) since the system lacks the geometrical symmetries required to diagonalize the imaginary part of the Green's tensor. In these cases, we must take a step back and use Eq. (2.27) instead. However, in some particular configurations there are enough symmetries so that we are allowed use Eq. (2.32), as, for instance, the case of an on-axis quantum emitter close to a plasmonic nanodisk. Moreover, even in more complicated scenarios we expect similar numerical results between both equations since the Purcell factors give the contribution of the diagonal terms of the Green's tensor. Hence, all qualitative conclusions found with Eq. (2.32) will not be different from (2.27). For these reasons, and also for simplicity, in all subsequent discussion we will restrict ourselves to the scope of Eq. (2.32).

The Purcell factors $P_a(\mathbf{r}, \omega)$ can be calculated with the aid of the identity [62] $P_a(\mathbf{r}, \omega) = W_a(\mathbf{r}, \omega)/W_0(\omega)$, where $W_a(\mathbf{r}, \omega)$ is the total power dissipated by a classical dipole $\mathbf{d}_a = d_a \hat{\mathbf{e}}_a$ oscillating with frequency ω at position \mathbf{r} near the nanostructure, and $W_0(\omega)$ is the corresponding dissipated power in free space. This identity derives from Eq. (1.25) since it can be shown that its right-hand side is equal to $W_a(\mathbf{r}, \omega)/W_0(\omega)$ [37]. As a consequence, one can write [62]

$$P_a(\mathbf{r}, \omega) = P_{a,nr}(\mathbf{r}, \omega) + P_{a,r}(\mathbf{r}, \omega), \quad (3.35)$$

where

$$\begin{aligned} P_{a,nr}(\mathbf{r}, \omega) &= \frac{6\pi\epsilon_0 c^3}{\omega^4 |\mathbf{d}_a|^2} \int d^3\mathbf{r}' \text{Re}\{\mathbf{J}^*(\mathbf{r}', \omega) \cdot \mathbf{E}(\mathbf{r}', \omega)\}, \\ P_{a,r}(\mathbf{r}, \omega) &= \frac{6\pi\epsilon_0 c^3}{\omega^4 |\mathbf{d}_a|^2} \int_{r' \rightarrow \infty} d\mathbf{A}' \cdot \text{Re}\{\mathbf{E}(\mathbf{r}', \omega) \times \mathbf{H}^*(\mathbf{r}', \omega)\} \end{aligned} \quad (3.36)$$

correspond to the contribution of non-radiative and radiative decay channels to the Purcell factor, respectively. Due to the finite size of the nanostructure, we expect a non-negligible contribution of $P_{a,r}$, in contrast to the cases presented previously in this thesis.

We start by calculating the non-radiative contribution. By inserting $\mathbf{J}(\mathbf{r}', \omega) = \mathbf{K}(\mathbf{r}', \omega)\delta(z') = \sigma(\omega)f(\mathbf{r}')\mathbf{E}_{\parallel}(\mathbf{r}', \omega)\delta(z')$ into equation (3.36) and using the orthogonality relation in Eq. (3.26), we derive

$$P_{a,nr}(\mathbf{r}, \omega) = \frac{6\pi\epsilon_0 c^3}{\omega^4 |\mathbf{d}_a|^2} \text{Re}[\sigma(\omega)] \sum_{\alpha} \left| \frac{c_{\alpha}}{1 - \eta(\omega)/\eta_{\alpha}} \right|^2. \quad (3.37)$$

In the near-field regime and using the quasi-static approximation, the external field over the nanostructure, which here is the electric field generated by the oscillating dipole \mathbf{d}_a placed at position \mathbf{r} , is given by $\mathbf{E}^{ext}(\mathbf{r}', \omega) = \frac{1}{4\pi\epsilon_0} \nabla \mathbf{d}_a \cdot \nabla |\mathbf{r} - \mathbf{r}'|^{-1}$. After inserting this expression into Eq. (3.28), we obtain $c_{\alpha} = \mathbf{d}_a \cdot \mathbf{F}_{\alpha}^*(\mathbf{r})/4\pi\epsilon_0 D^2$, where

$$\mathbf{F}_{\alpha}(\mathbf{r}) = \int d^2 \mathbf{u}' \frac{v_{\alpha}(\mathbf{u}')(\mathbf{r}/D - \mathbf{u}')}{|\mathbf{r}/D - \mathbf{u}'|^3} \quad (3.38)$$

corresponds to the field generated at position \mathbf{r} by the α -th PWF mode. This result allows us to write Eq. (3.37) as

$$P_{a,nr}(\mathbf{r}, \omega) = \frac{3c^3}{2D^3\omega^3} \text{Im} \sum_{\alpha} \hat{\mathbf{e}}_a \cdot \frac{\mathbf{F}_{\alpha}(\mathbf{r}) \otimes \mathbf{F}_{\alpha}^*(\mathbf{r})}{1/\eta(\omega) - 1/\eta_{\alpha}} \cdot \hat{\mathbf{e}}_a. \quad (3.39)$$

In the regime $D \ll \lambda_{\alpha}$, the radiative contribution to the Purcell factor is due to the system's emitted dipolar radiation, which can be well approximated by [140]

$$P_{a,r}(\mathbf{r}, \omega) \simeq \frac{|\mathbf{d}_a + \mathbf{d}_{a,ind}(\mathbf{r}, \omega)|^2}{|\mathbf{d}_a|^2}, \quad (3.40)$$

where

$$\mathbf{d}_{a,ind}(\mathbf{r}, \omega) = \int d^2 \mathbf{r}' \mathbf{r}' \rho_{2D}(\mathbf{r}', \omega) = \sum_{\alpha} \frac{\zeta_{\alpha} \otimes \mathbf{F}_{\alpha}^*(\mathbf{r})}{1/\eta(\omega) - 1/\eta_{\alpha}} \cdot \mathbf{d}_a \quad (3.41)$$

is the dipole moment induced in the nanostructure by the field of the dipole \mathbf{d}_a , and

$$\zeta_{\alpha} = \int d^2 \mathbf{u} \mathbf{u} v_{\alpha}(\mathbf{u}) \quad (3.42)$$

corresponds to the dipole moment of the plasmon α . Hence,

$$P_{a,r}(\mathbf{r}, \omega) = \left| \hat{\mathbf{e}}_a + \sum_{\alpha} \frac{\zeta_{\alpha} \otimes \mathbf{F}_{\alpha}^*(\mathbf{r})}{1/\eta(\omega) - 1/\eta_{\alpha}} \cdot \hat{\mathbf{e}}_a \right|^2. \quad (3.43)$$

This approximated expression of the radiative Purcell factor consists basically of substituting the emitter-nanostructure system by an oscillating point electric dipole given by the sum of the emitter's dipole with the nanostructure induced dipole. The induced dipole is written as a sum over the dipole moments of each PWF weighted by their coefficients in the eigenmodes expansion. Therefore, it is natural to expect that a good generalization of this equation can be obtained by considering also the electromagnetic radiation of other multipole moments in the summation. Finally, it is important to note that Eqs. (3.39) and (3.43) are exact (within the quasi-static approximation for obtaining the PWFs and the replacement of the nanostructure by a point dipole when calculating the radiative Purcell factor) expressions for the non-radiative and radiative Purcell factors, and can be numerically evaluated for any material once the PWFs for a given geometry are known.

The TQSE spectral density of a $s \rightarrow s$ transition is given by Eq. (2.24). By taking advantage of Eq. (3.35), we can identify the spectral enhancements associated to the three relevant plasmon-plasmon, photon-plasmon, and photon-photon relaxation channels, namely

$$\frac{\gamma_{pl,pl}(\mathbf{r}, \omega)}{\gamma_0(\omega)} = \frac{1}{3} \sum_a P_{a,nr}(\mathbf{r}, \omega) P_{a,nr}(\mathbf{r}, \omega_t - \omega), \quad (3.44)$$

$$\frac{\gamma_{ph,pl}(\mathbf{r}, \omega)}{\gamma_0(\omega)} = \frac{1}{3} \sum_a [P_{a,nr}(\mathbf{r}, \omega) P_{a,r}(\mathbf{r}, \omega_t - \omega) + P_{a,r}(\mathbf{r}, \omega) P_{a,nr}(\mathbf{r}, \omega_t - \omega)], \quad (3.45)$$

$$\frac{\gamma_{ph,ph}(\mathbf{r}, \omega)}{\gamma_0(\omega)} = \frac{1}{3} \sum_a P_{a,r}(\mathbf{r}, \omega) P_{a,r}(\mathbf{r}, \omega_t - \omega). \quad (3.46)$$

In Fig. 3.11 we depict these unique two-quanta decay channels. We point that, in principle, $P_{a,nr}$ also accounts for non-radiative mechanisms which could result in, e.g., entangled lossy excitations (double quenching) [10]. However, in low-dissipative systems such as the ones we consider here, plasmonic modes largely dominate the non-radiative emission channel and double quenching is negligible. The photon-photon decay channel results from the product of $P_{a,r}$ with itself, and is also enhanced as a result of plasmon leakage into the far-field. Last, but not least, we have a hybrid entangled photon-plasmon

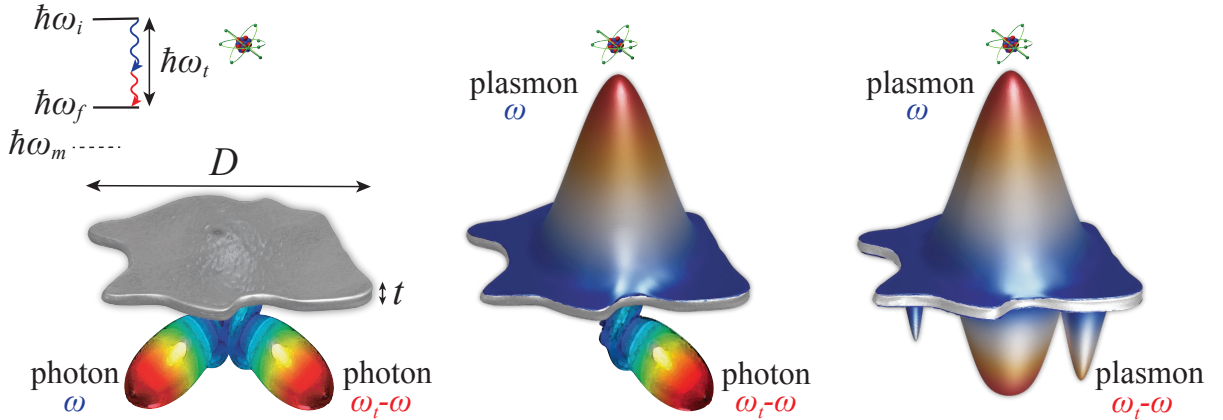


Figure 3.11: Schematics of the system under study and representation of the TQSE pathways for a multi-level quantum emitter close to a 2D plasmonic nanostructure: a pair of photons is emitted to the far-field (left), a hybrid photon-plasmon state is generated (center), or two plasmonic excitations are launched on the nanostructure (right). In each case the two-quanta states can be entangled in time-energy, linear, or angular momentum.

state as a result of the cross products between $P_{a,nr}$ and $P_{a,r}$.

The TQSE channels inherit their main spectral characteristics directly from $P_{a,r}$ and $P_{a,nr}$. In order to investigate the line-shape of these spectral enhancements, we consider that the conductivity of the nanostructure is well described by a Drude model given by Eq. (3.33). Using this expression in Eq. (3.39) we find that the non-radiative Purcell factor can be written as

$$P_{a,nr}(\mathbf{r}, \omega) = \sum_{q=1}^N \frac{3c^3\omega_p^2 t}{8\pi D^4\omega^2\tau} \frac{\sum_{j=1}^{g_q} |\hat{\mathbf{e}}_a \cdot \mathbf{F}_{q,j}(\mathbf{r})|^2}{(\omega^2 - \omega_q^2)^2 + \omega^2/\tau^2}, \quad (3.47)$$

where ω_q is given by Eq. (3.34) with $\omega_p^2 t \rightarrow e^2 E_F / \pi \epsilon_0 \hbar^2$ in the case of a graphene nanostructure (see the graphene Drude conductivity in Eq. (3.4)). We have also split the summation over modes α into a sum in q over all the N resonances present in the TQSE spectrum, and a sum in j over all degenerate modes. In Eq. (3.47) g_q is the degree of degeneracy of the q -th resonance.

In the regime of small dissipation, the overlap between different resonances is negligible, and we can expand each term in the above sum around the corresponding ω_q , leading

to

$$P_{a,nr}(\mathbf{r}, \omega) \simeq \sum_{q=1}^N \frac{A_{a,q}}{\omega^2} \frac{(1/2\tau)^2}{(\omega - \omega_q)^2 + (1/2\tau)^2}, \quad (3.48)$$

where

$$A_{a,q} = \frac{3c^3\omega_p^2 t \tau}{8\pi D^4 \omega_q^2} \sum_{j=1}^{g_q} |\hat{\mathbf{e}}_a \cdot \mathbf{F}_{q,j}(\mathbf{r})|^2. \quad (3.49)$$

We kept the prefactor $1/\omega^2$ since it comes from the normalization by the free space spectral density and determines the spectrum behaviour near $\omega = 0$ and $\omega = \omega_t$. It should be noticed, however, that far from $\omega = 0$ (and $\omega = \omega_t$) it is a good approximation to replace $1/\omega^2$ by $1/\omega_q^2$. Note that any eigenmode supported by the system provides a Lorentzian line-shape for the non-radiative part of the spectrum regardless of the geometry of the nanostructure. Hence, the two-plasmon SE spectrum is a combination of Lorentzian line-shapes symmetric around each of the N distinct plasmonic resonances ω_q within the TQSE spectral range. Also, precisely at a given plasmon resonance $\omega_{q'}$, the non-radiative Purcell factor reduces to $P_{a,nr}(\mathbf{r}, \omega_{q'}) = (6\pi c^3 \eta_{q'}^2 \tau / D^2 \omega_p^2 t) \sum_{j=1}^{g_q} |\hat{\mathbf{e}}_a \cdot \mathbf{F}_{q',j}(\mathbf{r})|^2$. The particular case of graphene can be obtained by replacing $\omega_p^2 t \rightarrow e^2 E_F / \pi \epsilon_0 \hbar^2$ and $\tau \rightarrow E_F \mu / ev_F^2$. This gives a non-radiative contribution at resonance proportional to μ/D^2 , being independent of E_F .

Now we will do the same analysis for the radiative contribution given by Eq. (3.43). To write $P_{a,r}$ as a sum over resonances is more subtle than the previous case since $\lim_{\omega \rightarrow \infty} P_{a,r} \rightarrow 1$, which means that there is always an overlap between different resonances due to the free space contribution. Therefore, in order to write $P_{a,r}$ as a sum of functions which accurately describe each resonance near its own resonance frequency, we must subtract the background contribution from all other $N - 1$ resonant terms. Hence,

$$P_{a,r}(\mathbf{r}, \omega) \simeq \sum_{q=1}^N \left| \hat{\mathbf{e}}_a + \frac{\omega_p^2 t}{4\pi D} \frac{\sum_{j=1}^{g_q} \hat{\mathbf{e}}_a \cdot \mathbf{F}_{q,j}^*(\mathbf{r}) \otimes \zeta_{q,j}}{\omega^2 - \omega_q^2 + i\omega/\tau} \right|^2 - (N - 1). \quad (3.50)$$

Expanding the denominator of each resonant term around its corresponding ω_q yields

$$P_{a,r}(\mathbf{r}, \omega) = \sum_{q=1}^N \frac{\left| (\omega - \omega_q + i/2\tau)\hat{\mathbf{e}}_a + \frac{\omega_p^2 t}{8\pi D\omega_q} \sum_{j=1}^{g_q} \hat{\mathbf{e}}_a \cdot \mathbf{F}_{q,j}^*(\mathbf{r}) \zeta_{q,j} \right|^2}{(\omega - \omega_q)^2 + (1/2\tau)^2} - (N-1). \quad (3.51)$$

Finally, we express $\zeta_{q,j}$ in terms of its components parallel and perpendicular to the dipole moment, $\zeta_{q,j} = \zeta_{a;q,j}^{\parallel} + \zeta_{a;q,j}^{\perp}$, where $\zeta_{a;q,j}^{\parallel} = (\zeta_{q,j} \cdot \hat{\mathbf{e}}_a) \hat{\mathbf{e}}_a$ and $\zeta_{a;q,j}^{\perp} = \zeta_{q,j} - (\zeta_{q,j} \cdot \hat{\mathbf{e}}_a) \hat{\mathbf{e}}_a$.

This results in

$$P_{a,r}(\mathbf{r}, \omega) = 1 + \sum_{q=1}^N \frac{(\omega - \omega_q + f_{a,q}/2\tau)^2 + B_{a,q} \times (1/2\tau)^2}{(\omega - \omega_q)^2 + (1/2\tau)^2} - N, \quad (3.52)$$

where

$$f_{a,q} = \frac{\omega_p^2 \tau t}{4\pi D\omega_q} \sum_{j=1}^{g_q} \text{Re} \left[\hat{\mathbf{e}}_a \cdot \mathbf{F}_{q,j}^*(\mathbf{r}) \zeta_{a;q,j}^{\parallel} \right] \quad (3.53)$$

is the Fano asymmetry parameter of the q -th radiative Fano resonance [141–143], and

$$B_{a,q} = \left[1 + \frac{\omega_p^2 t}{8\pi D\omega_q} \sum_{j=1}^{g_q} \text{Im} \left[\hat{\mathbf{e}}_a \cdot \mathbf{F}_{q,j}^*(\mathbf{r}) \zeta_{a;q,j}^{\parallel} \right] \right]^2 + \left| \frac{\omega_p^2 t}{8\pi D\omega_q} \sum_{j=1}^{g_q} \hat{\mathbf{e}}_a \cdot \mathbf{F}_{q,j}^*(\mathbf{r}) \zeta_{a;q,j}^{\perp} \right|^2 \quad (3.54)$$

is the amplitude of the Lorentzian resonance. Hence, the two-photon SE spectrum is a combination of asymmetric Fano and symmetric Lorentzian line-shapes around each of the N distinct plasmonic resonances ω_q within the TPSE spectral range. The radiative Purcell factor peaks approximately at $\omega_q + (2\tau f_{a,q})^{-1}$ around which the Fano term overwhelms the Lorentzian one, but near the Fano dip at $\omega_q - f_{a,q}/2\tau$ the Lorentzian term becomes relevant preventing complete inhibition of photon emission. By tailoring $f_{a,q}$ through geometry or material properties it is possible to either enhance or suppress the generation of far-field radiation via $\gamma_{ph,ph}$ or $\gamma_{ph,pl}$.

We can interpret the above results for the TQSE radiative and non-radiative spectrum as follows: when the electromagnetic fields radiated by the quantum emitter and by the induced multipoles on the nanostructure are in (out of) phase, far-field constructive (destructive) interference occurs, rendering an asymmetric Fano-like profile for $P_{a,r}$. On the other hand, non-radiative processes are governed by absorption in the nanostructure

through plasmon excitation, where the induced fields are much stronger than the emitter's. Hence, emitter-multipoles interferences are negligible and $P_{a,nr}$ results symmetric around resonances. We finish this subsection recalling the reader that by using Eqs. (3.48) and (3.52) in Eqs (3.44)-(3.46) we are able to fully describe the line-shape of the spectral enhancements for each decay channel in the TQSE process. By integrating each contribution, we can also compare the relevance of each decay channel to the total TQSE rate, which is obtained by summing over the three pathways. In the next subsections we will apply this formalism to the case of a quantum emitter close to a Ag and a graphene nanodisk.

3.3.3 Two-photon spontaneous emission near a two-dimensional silver nanodisk

In this subsection we consider an on-axis quantum emitter close to a silver nanodisk described in Fig. 3.10. As shown in appendix A, in this case only dark and bright modes can be excited. The former ones do not contribute to $P_{a,r}$, while the latter have non-zero induced dipole moments that enable the photon-photon and photon-plasmon decay channels. The full normalized TQSE spectrum $\gamma/\gamma_0 = (\gamma_{pl,pl} + \gamma_{ph,pl} + \gamma_{ph,ph})/\gamma_0$ of the metallic nanodisk is shown in Fig. 3.12a, and exhibits a wealth of strongly localized peaks precisely along the curves for $\omega_q(D)$ and $\omega_t - \omega_q(D)$. Single, dual, and even multi-band quanta emissions are possible depending on the number of resonances below ω_t . Cross-talk between bright-bright or dark-dark modes at complementary frequencies $\omega_q(D) = \omega_t - \omega_{q'}(D)$ also produces extreme enhancements of the TQSE spectrum $\gamma(\omega)/\gamma_0(\omega) \sim 10^8$. These features are very similar to the case of an emitter close to a graphene coated dielectric wire presented in section 3.2.3. However, we emphasize that GCW SPPs exist in a continuous range of frequencies, in contrast to the well-defined frequencies of these LSPs. Therefore, the nature of the resonances supported in the two cases are different. Precisely at the resonance frequencies, the relative magnitude of the spectral enhancement

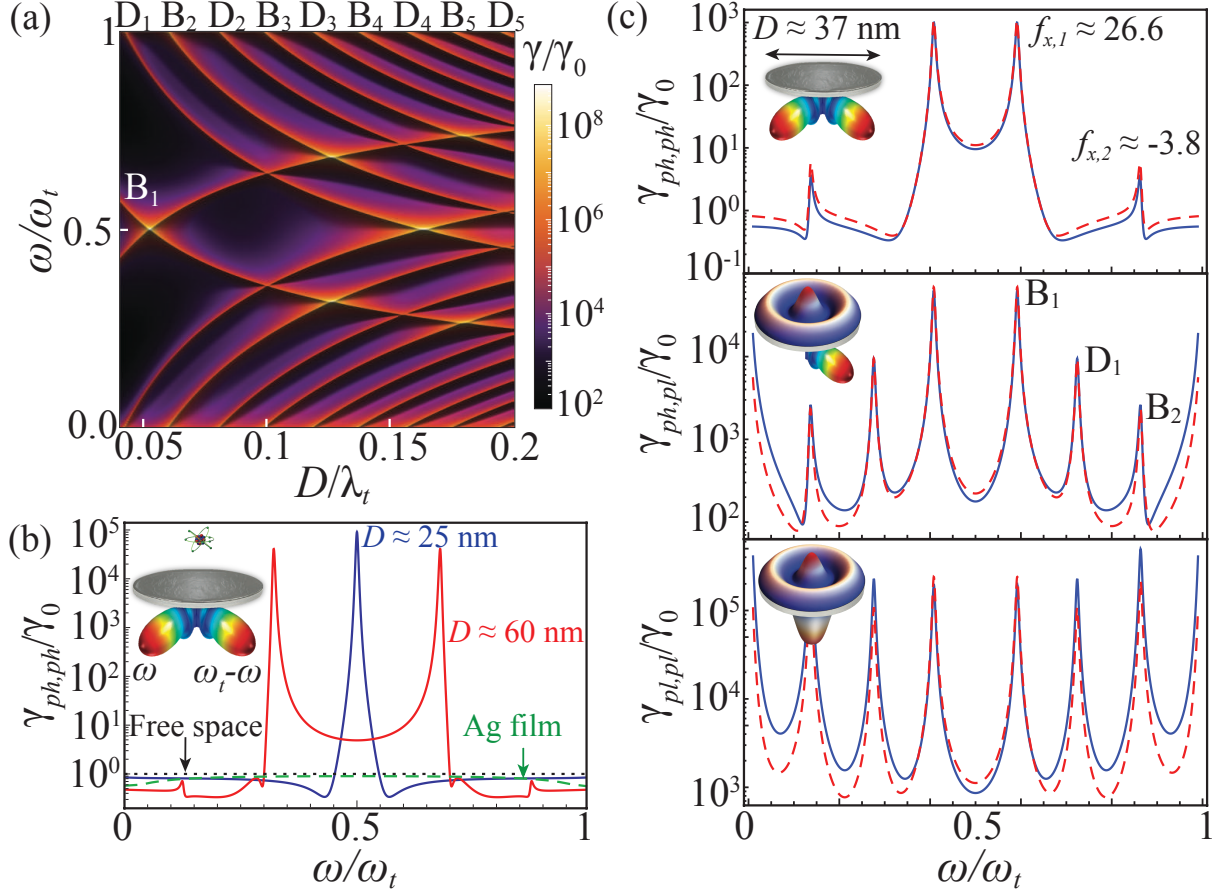


Figure 3.12: (a) TQSE spectral density $\gamma(\omega)$ near a bilayer Ag nanodisk. The chosen emitter is a quantum dot with transition frequency $\hbar\omega_t = 2.64$ eV placed at $z = 10$ nm. (b) Photon-pair production rates for a Ag nano-disk (solid blue and red), a Ag film (green), and in free space (black). (c) TQSE spectral profiles for photon-photon (top), photon-plasmon (center), and plasmon-plasmon (bottom) decay channels. Solid (dashed) curves result from exact (approximated) calculations (see discussion in the text). The Fano asymmetry factor $f_{x,q}$ is displayed for the two bright resonances.

of an emitter near a GCW is much smaller than if it is placed close to a finite-sized nanostructure. However, the opposite relation holds in the spectral regions between the resonance frequencies since GCW plasmons couple to the emitter at any frequency of emission.

Figure 3.12b compares $\gamma_{ph,ph}$ between confined and extended 2D metallic systems, evidencing that the finite size of the nanostructure is critical to accomplishing giant entangled photon-photon production rates. As previously mentioned, extended plasmonic

films do not enhance the radiative two-quanta decay channel since there is no natural mechanism of out-coupling the SPPs into photons. We notice that the highest spectral enhancement occurs for $D \approx 25$ nm, which corresponds to the case where the fundamental bright mode resonance frequency is exactly at the middle of the spectrum. The red curve presents the second highest TPSE spectral enhancement since it corresponds to the crossing between B_1 and B_2 . The spectral profiles of the TQSE channels are reported in Fig. 3.12c, where we observe a very good agreement between the TQSE lineshapes derived from the approximated expressions in Eqs. (3.48) and (3.52) and those obtained with full numerical evaluations. Close to plasmonic resonances there is a clear interplay of Fano and Lorentzian lineshapes that results in notable differences between the spectral profiles of $\gamma_{ph,ph}$ and those of the other emission mechanisms. The spectral distinction of $\gamma_{ph,pl}$ and $\gamma_{pl,pl}$ is more subtle: it is more prominent near the borders of the spectrum, and $f_{a,q}$ can be engineered to enhance their differences around $\omega_t/2$.

We emphasize that the results presented here are within reach of experimental observation. Setups such as those of Refs. [79, 144] can be employed to measure the TPSE at near-infrared frequencies from quantum dots with biexciton-exciton transitions. Recently developed synthesis techniques [106, 107] can be employed to fabricate ultra-thin noble-metal nanostructures on a SiO₂-GaAs membrane with an embedded emitter layer. For an InGaAs quantum dot located on-axis near a Ag nanodisk ($t = 1.65$ nm, $D = 62$ nm, SiO₂ thickness = 30 nm), for example, the fundamental bright mode is excited at $\omega_{B_1} = \omega_t/2 \simeq 1.4$ eV, resulting in two-photon enhancements $\gtrsim 10^4$. Such a giant enhancement is well above existing experimental sensitivities and should be easily detected (much smaller values ~ 10 have already been measured in Ref. [144]). High-resolution (~ 1 μeV) spectrometers can be used to scan the far-field TPSE spectral density and probe some of the predicted Fano and Lorentzian features. For instance, the Fano asymmetry factor can be obtained by reconstructing the two-photon spectrum via hyperspectral photon-coincidence measurements [13, 144] using near-infrared monochromators and

photo-detectors. Lorentzian signatures present in the hybrid photon-plasmon channel can be probed via frequency-resolved photoluminescence detection. Finally, these experiments combined with time-resolved fluorescence measurements [95, 145] of the emitter’s dynamics allow to extract the full TPSE rate Γ in Eq (2.32) and the individual decay probabilities for the three emission channels.

In summary, we have shown that atomically thin finite-sized noble metals are an ideal material platform to harness two-photon emission processes from single emitters, enabling emission rates significantly faster than in monolayers and thin films. However, the attentive reader will notice that the spectral enhancements found in this system is significantly smaller than the ones reported for graphene monolayers (Fig. 3.1), SWCNTs (Fig. 3.5a) and GCWs (Fig. 3.8a). Indeed, noble metals are extremely good in lifting the radiative decay channel, but do not present a plasmon-emitter coupling as strong as graphene. Still, the spectral enhancements found when reducing the dimensionality of these materials are far beyond what can be achieved in standard metallic systems [80, 99]. In the next final subsection we will consider a graphene nanodisk and show how we can achieve efficient TQSE enhancements while keeping the generation of far-field photons in the system high.

3.3.4 Two-photon spontaneous emission near a two-dimensional graphene nanodisk

In order to accomplish tunable TPSE rates we consider the nanodisk composed of active materials whose optical response can be dynamically controlled, e.g., graphene. Graphene not only provides the opportunity of emitting two-quanta in the mid-IR, but also allows for easier fabrication of 2D nanostructures as compared to metallic systems. Fig. 3.13a reports $\gamma(\omega)$ for different Fermi energies of a graphene nanodisk, showing enhanced selective spectral emission (solid curves). This is in stark contrast with the typical broadband spectrum achieved in monolayers (dashed curves). Giant photon-pair

production in this system is also possible, with $\gamma_{ph,ph}^{\text{disk}}/\gamma_{ph,ph}^{\text{monolayer}} \gtrsim 10^9$ at the center of the spectrum (not shown). Nevertheless, in graphene nanostructures this is achieved with even higher TQSE enhancements in comparison to noble metals, which allows for the disruption of the unbalance between one- and two-quanta transitions.

In Fig. 3.13b we address the question whether photon generation can be more efficient through two-photon transitions than via existing ordinary one-photon emission channels. The ratio between the probabilities of emitting at least one photon via two-photon transitions and of generating a single photon via a one-photon process is presented in figure for the case of the nano-disk. These probabilities are computed through the TPSE quantum yield $\text{QY}^{\text{TPSE}} = (\gamma_{ph,ph} + \gamma_{ph,pl})/\gamma$ and the single photon quantum yield $\text{QY}^{1q} = \Gamma_{ph}^{1q}/\Gamma^{1q}$, where Γ_{ph}^{1q} is the radiative contribution to the one-quantum transition rate Γ^{1q} . Surprisingly, we find that the fundamental dark mode D_1 acts as an amplifier of the TQSE photon-plasmon channel but as an attenuator of the one-photon pathway. For frequencies near ω_{D_1} , one-photon generation via TQSE is resonantly enhanced, being between two to four orders of magnitude larger than photon creation via standard one-quantum emission. On the other hand, there is also a broadband enhancement of $\text{QY}^{\text{TPSE}}/\text{QY}^{1q}$ that takes place within regions of frequencies below ω_{B_1} . These two kinds of enhancements are of a complete different nature. The resonant enhancement arises from the TPSE photon-plasmon emission channel that boosts QY^{TPSE} via a non-radiative Lorentzian resonance, while QY^{1q} is spectrally flat and much smaller than QY^{TPSE} near ω_{D_1} . The broadband enhancement results from the fact that QY^{1q} and QY^{TPSE} have spectrally aligned resonant responses along the fundamental bright mode B_1 , and as one moves to lower frequencies the former decreases faster than the latter.

Graphene nanostructures can also make the total one- and two-quanta SE competitive through tailoring the mobility μ or the Fermi energy E_F of graphene. For example, for a hydrogen emitter initially prepared in its $4s$ state, $\Gamma_{4s \rightarrow 3s} \simeq 1.9 \times 10^8 \text{ s}^{-1}$ while the fastest competing one-quantum electric dipole transition gives $\Gamma_{4s \rightarrow 3p}^{1q} \simeq 1.2 \times 10^8 \text{ s}^{-1}$

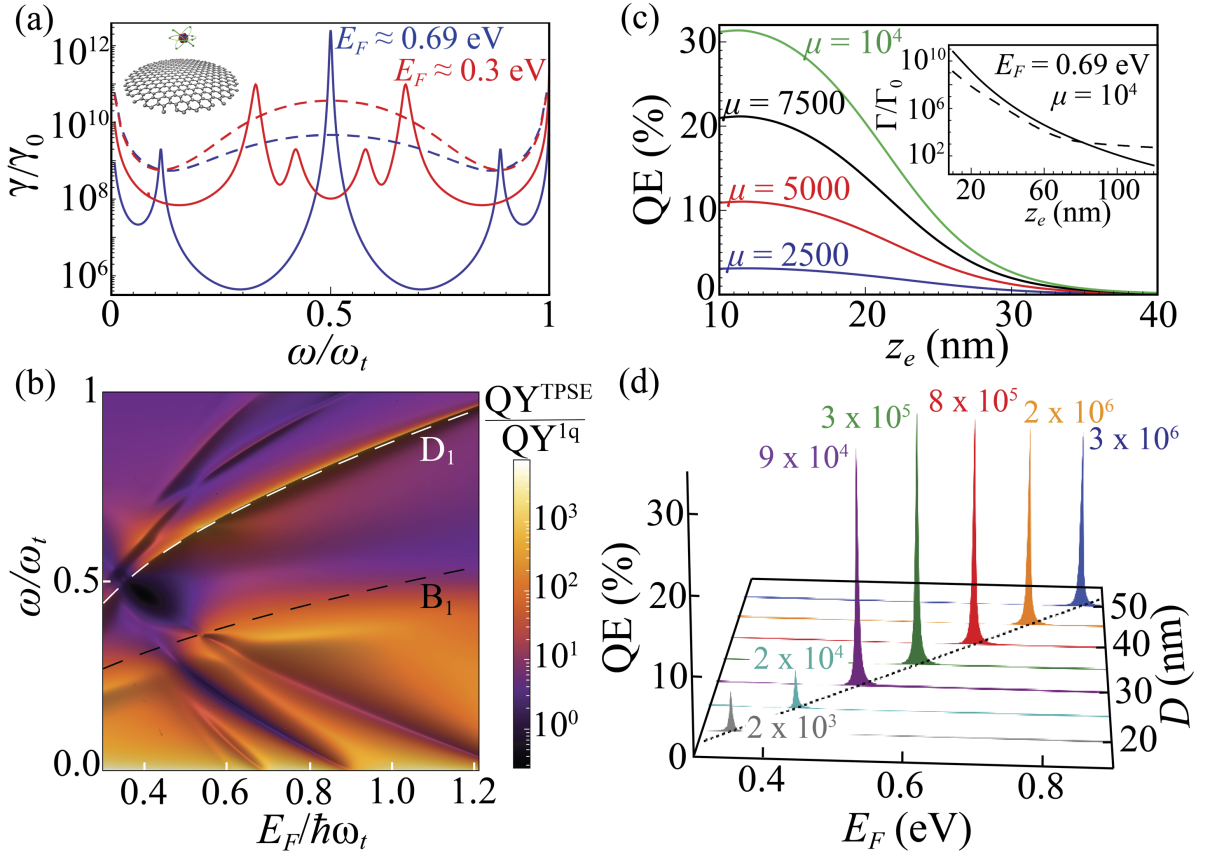


Figure 3.13: (a) Spectral TQSE for a graphene nano-disk (solid, $D = 40 \text{ nm}$) and a graphene monolayer (dashed), for an emitter with $\hbar\omega_t = 0.66 \text{ eV}$ located at $z_e = 10 \text{ nm}$. Graphene's conductivity is modeled using intra- and inter-band contributions, mobility is $\mu = 2500 \text{ cm}^2 \text{ V}^{-1} \text{ s}^{-1}$, and temperature is $T = 300 \text{ K}$. (b) Ratio of quantum yields between two- and one-quantum processes for the nano-disk. (c) Quantum efficiency versus distance for the TQSE $4s \rightarrow 3s$ transition in hydrogen (μ is in units of $\text{cm}^2 \text{ V}^{-1} \text{ s}^{-1}$). Inset: TQSE rate versus z_e for the nano-disk (solid) and monolayer (dashed). (d) QE as a function of E_F and D . The numbers near each QE profile show the photon-photon Purcell factor $\Gamma_{ph,ph}/\Gamma_0$, where $\mu = 10^4 \text{ cm}^2 \text{ V}^{-1} \text{ s}^{-1}$ and Γ_0 is the free-space TPSE rate.

for a graphene nano-disk at a distance $z_e = 10$ nm from the emitter ($D = 40$ nm, $E_F = 0.69$ eV, and ultra-high mobility $\mu = 10^4 \text{ cm}^2 \text{ V}^{-1} \text{ s}^{-1}$). In Fig. 3.13c,d we compare the TQSE rate for the $4s \rightarrow 3s$ transition in a hydrogen emitter with the competing one-quantum emission pathways. For separations $z_e \lesssim 20$ nm the quantum efficiency $\text{QE} = \Gamma_{4s \rightarrow 3s}/(\Gamma_{4s \rightarrow 3s} + \Gamma_{4s \rightarrow 3p}^{1q} + \Gamma_{4s \rightarrow 2p}^{1q})$ reaches values $\sim 30\%$, which are much higher than in graphene monolayers [10] (see Sec. 3.1.2). Also, for distances $z_e \lesssim 80$ nm the total TQSE rate is larger in graphene nanostructures than in graphene monolayers, highlighting that the finite-size of the system is pivotal to achieving giant emission rates. For any disk diameter the QE can also be controlled by changing the Fermi energy, with optimized performance when $\omega_{B_1}(D) = \omega_t/2$, (dotted curve in the (E_F, D) plane in Fig. 3.13d). For $E_F \lesssim \hbar\omega_t/2$, interband transitions in graphene lead to the generation of entangled electron-hole pairs, which dominate over plasmonic excitations and suppress the total TQSE (left-most two peaks).

In conclusion, we demonstrate that graphene nanostructures are a much better material platform for enhancing and tailoring TQSE than previously considered systems such as extended graphene [10] and polar dielectrics [14]. With these systems, we not only achieve higher spectral enhancements and quantum efficiencies, but also a fine control over the two-quanta emission spectrum and a significant amount of naturally produced photons. We believe that this system is a very promising source of on-demand frequency selected entangled photons for quantum information technologies.

Chapter 4

The Casimir effect

The Casimir effect is a well-known phenomenon in the scientific community thanks to the seminal work of Casimir [15], in which an attraction between two neutral perfectly conducting plates located in vacuum was predicted. Nevertheless, this effect has its origin in colloidal chemistry [17] and is closely related to dispersive London-van der Waals interactions. In 1930, London showed for the first time that two neutral but polarizable atoms attract each other, with an interaction potential given by $V_{Lon}(r) \approx -(3/4)\hbar\omega_0\alpha^2/r^6$ [146], where ω_0 is the atom dominant transition frequency, α the static polarizability, and r the distance between the atoms. However, some experiments with colloids have demonstrated that this power law is not correct for large separations, which led Casimir and Polder to consider the retardation effects on van der Waals forces between two atoms and between an atom and a perfect mirror [147]. The questions that emerged after this work resulted in a novel idea for obtaining the interaction energy between neutral bodies, namely, by calculating the variation on the electromagnetic field zero-point energy [2,148] due to the presence of the atoms [149]. The famous case of Casimir effect between two conducting plates was studied later using the same methodology, but it was published first and then became the standard example. Hence, it should be made clear that Casimir forces are a ubiquitous interaction and exist between any material objects.

Despite the beauty and simplicity of the Casimir method, computing the Casimir force between real materials in this way can be extremely hard or even infeasible [26]. In 1956,

Lifshitz and co-authors were the first to develop a general framework for calculating the Casimir force between two semi-infinite dispersive media at finite temperatures [150, 151]. In their formalism, instead of computing the variation in the electromagnetic field zero-point energy due to the presence of the media, they calculated the zz -component of the Maxwell stress tensor over the surface of the dispersive medium, which is equal to the derivative of the linear momentum per unit area [64]. After Lifshitz work, the field of Casimir physics expanded rapidly, attracting increasing interest not only of quantum field theorists, but also of experimental physicists [16, 152, 153]. The first experimental attempt to measure the standard Casimir force between two metallic plates was made by Sparnaay in 1958 [154]. However, due to difficulties regarding the parallelism between the plates and the intensity of the force the experiment lacked the necessary accuracy and was only able to show compatibility between data and theory, i.e., it did not disprove the existence of the Casimir effect. It was only in 1997 that Lamoreaux ushered the precision experiments era of the Casimir field after measuring the Casimir force by avoiding the parallelism problem in a torsion pendulum experiment [155, 156]. After this landmark experiment in the history of the Casimir effect, a modern series of experiments in the Casimir field started [25, 157].

Far from being a subject from the past, the field of Casimir physics has become a platform for bridging concepts from condensed matter, high energy and computational physics, and even biology, where the adhesion of geckos to walls has become a poster for such interactions [21, 22]. And with the recent advances in materials science, especially in low-dimensional materials, composites, and biosystems, the scientific community has gained new impetus to the study of dispersive interactions. In this chapter we present the fundamental physics behind the Casimir effect. In section I we discuss the Casimir method in the standard case of two parallel perfectly conducting plates, paying close attention to the typical magnitude of the force, sign and scaling law. In section II we provide a simple demonstration of the Lifshitz formula by considering the Casimir interaction in

one dimension. The demonstration is carried within the scattering approach [158] for any extended material bodies at zero or finite temperatures.

4.1 Casimir force between two perfect mirrors

Consider two perfectly conducting plates placed at $z = 0$ and $z = a$. The Casimir's method states that the interaction energy per unit area between both plates can be symbolically expressed as [2, 17]

$$E = \frac{1}{A} \left[\left(\sum_{\mathbf{k}\lambda} \frac{\hbar\omega_k}{2} \right)_I - \left(\sum_{\mathbf{k}\lambda} \frac{\hbar\omega_k}{2} \right)_{II} \right], \quad (4.1)$$

where the first term in brackets (I) is the electromagnetic field zero-point energy computed with the boundary conditions imposed by the mirrors taken into account and the second term (II) is the free-space zero-point energy. As studied in section 1.1.4, the boundary conditions imposed by the mirrors constrain the field modes wavevectors so that $k_z = n\pi/a$ is a discrete parameter. By using the dispersion relation $\omega_k = c\sqrt{k_{\parallel}^2 + k_z^2}$ and taking the limit to the continuum $\sum_{\mathbf{k}_{\parallel}} \rightarrow \frac{A}{(2\pi)^2} \int d\mathbf{k}_{\parallel}$ (and also $\sum_{k_z} \rightarrow \frac{a}{2\pi} \int dk_z$ for the free-space zero-point energy) we have

$$E(a) = \frac{\hbar c}{2} \int \frac{d\mathbf{k}_{\parallel}}{(2\pi)^2} \left[k_{\parallel} + 2 \sum_{n=1}^{\infty} \left(k_{\parallel}^2 + \frac{n^2\pi^2}{a^2} \right)^{1/2} \right] - \frac{\hbar c}{2} \int \frac{d\mathbf{k}_{\parallel}}{(2\pi)^2} \int_{-\infty}^{\infty} a \frac{dk_z}{(2\pi)} 2\sqrt{k_{\parallel}^2 + k_z^2}, \quad (4.2)$$

where we divided the term $n = 0$ by 2 since in this case there is only one possible polarization, as can be seen if we take $k_z = 0$ in Eqs. (1.8) and (1.9).

We notice that both zero-point energies (with and without the mirrors) diverge, which is a well-known feature of quantum field theory as a whole. Therefore, this difference is ill-defined and must be regularized. Here we will regularize the zero-point energy by introducing an exponential function inside both summations, which can be justified by the fact that a real metal becomes transparent in the limit $\omega \rightarrow \infty$. As a consequence, the high frequency contributions with and without the plates should cancel each other and

we are allowed to just ignore them in our idealized system. After making the substitution of variables $\lambda^2 = k_{\parallel}^2 + k_z^2$ we obtain

$$\begin{aligned} E_r(a, \epsilon) &= \frac{1}{2\pi} \left[\frac{1}{2} \int_0^\infty e^{-\epsilon k_{\parallel}} k_{\parallel}^2 dk_{\parallel} + \sum_{n=1}^{\infty} \int_{\frac{n\pi}{a}}^{\infty} e^{-\epsilon\lambda} \lambda^2 d\lambda - \frac{a}{\pi} \int_0^\infty dk_z \int_{k_z}^{\infty} e^{-\epsilon\lambda} \lambda^2 d\lambda \right] \\ &= \frac{1}{2\pi} \left[\frac{1}{\epsilon^3} + \sum_{n=1}^{\infty} \frac{\partial^2}{\partial\epsilon^2} \left(\frac{e^{-\epsilon n\pi/a}}{\epsilon} \right) - \frac{a}{\pi} \int_0^\infty dk_z \frac{\partial^2}{\partial\epsilon^2} \int_{k_z}^{\infty} e^{-\epsilon\lambda} d\lambda \right], \end{aligned} \quad (4.3)$$

where $E_r(a, \epsilon)$ is the regularized finite expression of the Casimir energy in Eq. (4.2). Notice that, as it should be in a regularization method, $E_r(a, \epsilon \rightarrow 0) = E(a)$. We also introduced the same regularization function in both zero-point energies, which is a consistency requirement for achieving the correct Casimir energy. Using the relation $\sum_{n=1}^{\infty} e^{-\epsilon n\pi/a} = \frac{1}{e^{\epsilon\pi/a}-1}$ and the definition of the Bernoulli numbers B_n [159],

$$\frac{1}{e^t - 1} = \sum_{n=0}^{\infty} B_n \frac{t^{n-1}}{n!}, \quad (4.4)$$

we obtain

$$E_r(a, \epsilon) = \frac{1}{2\pi} \left[\frac{6a}{\pi} (B_0 - 1) \frac{1}{\epsilon^4} + (1 + 2B_1) \frac{1}{\epsilon^3} + \frac{B_4}{12} \left(\frac{\pi}{a} \right)^3 + \sum_{n=5}^{\infty} \frac{B_n}{n!} (n-2)(n-3) \left(\frac{\pi}{a} \right)^{n-1} \epsilon^{n-4} \right]. \quad (4.5)$$

Finally, we insert the numerical values of the Bernoulli numbers $B_0 = 1$, $B_2 = -1/2$ e $B_4 = -1/30$, into the previous equation and take the limit $\epsilon \rightarrow 0^+$, which yields

$$E(a) = \lim_{\epsilon \rightarrow 0^+} E_r(a, \epsilon) = -\frac{\pi^2}{720} \frac{\hbar c}{a^3}. \quad (4.6)$$

We notice that the divergent terms cancel each other in the regularized subtraction, and only the term which depends on the distance between the plates remain.

The Casimir force per unit area (also referred as the Casimir pressure) is given by the derivative of the energy with respect to the distance between the plates,

$$F(a) = -\frac{d}{da} E(a) = -\frac{\pi^2}{240} \frac{\hbar c}{a^4} \approx -0.013 \frac{1}{(a/\mu m)^4} \frac{dyn}{cm^2}. \quad (4.7)$$

For a separation distance of $1\mu m$, the Casimir pressure is about $10^{-8} atm$, which is significantly small. This is one of the reasons why the Casimir effect took almost fifty years

from its prediction to be accurately measured in laboratory [155]. We also notice a rather simple distance scaling law of the force, that goes with a^{-4} . As we shall discuss later, this power law is not universal, being valid for some real materials only at zero temperature and in the long-distance regime.

4.2 Lifshitz formula

In this section, we focus our attention on the Casimir effect between real materials. The theoretical framework for computing the Casimir force can be rather complicated depending on the materials properties and geometry of the system [26, 160]. However, the Casimir energy per unit area between two parallel layers, which is the geometry we consider in the following chapter, can be obtained by the Lifshitz formula. This formula is valid for separations much larger than the interatomic distances of the materials, when the dielectric and permittivity functions are well defined. Here, we present a simple derivation of the Lifshitz formula by considering the variation of the zero-point energy due to the introduction of two layers of real materials within the scattering approach [161]. For simplicity, we consider only the Casimir effect in one dimension, which can be easily generalized to the three-dimensional case we are interested in. We start by calculating the zero-temperature Casimir energy and then consider the finite temperature interaction by modifying the expectation values of the number of photons in each field mode.

4.2.1 Scattering approach for the zero-temperature Casimir effect

Let's consider a one-dimensional Fabry-Pérot cavity consisting of two infinite material plates in vacuum separated by a distance d , as portrayed in Fig. 4.1. The Casimir interaction between both plates is given by the variation in the zero-point energy of the electromagnetic field. Therefore, we are left with the task of calculating the vacuum energy in the presence of the optical cavity and subtracting spurious infinite terms. In

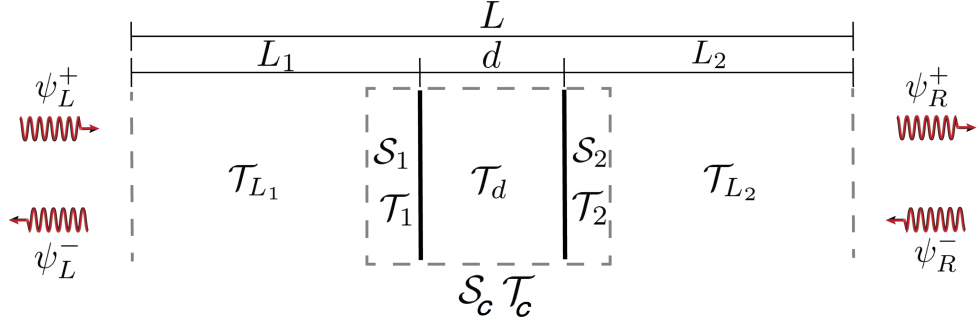


Figure 4.1: Optical object consisting of a Fabry-Pérot cavity of size d in a quantization box of length $L = L_1 + L_2 + d$.

order to do that, we first find the allowed field mode frequencies of an optical object using a scattering (\mathcal{S}) and a transfer (\mathcal{T}) matrix, which are defined by the relations

$$\begin{bmatrix} \psi_R^+ \\ \psi_L^- \end{bmatrix} = \mathcal{S} \begin{bmatrix} \psi_L^+ \\ \psi_R^- \end{bmatrix}, \text{ with } \mathcal{S} = \begin{bmatrix} t & \bar{r} \\ r & \bar{t} \end{bmatrix}; \quad (4.8)$$

$$\begin{bmatrix} \psi_R^+ \\ \psi_R^- \end{bmatrix} = \mathcal{T} \begin{bmatrix} \psi_L^+ \\ \psi_L^- \end{bmatrix} \text{ with } \mathcal{T} = \frac{1}{\bar{t}} \begin{bmatrix} \det \mathcal{S} & \bar{r} \\ -r & 1 \end{bmatrix}. \quad (4.9)$$

In the previous equations, ψ_L^+ (ψ_L^-) and ψ_R^+ (ψ_R^-) are the fields on the left and right sides of the system, respectively, that propagate to the right (left) direction. Also, r (\bar{r}) and t (\bar{t}) are the reflection and transmission coefficients for modes propagating from the left (right) side of the cavity. By definition, the scattering matrix relates the incident field with the output, *i.e.*, the field scattered by the optical object, while the transfer matrix relates the field on the left side with the field on the right side of the system. The relation between the transfer and scattering matrix stems from their definitions, and can be explicitly verified by rearranging Eq. (4.8) so that ψ_R^\pm are brought to the left side of the equation and ψ_L^\pm to the right side. Considering a quantization box of length L with periodic boundary conditions, we must have

$$\mathcal{T}_{L_2} \mathcal{T}_c \mathcal{T}_{L_1} \begin{bmatrix} \psi_L^+ \\ \psi_L^- \end{bmatrix} = \begin{bmatrix} \psi_R^+ \\ \psi_R^- \end{bmatrix} = \begin{bmatrix} \psi_L^+ \\ \psi_L^- \end{bmatrix}, \quad (4.10)$$

where $L_1 + L_2 = L$ and $\mathcal{T}_{L_i} = \text{diag}(e^{ikL_i}, e^{-ikL_i})$ is the free-space transfer matrix of a region with length L_i . As a consequence, the condition $\det(\mathcal{T}_{L_2} \mathcal{T}_c \mathcal{T}_{L_1} - \mathbb{I}) = 0$ must be

satisfied, which results in

$$z_k^2 - (t_c + \bar{t}_c)z_k + \det\mathcal{S}_c = 0, \quad (4.11)$$

where we defined $z_k = e^{-ikL}$. The previous equation allows us to determine the mode frequencies since $\omega_k = kc = i \log(z_k)c/L$. By multiplying the two solutions and taking the logarithm of the result we have

$$\omega_{n1} + \omega_{n2} = -i \frac{c \log(\det\mathcal{S}_c)}{L} + \frac{2n\pi c}{L}, \quad (4.12)$$

where $n = 0, 1, 2, \dots$. Interestingly, the free-space contribution readily appears in the second term of the right hand side of this expression, which facilitates the task of subtracting it from the Casimir energy. We then perform the summation of the first term of this equation in order to obtain the zero-point energy of the cavity as a whole, obtaining

$$E = \frac{i\hbar c}{2L} \sum_n \log(\det\mathcal{S}_c). \quad (4.13)$$

In the previous equation, the Casimir energy was written as a sum of a function of the cavity scattering matrix. It is convenient, however, to write the scattering matrix of the cavity in terms of the scattering matrices of each layer, namely, \mathcal{S}_1 and \mathcal{S}_2 . This can be done by using that $\mathcal{T}_c = \mathcal{T}_2 \mathcal{T}_d \mathcal{T}_1$, where \mathcal{T}_i is the transfer matrix of layer i and $\mathcal{T}_d = \text{diag}(e^{ikd}, e^{-ikd})$ is the free-space transfer matrix within the region inside the cavity. This free-space contribution must also be subtracted, which can be accomplished by calculating $\tilde{\mathcal{T}}_c = \mathcal{T}_d^{-1} \mathcal{T}_c$ instead of \mathcal{T}_c . Combining this with the general relation between the transfer and scattering matrices of an object given by Eq. (4.9) we obtain

$$\frac{\tilde{\mathcal{T}}_c}{\bar{t}_1 \bar{t}_2} = \det\tilde{\mathcal{S}}_c = \det\mathcal{S}_1 \det\mathcal{S}_2 e^{i\Delta(k)}, \quad (4.14)$$

where

$$e^{i\Delta(k)} = \frac{1 - \bar{r}_1^* r_2^* e^{-2ikd}}{1 - \bar{r}_1 r_2 e^{2ikd}}. \quad (4.15)$$

Hence, Eq. (4.14) implies that $\log(\det\tilde{\mathcal{S}}_c) = \log(\det\mathcal{S}_1) + \log(\det\mathcal{S}_2) + i\Delta(k)$ and we have three contributions to the Casimir energy of the cavity. The contributions of $\log(\det\mathcal{S}_1)$

and $\log(\det\mathcal{S}_2)$ are the variation in the zero-point energy due to the presence of one material body as if the other does not exist, while the term $i\Delta(k)$ depends on the distance between the plates and gives the Casimir interaction between both layers. Therefore, we need only to consider the last term in the summation over modes, which yields

$$\begin{aligned} E &= -\frac{\hbar c}{L} \sum_n \text{Im} [\log(1 - \bar{r}_1 r_2 e^{2ikd})] \\ &= \frac{\hbar c}{2\pi} \int_0^\infty dk \text{Im} [\log(1 - \bar{r}_1 r_2 e^{2ikd})], \end{aligned} \quad (4.16)$$

where we used the identity $\log(z^*/z) = -2i\text{Im}(\log z)$ and in the last step we took the limit to the continuum by replacing $\sum_n \rightarrow \frac{L}{2\pi} \int_0^\infty dk$. The beauty of this equation is that all relevant characteristics of the plates to the Casimir interaction are encoded in their Fresnel reflection coefficients. Also, this expression is valid for any thickness of the materials since the reflection coefficients already take this into account.

4.2.2 Wick rotation

Eq. (4.16) allows us to calculate the Casimir energy between two arbitrary infinite layers once we know their Fresnel reflection coefficients r_1 and r_2 . However, this equation is not convenient from a mathematical point of view since in the real frequency domain there are several resonances that must be handled carefully [162, 163]. One must also split the integration between evanescent and propagating modes and the distance dependence of each contribution is not clear due to the coupling between the real and imaginary parts of e^{2ikd} . Luckily, the Casimir force calculation is incredibly easier when it is analyzed in the complex plane. In this section we shall use a trick called the Wick rotation to rewrite Eq. (4.16) as an integral over imaginary frequencies, which will make the distance dependence of the Casimir interaction more explicit and simplify further calculations. To this end, it is convenient to work with the Casimir force, $F = \partial E / \partial d$ rather than the Casimir energy. The Casimir force can be written as

$$F = \frac{\hbar}{\pi c} \text{Re} \left[\int_0^\infty d\omega G(\omega) \right] \quad (4.17)$$

where we used the change of variable $\omega = kc$ and defined

$$G(\omega) = \frac{\omega \bar{r}_1 r_2 e^{2i\omega d/c}}{1 - \bar{r}_1 r_2 e^{2i\omega d/c}} \quad (4.18)$$

This integral can be solved by defining a closed contour in the complex plane given by $\mathcal{C} = \mathcal{C}_{\text{Re}} + \mathcal{C}_{\text{Im}} + \mathcal{C}_R$, where \mathcal{C}_{Re} is a line in the real axis ranging from $z = 0$ to $z = R$, \mathcal{C}_{Im} is a line in the imaginary axis from iR to 0, and \mathcal{C}_R is a quarter of a circle of radius R that connects the points $(R, 0)$ and $(0, R)$. From the residue theorem we get

$$\oint_{\mathcal{C}} dz G(z) = \int_0^R d\omega G(\omega) + \int_{iR}^0 dz G(z) + \int_{\mathcal{C}_R} dz G(z) = 0. \quad (4.19)$$

Now we take the limit $R \rightarrow \infty$, where the contribution of \mathcal{C}_R vanishes and we are left with

$$\int_0^\infty d\omega G(\omega) = \int_0^\infty d\xi G(i\xi), \quad (4.20)$$

where we defined $\xi = -iz$ in the integral over \mathcal{C}_{Im} . After substituting the previous equation into (4.17) we have

$$F = -\frac{\hbar}{\pi c} \int_0^\infty d\xi \frac{\xi \bar{r}_1(i\xi) r_2(i\xi) e^{-2\xi d/c}}{1 - \bar{r}_1(i\xi) r_2(i\xi) e^{-2\xi d/c}}, \quad (4.21)$$

which can be derived from the following Casimir energy:

$$E = \frac{\hbar}{2\pi} \int_0^\infty d\xi \log(1 - \bar{r}_1(i\xi) r_2(i\xi) e^{-2\xi d/c}). \quad (4.22)$$

This is the zero-temperature Lifshitz formula for the Casimir energy in one dimension. Notice that, the Fresnel coefficients, which in general are frequency-dependent, must be evaluated at the imaginary frequencies $i\xi$. Also, the integrand now is a real function, and the distance dependence of each mode contribution to the Casimir interaction is given by the exponential factor $e^{-2\xi d/c}$, which implies that the retarded Casimir effect is governed by the low-frequency response of the materials.

4.2.3 Finite temperature Casimir energy

Until now we discussed the Casimir effect at zero temperature. In order to consider a system in thermal equilibrium at temperature T , it is necessary to account for the

electromagnetic field fluctuations arising from thermal photons. This can be done by modifying the zero-point energy as

$$\sum_k \frac{\hbar\omega_k}{2} \rightarrow \sum_k \hbar\omega_k \left[\frac{1}{2} + \tilde{n}(\omega_k) \right], \quad (4.23)$$

where $\tilde{n}(\omega_k) = (e^{\hbar\omega_k/k_B T} - 1)^{-1}$ is the Bose-Einstein distribution for the average number of photons with frequency ω_k and k_B is the Boltzmann constant. Following the same steps discussed in the previous subsections, we obtain an integrand that is no longer analytical in the upper complex plane, presenting infinite isolated simple poles at the Matsubara frequencies $\xi_n = 2\pi k_B T n / \hbar$ ($n = 0, 1, 2, \dots$). After performing the calculations by circumventing the equally spaced poles in the imaginary axis, one finds

$$E = k_B T \sum_n \log \left(1 - \bar{r}_1(i\xi) r_2(i\xi) e^{-2\xi_n d/c} \right), \quad (4.24)$$

which is the one-dimensional finite temperature Casimir energy. We notice that, the high temperature limit is somewhat equivalent to the long distance regime since both require only knowledge of the low-frequency optical response of the materials. The $T = 0$ Casimir energy can be obtained from the finite temperature Lifshitz formula by applying the transformation $k_B T \sum_n \rightarrow \frac{\hbar}{2\pi} \int_0^\infty d\xi$.

Finally, we discuss the generalization of Eq. (4.24) to three dimensions. In this case, we must add an integration over the parallel components of the wavevector \mathbf{k} and a sum over the two s- and p-polarized waves, that may couple in a reflection process depending on the material anisotropy. The Casimir energy per unit area is then given by

$$E = k_B T \sum_n' \int \frac{d^2 \mathbf{k}_\parallel}{(2\pi)^2} \log \det \left(1 - \mathbb{R}_1 \cdot \mathbb{R}_2 e^{-2k_{z,n} d} \right), \quad (4.25)$$

where $k_{z,n} = \sqrt{\mathbf{k}_\parallel^2 + \xi_n^2/c^2}$, and the prime on the summation symbol indicates that the term $n = 0$ must be multiplied by 1/2. Also, \mathbb{R}_i are the reflection matrices for each sheet, with rows given by the Fresnel coefficients for incident s- and p-polarized waves. As before, these reflection matrices encode all complexity regarding the optical properties

of the materials. Since the integrand inside the Lifshitz formula decays with $e^{-2\xi d/c}$, for sufficiently large separations or high temperatures, the low-frequency optical response of the materials dictates the Casimir force. Therefore, the integrand can be expanded as a power series of $i\xi$ and we may retain only the leading contribution (while keeping the exponential factor). In the following chapter, we shall apply this theory in some cases of interest, namely, Casimir forces between graphene monolayers and graphene family materials under external fields. For now, let's only consider the standard Casimir energy by assuming both layers can be described by perfect mirrors. The reflection matrices yield $\mathbb{R}_{ss} = \mathbb{R}_{sp} = \mathbb{R}_{ps} = 0$ and $\mathbb{R}_{pp} = 1$. By performing the integration in the zero-temperature limit it is simple to show that Eq. (4.25) results in Eq. (4.6).

Chapter 5

Casimir effect in the flatland

The reduced dimensionality that can be achieved in isolated graphene monolayers and their related nanostructures raises the possibility of studying the Casimir effect between materials with peculiar dielectric properties and reveals insights in the nature of the Casimir interaction. These features have led to the discovery of novel behaviours in the Casimir force, which have a strong dependence on temperature and doping [164, 165], as demonstrated in experimental measurements [166]. Casimir force gradient experiments also have shown that the Casimir interaction between dielectric media is substantially diminished when one of them is covered with graphene [167]. Meanwhile, quantum Hall physics arising from externally applied magnetic fields results in a complex and rich magneto-optical response of graphene [168]. This was already exploited for tuning and screening dispersive interactions, which were shown to be quantized and significantly weaker when compared to the situation without the field [169, 170].

On the other hand, two-dimensional Dirac materials such as silicene, germanene, stanene, and plumbene are representatives of the graphene family and present several possible topological phase transitions¹ under external fields due to their significant spin-orbit coupling and finite staggering [173, 174]. These phase transitions strongly impact

¹Topological insulators are quantum materials characterized by distinct conducting surface states (edge states in case of two-dimensional media) that show up due to a non-trivial topological character of the electronic wave functions. We will not discuss this rich subject in this thesis, but we recommend Refs. [171, 172] as good introductions to topological matter and topological phase transitions.

their Casimir forces, in which different scaling laws, repulsion, and force quantization are possible [175]. Moreover, vertically stacking of different two-dimensional materials held by Van der Waals interactions is an emerging scientific direction since it allows one to design the properties of the final stacked material [176, 177]. And as recent studies have shown, the Casimir effect affects the electronic and phonon properties of these Van der Waals heterostructures [178], which is important for their transport and optical applications. For all the above reasons, the study of Casimir interactions in the flatland, in particular with graphene family materials, is of extreme relevance.

In this chapter we present the unusual Casimir interactions that exist in graphene and graphene family materials. In the first section we discuss graphene-graphene Casimir forces, and demonstrate how the introduction of a magnetic field allows one to achieve repulsive Casimir interactions and control for its magnitude and sign. In section II we study the Casimir effect in other graphene family materials, where photo-induced topological phase transitions play a key role in determining the final Casimir force. Finally, we join the knowledge of the previous sections and consider the simultaneous impact of topological phase transitions and quantum Hall physics in the Casimir force between graphene family layers [179]. As we demonstrate, there are numerous advantages and intricate effects that arise from the interplay between both phenomena.

5.1 Casimir forces between graphene sheets

The Casimir effect between graphene monolayers has been extensively studied in the last decade [164, 180–184]. The simplest (and yet very general) method for calculating the graphene/graphene Casimir interaction is by inserting their Fresnel coefficients into the Lifshitz formula. In the case of two neutral graphene sheets at zero temperature, the conductivity is a constant given by $\sigma = \sigma_0 = e^2/(4\hbar)$, and the Casimir energy per unit

area yields [164]

$$E_g = -\frac{\hbar c \alpha}{32\pi d^3}, \quad (5.1)$$

where $\alpha = e^2/(4\pi\epsilon_0\hbar c) \approx 1/137$ is the fine structure constant. We notice that the neutral graphene/graphene interaction has the same distance scaling law as the Casimir energy of two perfectly conducting plates obtained in Eq. (4.6). However, the magnitude of the Casimir force is reduced by a factor α , which is why graphene can be used to screen dispersive interactions. Since the Casimir force per unit area is given by $F = -\partial E/\partial d$, we have $F_g < 0$, which results in an attraction between the graphene monolayers.

The fact that the undoped graphene interaction has the same distance scaling law as the case of two ideal metals is astonishing since this is not the case of most real materials such as dielectric media. This feature is strongly connected to the fact that both systems do not present a characteristic length scale since their optical properties are described by constant response functions. Indeed, it is known that thermal effects provide such scale, which is given by $\xi_T = \hbar v_F/k_B T \approx 26$ nm at room temperature [181]. For separations between the two layers smaller than the thermal length, the zero-temperature result for the Casimir energy prevails, while for separations larger than the thermal length, the force crosses over to a linear universal regime where $E_g \sim T/d^2$ is independent of any material parameter. On the other hand, the effects of doping in the dispersive interaction between graphene sheets substantially enhance their Casimir force [184]. Nevertheless, the Casimir interaction of graphene can never surpass the force between ideal metals. In the next subsection we will discuss how the introduction of a magnetic field in the graphene/graphene system allows for an even higher screening of the Casimir interaction and also switching the sign of the force by controlling for doping in both sheets.

5.1.1 Repulsive quantized Casimir force with graphene

The fact that the presence of a magnetic field impacts the dynamics of charged particles is a well-known feature of electromagnetism. An important phenomenon related

to this type of interaction is the Hall effect, which consists on the production of a voltage difference in a conductive material that causes an electric field perpendicular to the original electric current and to the applied magnetic field [64]. Meanwhile, low-energy electrons in graphene present a relativistic nature that gives birth to an unusual quantum Hall effect, measured in laboratory by K. S. Novoselov *et al* and also by Y. Zhang *et al* in 2005 [185, 186]. This quantum Hall effect is characterized by a quantized electrical conductivity, which originates on the discrete energy levels of the relativistic electron gas in graphene, also known as Landau levels [168, 187, 188]. In this subsection we show how the quantum Hall effect impacts the Casimir force between two graphene monolayers, allowing for tuning its magnitude and changing the attractive character of the interaction to a repulsion between the graphene sheets.

First, let's discuss the magneto-optical properties of graphene under the influence of a strong externally applied magnetic field perpendicular to the surface, B_z . Due to time-reversal symmetry breaking, the local graphene conductivity in this situation is a 2-ranked tensor. The longitudinal (σ_{xx}) and Hall (σ_{xy}) conductivities can be obtained by a standard Kubo approach within the conical approximation for the band structure, and are given by [188]

$$\sigma_{xx} = \sigma_{yy} = \frac{2E_B^2\sigma_0\hbar(\xi + \Gamma)}{\pi} \sum_{n=0}^{\infty} \left[\frac{f_n - f_{n+1} + f_{-n-1} - f_{-n}}{(\varepsilon_{n+1} - \varepsilon_n)[(\varepsilon_{n+1} - \varepsilon_n)^2 + \hbar^2(\xi + \Gamma)^2]} + (n \rightarrow -n) \right], \quad (5.2)$$

$$\sigma_{xy} = -\sigma_{yx} = -\frac{2E_B^2\sigma_0}{\pi} \sum_{n=0}^{\infty} \left[\frac{f_n - f_{n+1} - f_{-n-1} + f_{-n}}{(\varepsilon_{n+1} - \varepsilon_n)^2 + \hbar^2(\xi + \Gamma)^2} + (n \rightarrow -n) \right], \quad (5.3)$$

where we evaluated the conductivity tensor at the Matsubara frequency $\omega = i\xi$. In the previous equations, $\varepsilon_n = \text{sgn}(n)\sqrt{|n|}E_B$ are the Landau energy levels of the system, with $E_B = \sqrt{2v_F^2\hbar|eB_z|}$ being the relativistic analog of the cyclotron energy. Also $f_n = 1/[e^{(\varepsilon_n - \mu)/k_B T} + 1]$ denotes the Fermi Dirac distribution, μ is the chemical potential, T is the absolute temperature, and Γ is the relaxation rate. The Landau energy levels are illustrated in Fig. 5.1a for a single Dirac cone. We notice that, at sufficiently small

temperatures ($k_B T \ll E_B$), only one intraband transition gives a relevant contribution to the conductivity due to the quasi-step function shape of the Fermi energy distribution. However, all interband transitions to Landau levels above the chemical potential play a role in the magneto-optical properties of graphene (with a higher weight for eigenenergies close to μ). In the limit of zero temperature and small dissipation, the DC ($\xi = 0$) Hall conductivity is quantized, which is the manifestation of the quantum Hall effect in graphene. This can be demonstrated by substituting $f_n = \theta(\mu - \epsilon_n)$ into the conductivities expressions, taking $k_B T = \hbar\xi = \hbar\Gamma = 0$, and performing the summation over the Landau levels, which yields [187]

$$\sigma_{xy} = \text{sgn}(eB_z\mu) \frac{e^2}{\hbar\pi} (2N + 1), \quad (5.4)$$

where $N = \lfloor \mu^2/E_B^2 \rfloor$ is the number of filled Landau levels per cone and $\lfloor \mu^2/E_B^2 \rfloor$ is the biggest integer smaller than μ^2/E_B^2 . We notice that the quantum Hall effect in graphene is unconventional, i.e., the conductivity is proportional to $2N + 1$ instead of N as the case of thick metals. This can be accounted on the higher degeneracy of the $n = 0$ Landau level in comparison to the higher energy levels. Finally, in this regime of zero temperature and dissipation, the DC longitudinal conductivity vanishes since all Landau levels below N are fully occupied.

In order to obtain the Casimir force between the two graphene monolayers subjected to a magnetic field we must insert their reflection matrices into the Lifshitz formula given by Eq. (4.25). If we consider two standing graphene sheets in free space, the reflection matrices components, i.e., the Fresnel coefficients, depend on the longitudinal and Hall conductivities and can be written as [169, 189, 190]

$$\mathbb{R}_{ss} = -\frac{2\pi}{\delta_n} \left[\frac{\sigma_{xx}\xi_n}{k_{z,n}c^2} + \frac{2\pi}{c^2} (\sigma_{xx}^2 + \sigma_{xy}^2) \right], \quad (5.5)$$

$$\mathbb{R}_{sp} = \mathbb{R}_{ps} = \frac{2\pi\sigma_{xy}}{\delta_n c}, \quad (5.6)$$

$$\mathbb{R}_{pp} = \frac{2\pi}{\delta_n} \left[\frac{\sigma_{xx}k_{z,n}}{\xi_n} + \frac{2\pi}{c^2} (\sigma_{xx}^2 + \sigma_{xy}^2) \right], \quad (5.7)$$

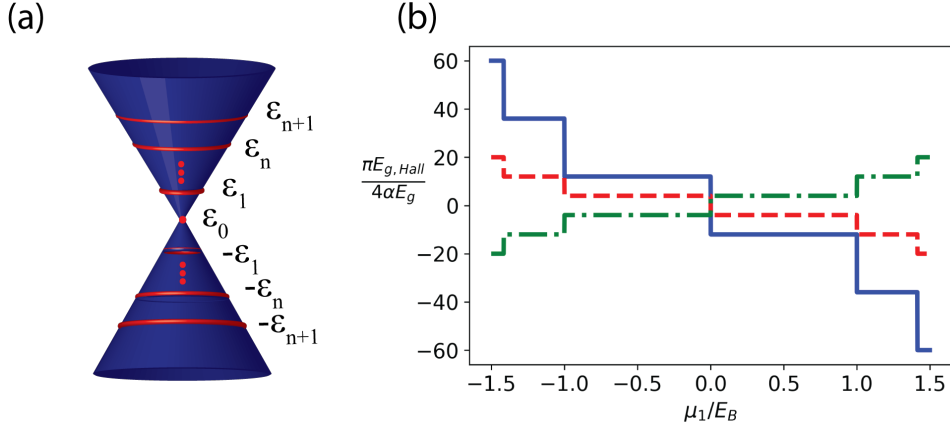


Figure 5.1: (a) Low-energy band structure of graphene for a non-zero magnetic field. The quantized Landau levels (red circles) are built on top of the Dirac cone. (b) Normalized Casimir energy given by Eq. (5.8) as a function of the chemical potential of a single graphene sheet for $\mu_2/E_B = \{1, 0.5, -0.5\}$ (solid blue, dashed red, and dash-dotted green, respectively).

where $\delta_n = 1 + \frac{2\pi\sigma_{xx}}{c} \left(\frac{\xi_n}{k_{z,n}} + \frac{k_{z,n}}{\xi_n} \right) + \frac{4\pi^2}{c^2} (\sigma_{xx}^2 + \sigma_{xy}^2)$ and the conductivity components are evaluated at the imaginary Matsubara frequencies $i\xi_n$. Here we restrict our analysis to the zero-temperature retarded Casimir effect. At $T = 0$, the Casimir energy is given by an integral over imaginary frequencies $i\xi$, which can be obtained by applying the transformation $k_B T \sum'_n \rightarrow \frac{\hbar}{2\pi} \int_0^\infty d\xi$ in Eq. (4.25). Since the integrand inside the Lifshitz formula decays with $e^{-2\xi d/c}$, for large separations ($d \gg \hbar c/E_B$) the graphene low-frequency optical response provides the dominant contribution. Hence, we can expand the integrand and retain only the leading term. By keeping only the DC Hall conductivity given by Eq. (5.4) we have $\mathbb{R}_{sp} = \mathbb{R}_{ps} \approx 2\pi\sigma_{xy}/c$ and $\mathbb{R}_{ss} = \mathbb{R}_{pp} \approx 0$, where we discarded σ_{xy}^2 since it gives a higher order contribution in α . By applying the relation $\log \det(1 + A) = \text{Tr} \log(1 + A) \approx \text{Tr}(A)$ to the integrand of the Lifshitz formula and using Eq. (5.4), we obtain [169]

$$\frac{E_{g,\text{Hall}}}{E_g} = -\frac{16\alpha}{\pi} \text{sgn}(\mu_1\mu_2)(2N_1 + 1)(2N_2 + 1), \quad (5.8)$$

where the normalization factor E_g is the graphene/graphene Casimir energy without the magnetic field given by Eq. (5.1). Also, μ_1 and μ_2 are the chemical potentials of the

two graphene sheets, which may be prepared at different doping levels, and N_1, N_2 are the number of filled Landau levels in both monolayers. We notice that $E_{g,\text{Hall}}$ has the same distance dependence as E_g , hence, the Casimir force normalized by the graphene-graphene force ($-\partial E_g / \partial d$) is also given by the previous equation. As a consequence, a negative (positive) normalized energy implies a repulsive (attractive) force. In Fig. 5.1b we plot the normalized Casimir energy of this system as a function of the chemical potential μ_1 for different values of (B_z, μ) . For two layers with the same charge carriers, i.e., $\text{sgn}(\mu_1) = \text{sgn}(\mu_2)$ the Casimir force in the long distance regime is repulsive, but the sign of the force is switched once $\text{sgn}(\mu_1) = -\text{sgn}(\mu_2)$. Also, the Casimir force presents signatures of the quantum Hall effect in graphene since it is quantized and proportionally to the Landau filling factors of the system. Finally, we mention that the introduction of a magnetic field provides an even higher suppression of the Casimir interaction, that now is α^2 times smaller than the mirror-mirror system. Nevertheless, we emphasize that, at the same time, this Casimir interaction is stronger than the Casimir force between ordinary two-dimensional insulators, which falls off especially rapidly ($F \sim d^{-6}$) at large distances [169].

5.2 Casimir effect in graphene family materials

Two-dimensional Dirac materials such as silicene, germanene, stanene, and plumbene (the allotropes of Si, Ge, Sn, and Pb, respectively) are representatives of the graphene family and present a honeycomb structure just like graphene. However, the two atoms in the unit cell are arranged in staggered layers separated by a distance 2ℓ , as depicted in Fig. 5.2a [173]. Graphene family materials were recently synthesized [191–193] and exhibit fascinating phenomena that find their importance in a broad range of applications [194]. As a consequence of their finite staggering and non-zero spin-orbit coupling (SOC), which is an effect caused by the intrinsic high mass of these atoms when compared to carbon, these materials are topological insulators and present several possible topological phase

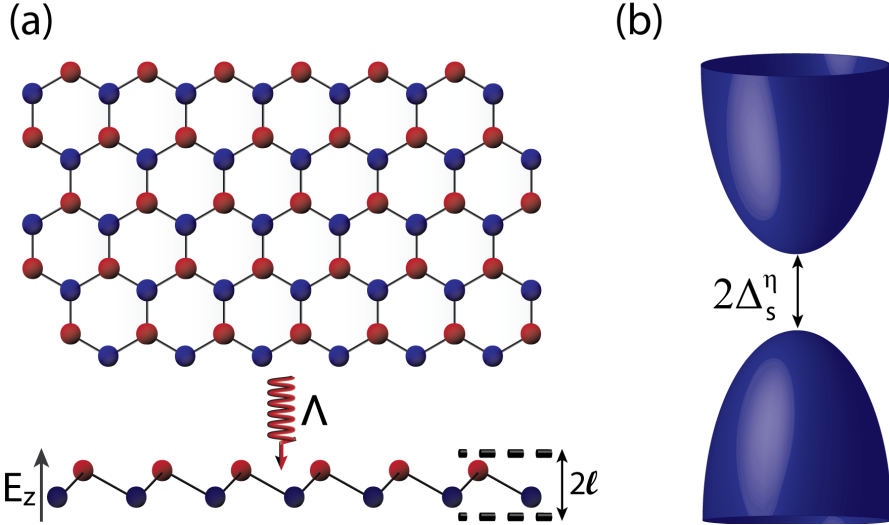


Figure 5.2: (a) Top and side views of the graphene family materials subjected to an externally applied electric (E_z) field, and a circularly polarized laser (Λ). The red and blue colored atoms in the honeycomb structure belong to inequivalent sublattices with a finite staggering 2ℓ between them. (b) Low-energy band structure around a given K or K' point. The gap Δ_s^n between the valence and conduction bands can be tuned by adjusting Λ and E_z .

transitions under external fields [195–197]. These photo-induced topological features show up in a variety of light-matter interaction phenomena, such as the photonic Spin Hall effect [174], quantum friction [198], and the quantum reflection [199]. Therefore, an investigation of the impact of these topological phase transitions in the Casimir forces between graphene family materials deserves our attention.

5.2.1 Topological phase transitions in the Casimir force

Let's start by discussing the graphene family materials main properties and optical response. Their low-energy band structure is obtained from a generalized Kane-Mele Hamiltonian, which emerges from a nearest neighbour tight binding model and is given by $H_s^\eta = v_F(\eta p_x \tau_x + p_y \tau_y) + \Delta_s^\eta \tau_z$ [173]. Here, τ_i , $i = 1, 2, 3$, are the Pauli matrices for sublattice pseudo spin, $\mathbf{p} = (p_x, p_y)$ is the momentum for particles around points K ($\eta = +1$) and K' ($\eta = -1$), $s = \pm 1$ is the spin degree of freedom, v_F is the Fermi velocity, and Δ_s^η is half the mass gap. The Dirac mass naturally arises from the SOC, λ_{SO} , but can

be modified by applying an out-of-plane electric field E_z , and a circularly polarized laser $\Lambda = \pm 8\pi\alpha v_F^2 I_0/\omega_0^3$ (with I_0 being the radiation intensity and ω_0 the oscillation frequency), leading to $\Delta_s^\eta = -\eta s \lambda_{SO} + e\ell E_z + \eta\Lambda$. The SOC for silicene, germanene, stanene, and plumbene are $\lambda_{SO} \approx 3.9, 43, 100, 200$ meV, respectively, which are much higher than the graphene SOC of a few μ eV. Terms originating from Rashba physics² are ignored because of their comparatively small effect. In Fig. 5.2b we represent a single Dirac cone of graphene family materials, which corresponds to their low-energy band structure. We observe that the graphene family Dirac cones have a parabolical shape since the Hamiltonian of the system yields an energy per cone of $\varepsilon_\pm = \pm\sqrt{\hbar^2 v_F^2 k^2 + (\Delta_s^\eta)^2}$, in contrast to the gapless linear cones of graphene.

The full optical conductivity of the graphene family can be obtained by the Kubo formula. In this discussion, we restrict ourselves to the DC conductivity without doping in the zero-temperature and dissipationless limit. When the gap is not closed, we have $\sigma_{xx} = 0$ just like graphene under the influence of a magnetic field, but the Hall conductivity can be written as

$$\sigma_{xy} = \frac{2\sigma_0}{\pi} C_{\text{ph}}, \quad (5.9)$$

where C_{ph} is the photo-induced Chern number and is given by [173]

$$C_{\text{ph}} = -\frac{1}{2} \sum_{\eta,s} \eta \operatorname{sgn}(\Delta_s^\eta). \quad (5.10)$$

The tunability of the Dirac gap for each spin and valley index allows these materials to exhibit a multitude of different electronic phases, many of which harbor non-trivial topological states. Each electronic phase corresponds to a different value of the Chern number, and by varying the external agents Λ and E_z one can induce topological phase transitions by closing the gap of one (or two) Dirac cone(s). In Fig. 5.3 we plot the topological phase

²The Rashba spin-orbit coupling is a phenomenological approximation that explains the split in energy of electron spin subbands in two-dimensional semiconductors and other materials such as topological insulators [200, 201]. Rashba physics refers to the study and exploration of this kind of interaction in novel physical phenomena, such as spin filtering and the control of electron trajectories.

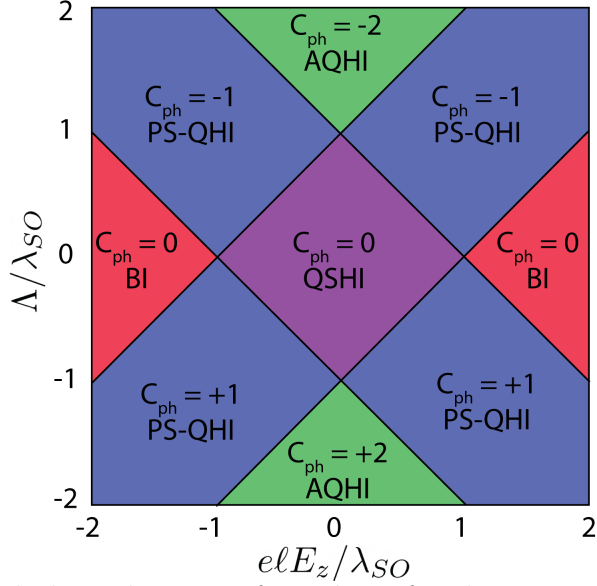


Figure 5.3: Topological phase diagram of graphene family materials. The displayed topological phases are the band insulator (BI), quantum spin Hall insulator (QSHI), polarized-spin quantum Hall insulator (PS-QHI), and anomalous quantum Hall insulator (AQHI).

diagram of graphene family materials in the $(\Lambda/\lambda_{SO}, e\ell E_z/\lambda_{SO})$ dimensionless plane. In this phase diagram, we notice that the system undergoes a topological phase transition whenever it crosses the black lines, where one Dirac cone closes, or when it crosses a vertex, where two Dirac cones close (as can be verified by substituting the vertex external agents values in Δ_s^η). The names given to each topological phase are related to the classification of topological insulators regarding their spin and valley Chern numbers, and dictates the behaviour of conductive electrons in these phases.

Such as the signatures of quantum Hall physics present in the Casimir force between graphene monolayers under the influence of a magnetic field, photo-induced topological features arise in the graphene family Casimir interaction. Indeed, the more relevant contribution to the zero-temperature Casimir energy in the long-distance regime at $\mu = 0$ is given by [175]

$$\frac{E_{gf}}{E_g} = -\frac{4\alpha}{\pi} C_{1,\text{ph}} C_{2,\text{ph}}. \quad (5.11)$$

as can be demonstrated after following the same steps taken when obtaining Eq. (5.8).

The Casimir force dependence on the distance between the sheets is exactly equal to the graphene-graphene Casimir force, but the interaction is repulsive and α times smaller than in graphene. We should note that, unlike the case of graphene in a magnetic field, we cannot tune the sign of this contribution to the force since the external agents are the same for both monolayers, which implies $\text{sgn}(C_{1,\text{ph}}) = \text{sgn}(C_{2,\text{ph}})$ for $C_{1,\text{ph}}, C_{2,\text{ph}} \neq 0$. In the case of $C_{1,\text{ph}} = 0$ (and/or $C_{2,\text{ph}} = 0$), Eq. (5.11) yields $E_{gf} = 0$ and higher order attractive contributions take place. This is only the case in the QSHI and BI phases. However, we mention that when the system is exactly at the black lines or vertices, the Casimir energy presents a graphene-like behaviour and is given by $E_{gf} = E_g/4$ (at the lines / when only one cone is closed) or $E_{gf} = E_g/2$ (at the vertices / when two cones are closed). This can be accounted on by the fact that closing the gap establishes an equivalence between the graphene and graphene family Dirac cones, so that the longitudinal conductivity does not vanish in a topological phase transition. Finally, we briefly comment on the role of the chemical potential in the graphene family Casimir interaction. As long as $|\mu| < |\Delta_s^\eta|$, for all Dirac cones the results described above are still valid since the electrons are still occupying the same states (at small temperatures). When $|\mu| > |\Delta_s^\eta|$, however, intraband transitions start being important and the system behaves like a conductor, which erases the topological insulator features in the Casimir force. The same happens at high temperatures (or high dissipations) since the topology of the system is encoded in the DC Hall conductivity.

From what has been presented so far in this chapter, it is natural to wonder which effects can be brought to the Casimir force as a consequence of coexistent topological and quantum Hall features in the flatland. Indeed, the disposal of this chapter was intended to achieve that. In the next subsection we present a complete study of the Casimir effect in this situation, namely, two infinite graphene family sheets subjected to the influence of a circularly polarized laser and externally applied electrical and magnetic fields.

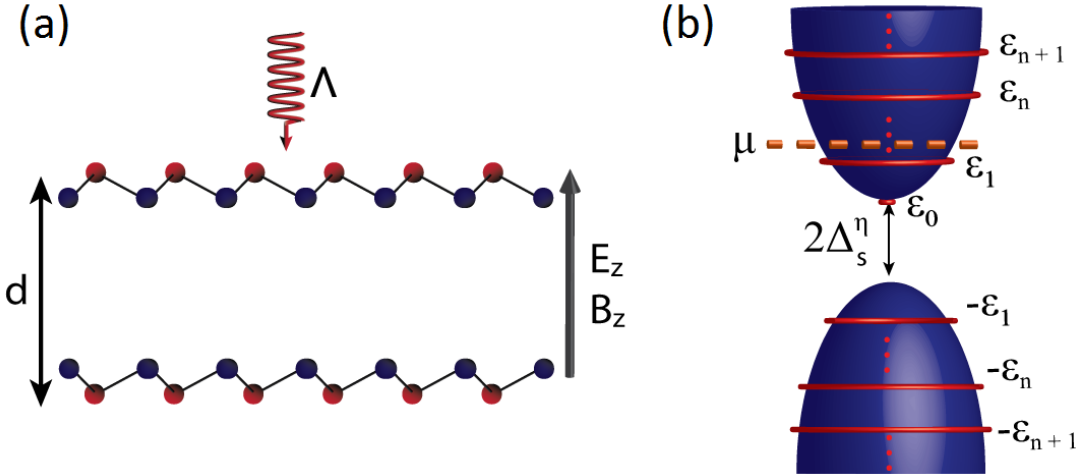


Figure 5.4: (a) Schematics of the system under study. Two graphene family monolayers separated by a distance d and subjected to externally applied electric (E_z) and magnetic (B_z) fields, and a circulary polarized laser (Λ); (b) Low-energy band structure of graphene family materials around a given Dirac point. For a non-zero magnetic field, the quantized Landau levels (red circles) are built on top of the Dirac cones.

5.2.2 Interplay between photo-induced phase transitions and quantum Hall physics in the Casimir effect

In this subsection we investigate the presence of topological phase transitions and the quantum Hall effect in the graphene family Casimir interaction [179]. The schematics of the system under study is shown in Fig. 5.4a, where the layers are separated by a distance d and subjected to a circulary polarized laser field Λ , and out-of-plane static and uniform electric (E_z) and magnetic (B_z) fields. We first give a brief overview on the graphene family magneto-optical response. Then, we show our main results on the zero-temperature Casimir interaction, discussing its distance dependence and long-distance behaviour in the phase space. Thermal effects on the Casimir energy will also be discussed, but in the next subsection.

The conductivity components for graphene family materials are well known and can

be cast as [202],

$$\sigma_{xx} = \sigma_{yy} = \frac{iE_B^2\sigma_0}{\pi} \sum_{\eta,s} \sum_{n,m} \frac{f_m - f_n}{\varepsilon_n - \varepsilon_m} \times \frac{(A_m^+ A_n^-)^2 \delta_{|n|,|m|-\tilde{\eta}} + (A_m^- A_n^+)^2 \delta_{|n|,|m|+\tilde{\eta}}}{\varepsilon_m - \varepsilon_n + i\hbar(\xi + \Gamma)}, \quad (5.12)$$

$$\sigma_{xy} = -\sigma_{yx} = -\frac{E_B^2\sigma_0}{\pi} \sum_{\eta,s} \sum_{n,m} \eta \frac{f_m - f_n}{\varepsilon_n - \varepsilon_m} \times \frac{(A_m^+ A_n^-)^2 \delta_{|n|,|m|-\tilde{\eta}} - (A_m^- A_n^+)^2 \delta_{|n|,|m|+\tilde{\eta}}}{\varepsilon_m - \varepsilon_n + i\hbar(\xi + \Gamma)}. \quad (5.13)$$

Here, $\varepsilon_n = \text{sgn}(n)\sqrt{|n|E_B^2 + (\Delta_s^\eta)^2}$ for $n \neq 0$ and $\varepsilon_0 = -\tilde{\eta}\Delta_s^\eta$ are the Landau levels of the system, with $\tilde{\eta} = \text{sgn}(eB)\eta$, and $E_B = \sqrt{2v_F^2\hbar|eB_z|}$. Also, $A_n^\pm = \sqrt{|\varepsilon_n| \pm \text{sgn}(n)\Delta_s^\eta/2|\varepsilon_n|}$ for $n \neq 0$, $A_0^\pm = (1 \mp \tilde{\eta})/2$, f_n denotes the Fermi Dirac distribution, and Γ is the dissipation rate. The Landau energy levels are illustrated in Fig. 5.4b for a single Dirac cone. For $k_B T = \hbar\Gamma = 0$, one can show that the DC Hall conductivity presents clear signatures of topology and quantum Hall effect. It is given by $\sigma_{xy} = 2\sigma_0(C_{\text{ph}} + C_{\text{QH}})/\pi$, where C_{ph} is the Chern number associated with photo-induced topology, and C_{QH} is the Chern number associated with the quantum Hall effect, namely [202]

$$C_{\text{ph}} = -\frac{1}{2} \sum_{\eta,s} \theta(|\mu| - |\varepsilon_1|) \eta \text{sgn}(\Delta_s^\eta + \tilde{\eta}\mu), \quad (5.14)$$

$$C_{\text{QH}} = -\text{sgn}(eB\mu) \sum_{\eta,s} \theta(|\mu| - \varepsilon_1) (N_s^\eta + 1/2), \quad (5.15)$$

with N_s^η being the number of filled Landau levels per Dirac cone.

In all subsequent discussions, we shall always normalize the Casimir energy between graphene family materials by the zero-temperature neutral graphene/graphene Casimir interaction given by Eq. (5.1). In the long distance regime, the Casimir energy is determined by the DC Hall conductivity and is given by

$$\frac{E^{(0)}}{E_g} = -\frac{4\alpha}{\pi} (C_{1,\text{ph}} + C_{1,\text{QH}})(C_{2,\text{ph}} + C_{2,\text{QH}}). \quad (5.16)$$

Once again, $E^{(0)}$ has the same distance dependence as E_g , therefore a negative (positive) normalized energy implies a repulsive (attractive) force. For two identical layers in the same non-trivial topological phase the Casimir force is repulsive and proportional to the

square of the full Chern number ($C = C_{\text{ph}} + C_{\text{QH}}$) characterizing the corresponding phase of the materials. However, the Casimir force is attractive if the materials are in different topological phases, which in this configuration could be achieved by doping the materials at different levels (in contrast to the case where the magnetic field is absent). We mention that the interplay between photo-induced topology and quantum Hall physics requires $E_B \sim \lambda_{SO}$, which can be accessed in the graphene family for magnetic fields less than or of the order of a few teslas.

Let's also briefly discuss the corrections to Eq. (5.16). When one layer is in a trivial topological phase ($C = 0$), which can be achieved for external fields such that $C_{\text{ph}} = -C_{\text{QH}}$ or $C_{\text{ph}} = C_{\text{QH}} = 0$ (the latter only being possible if $|\mu| < \varepsilon_1$ for every Dirac cone), the first contribution to the Casimir energy arises from the longitudinal conductivity. In the situation where $C_1 = C_2 = 0$, the reflection matrices are given by $\mathbb{R}_{sp} = \mathbb{R}_{ps} \approx 0$, $\mathbb{R}_{ss} \approx -\frac{2\pi\sigma'_{xx}\xi^2}{c^2k_z}$, and $\mathbb{R}_{pp} \approx 2\pi\sigma'_{xx}k_z$, where $\sigma'_{ij} = \partial\sigma_{ij}/\partial\xi|_{\xi \rightarrow 0}$, hence

$$\frac{E^{(0)}}{E_g} \approx \frac{144\pi}{5\alpha d^2} \sigma'_{1,xx} \sigma'_{2,xx}. \quad (5.17)$$

In the above formula, it is important to notice that, since the conductivity is proportional to the fine structure constant, E/E_g is linear in α , such as the case where $C_1, C_2 \neq 0$. However, the normalized energy goes with $1/d^2$, decaying much faster with the distance. If only $C_1 = 0$ but $C_2 \neq 0$ (for instance, by considering monolayers of two different graphene family materials), we must also consider the terms proportional to $\sigma_{2,xy}^2$ inside the reflection matrices in order to obtain the first non zero contribution. By doing that, we obtain

$$\frac{E^{(0)}}{E_g} \approx \frac{8\alpha}{d} \sigma'_{1,xx} C_2^2. \quad (5.18)$$

This time, the normalized energy is proportional to α^2/d , which is also much smaller than the situation where the Chern numbers are finite. In summary, the message from the previous equations is that if C_1 or C_2 vanish, the long distance Casimir force is attractive, smaller in magnitude, and decreases faster with the distance than the case of

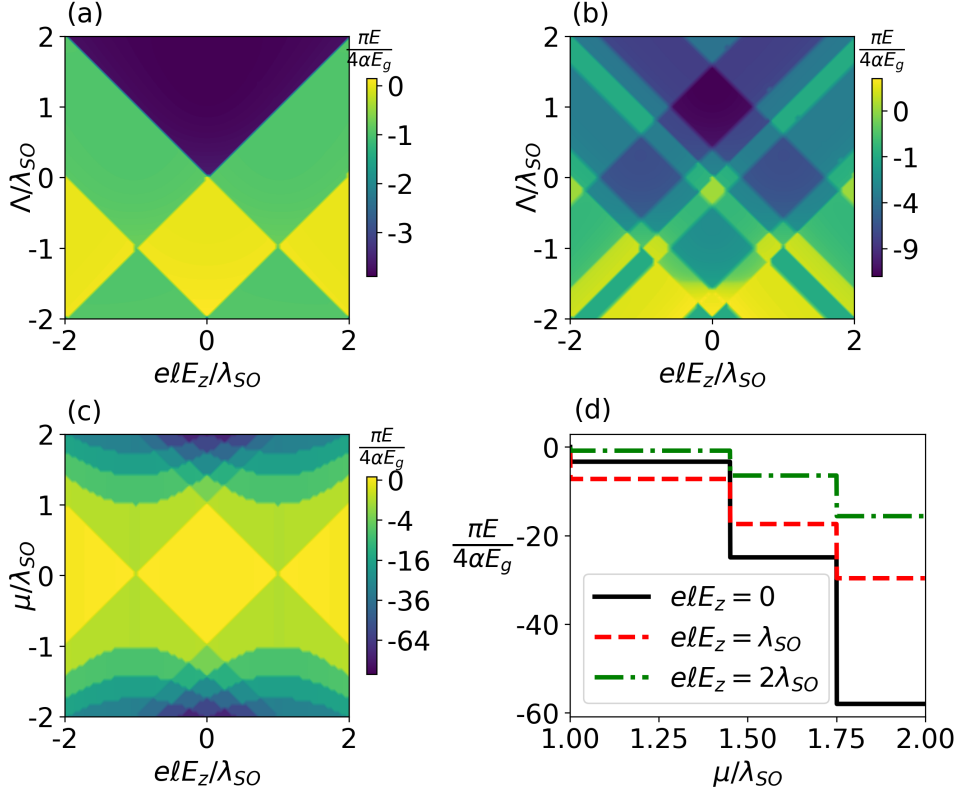


Figure 5.5: Casimir energy in the (E_z, Λ) plane for (a) $\mu = \lambda_{SO}$ and $E_B = 1.2\lambda_{SO}$ and (b) $E_B = 0.8\lambda_{SO}$. (c) Normalized Casimir energy in the (E_z, μ) plane for $\Lambda = 0$ and $E_B = \lambda_{SO}$. (d) Normalized Casimir energy as a function of the chemical potential for $\Lambda = 0$. In all plots the distance between the plates is given by $d\lambda_{SO}/\hbar c = 10$ and the dissipation is set to zero.

non-trivial topological states. Therefore, Eq. (5.16) is the dominant approximation to the Casimir energy in the long distance regime, in contrast to what we get in the absence of a magnetic field, where the Casimir force near the boundaries of the phase diagram is attractive and much higher than far from them [175].

In Fig. 5.5a we plot the Casimir energy for two identical layers separated by $d\lambda_{SO}/\hbar c = 10$ in the (E_z, Λ) plane for $\mu_1 = \mu_2 = \lambda_{SO}$ (denoted by μ) and $E_B = 1.2\lambda_{SO}$. In all regions where $C \neq 0$ the normalized Casimir energy is negative and approximately given by Eq. (5.16), presenting clear signatures of topology. When $C = 0$, the right-hand side of eq. (5.16) vanishes, but we get a small attractive force between the plates, which arises from further expansions of the reflection matrices in the Lifshitz equation. Since $|\mu| < \varepsilon_1$ for

every cone (which is achieved in our plot with the stronger condition $|\mu| < E_B$), we have $C_{\text{QH}} = 0$, implying that we are only able to probe the photo-induced topology. This feature has its roots in the quantum anomaly of the zeroth Landau level [203], which has a twice smaller degeneracy and its energy does not depend on the magnetic field. As a consequence, the Chern number depends only on $\Delta_s^\eta[\Lambda] + \tilde{\eta}\mu = \Delta_s^\eta[\Lambda + \text{sgn}(eB)\mu]$, and thus changing the chemical potential induces the same effect in the phase diagram as modifying the circularly polarized laser intensity. Furthermore, the diagram is also symmetric with respect to $E_z = 0$ and antisymmetric with respect to $\Lambda = -\text{sgn}(eB)\mu$. In the situation where $\mu = 0$, the Chern number is given by $C = -\sum_{\eta,s} \eta \text{sgn}(\Delta_s^\eta)/2$, being the same as in the case without the magnetic field [173]. For $|\mu| > E_B$, the first Landau level may be occupied in a given cone depending on the values of E_z and Λ , resulting in $C_{\text{QH}} \neq 0$ and a wealth of quantum Hall topological phases (Fig. 5.5b). Fig 5.5c is a plot of the normalized Casimir energy in the (E_z, μ) space for $\Lambda = 0$. The shape of the diagram in the region $|\mu| < E_B$ resembles Fig. 5.5a due to the similar role played by μ and Λ under this condition. This shows that the chemical potential can be used as a substitute of the circularly polarized laser field to probe the photo-induced topological features of the Casimir effect. Furthermore, the chemical potential presents an advantage over the laser field since it does not cause an increase of the system's temperature. For highly doped materials ($|\mu| > E_B$), the quantum Hall effect dominates the Casimir interaction and hyperbola-like curves define the boundaries between different topological phases. In Fig 5.5d we display the normalized Casimir energy as a function of the chemical potential. When μ crosses one of the Landau levels in a single Dirac cone from below the Casimir interaction increases, becoming more repulsive. This same behaviour is found in the graphene-graphene interaction in the presence of an external magnetic field [169], as presented in Fig 5.1b. However, here the position and height of the quantum Hall jumps can be tuned with an externally applied electric field, which can move the energy levels upwards or downwards.

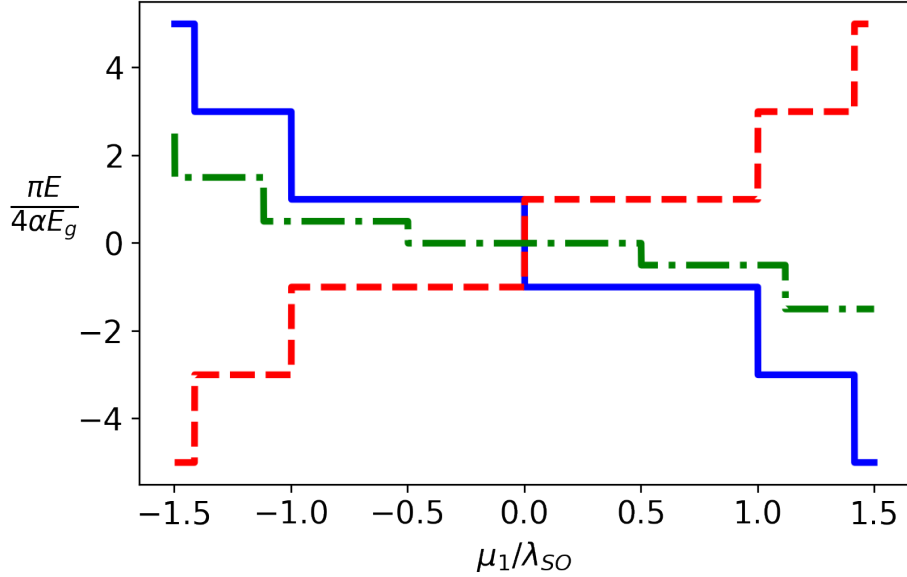


Figure 5.6: Casimir energy as a function of the chemical potential of a single monolayer for $\{e\ell E_z, \mu_2\}/\lambda_{SO} = \{(1,0.5), (1,-0.5), (1.5,0.5)\}$ (solid blue, dashed red, and dash-dotted green, respectively) and $E_B = \lambda_{SO}$. For all curves, the distance between the plates is long enough so that Eq. (5.16) is valid and $\Lambda, \Gamma = 0$.

In Fig. 5.6 we plot the long distance Casimir energy for two identical layers as a function of the chemical potential μ_1 of one of the plates. In this situation, the Chern numbers of the monolayers do not always coincide, which opens up the possibility of changing the attractive or repulsive character of the quantized Casimir force. The sign of the force can be tuned by properly choosing μ_1 , while its magnitude could also be dynamically tailored by modifying E_z and μ_2 . We emphasize that this fine control of the Casimir interaction is only possible due to the energy level quantization arising from the introduction of a magnetic field. As pointed in the previous subsection, without this agent switching the sign of the dispersive Casimir force from repulsion to attraction breaks its quantized behaviour. We also comment that for $|\mu_1| > E_B$ and $|\mu_2| < E_B$ the Casimir force is a full mix of photo-induced topology and quantum Hall physics since $C_1 = C_{1,\text{QH}}$ and $C_2 = C_{2,\text{ph}}$.

The accuracy of the long distance approximation is not the same in all regions of

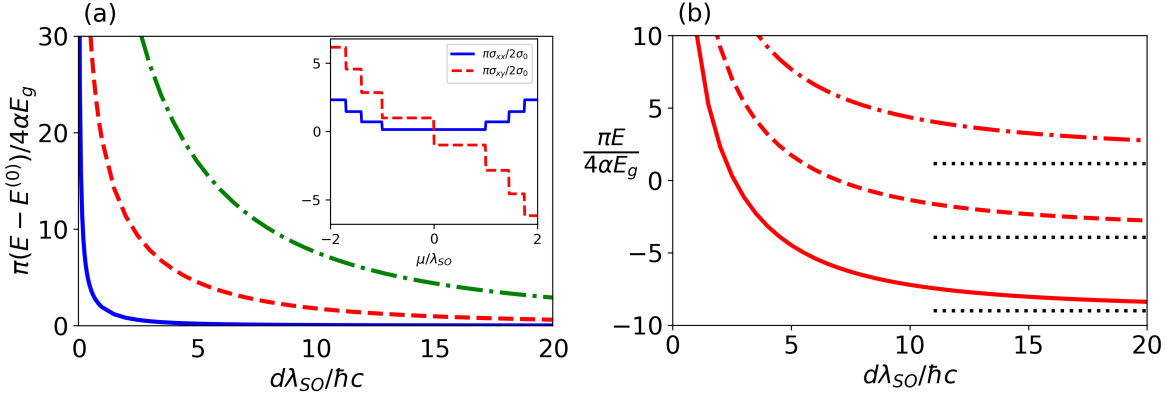


Figure 5.7: (a) Long distance approximated expression given by Eq. (5.16) subtracted from the Casimir energy as a function of distance. The chosen parameters are $\Lambda = 0$, $\Gamma = 0$, $e\ell E_z = \lambda_{SO}$, and $\mu = \{0.5, 1.25, 1.5\}\lambda_{SO}$ (solid blue, dashed red, and dash-dotted green lines, respectively). The inset shows the longitudinal and Hall conductivity at frequency $\hbar\xi = 0.01\lambda_{SO}$ as a function of the chemical potential. (b). Casimir energy for $\Lambda = 0$, $e\ell E_z = \lambda_{SO}$, $\mu = 1.25\lambda_{SO}$, and $\hbar\Gamma = \{0, 0.01, 0.02\}\lambda_{SO}$ (solid, dashed, and dash-dotted lines, respectively) as a function of distance. The gray dotted lines are the approximated solutions in the long distance regime, given by the sum of Eqs. (5.16) and (5.19).

the phase space. In fact, if we look at the upper and bottom portions of the phase diagram in Fig 5.5c and compare it to the numerical values obtained from Eq. (5.16), it becomes evident that this approximation is not as good as it is for smaller values of μ . In Fig. 5.7a we plot the difference between the exact Casimir energy, obtained by full numerical integration of the Lifshitz formula, and the approximated solution in the long distance limit for different values of μ . All curves tend to zero for large distances, but it is evident that the Casimir energy converges faster to its asymptotic expression for smaller values of the chemical potential. The reason for this discrepancy is due to the fact that the asymptotic solution is obtained by neglecting the contribution arising from the longitudinal conductivity. However, as we can see in the inset of Fig. 5.7a, for larger values of μ the longitudinal conductivity increases near $i\xi = 0$ and, in this case, needs to be accounted in the low frequency expansion for the distances considered. Fig. 5.7b shows how the Casimir interaction is affected by introducing a non-negligible dissipation $\Gamma \neq 0$ in the monolayers. In this situation, the Casimir energy becomes less repulsive, and

can be attractive for sufficiently high values of dissipation. To understand this from an analytical point of view, we once again expand the integrand of Eq. (4.25) for small values of ξ . Since both σ_{xx} and σ_{xy} are non zero at $\xi = 0$, the dominant contribution of the Casimir energy comes from the DC conductivity tensor. For sufficiently small values of the dissipation ($\hbar\Gamma \ll \lambda_{SO}$), we have $\sigma_{xx}(0) \approx \sigma'_{xx}(0)\Gamma$ and $\sigma_{xy}(0) \approx \frac{\alpha c}{2\pi}C$, where we took advantage of the similar role played by Γ and ξ in Eqs. (5.12) and (5.13). By retaining only the longitudinal conductivity and expanding the reflection matrices for small ξ we obtain

$$\frac{\Delta E^{(0)}}{E_g} = \frac{4\alpha\Gamma}{c} \frac{\log(\sigma'_{1,xx}/\sigma'_{2,xx})}{(\sigma'_{2,xx})^{-1} - (\sigma'_{1,xx})^{-1}}. \quad (5.19)$$

For two identical layers, this expression simplifies to $\Delta E^{(0)}/E_g = 4\alpha\Gamma\sigma'_{xx}/c$. The dotted gray lines in Fig. 5.7b are given by the sum of Eq. (5.16) with Eq. (5.19), and have a good agreement with the non approximated results (red curves).

5.2.3 Thermal effects in the graphene family Casimir forces

Now we consider thermal effects in the Casimir energy between two parallel graphene family layers. For finite temperatures the Casimir interaction energy follows from Eq. (4.25) by considering the temperature dependent conductivity of the monolayers. The finite-temperature Casimir energy exhibits a rather distinct behaviour depending on whether or not we neglect dissipation in the materials. We first consider two identical dissipationless layers ($\Gamma = 0$). In Fig. 5.8a we show the normalized Casimir energy in the long distance regime as a function of temperature for different values of μ . For sufficiently small temperatures ($k_B T/\lambda_{SO} \lesssim 10^{-2}$), the Casimir energy is well described by the zero-temperature limit (left inset). As we increase the temperature, however, the Casimir force becomes more repulsive (right inset), reaching values two orders of magnitude greater than those at zero temperature in the region $k_B T/\lambda_{SO} \in [0.1, 1]$ (below, near, and above room temperature for silicene, germanene, and stanene, respectively). This contrasts with the results found in the absence of a magnetic field, where even

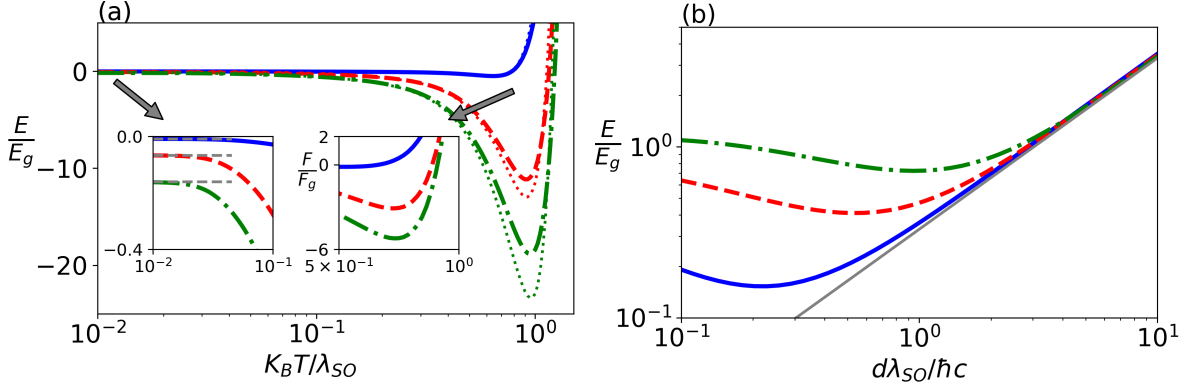


Figure 5.8: (a) Dissipationless Casimir energy as a function of temperature for a separation distance of $d\lambda_{SO}/\hbar c = 10$. The dotted lines correspond to the approximated value of the $n = 0$ Matsubara frequency contribution presented in Eq. (5.20). The left inset is a zoom of the plot, showing that each curve goes to its correspondent zero-temperature limit (dashed gray lines). The right inset shows the Casimir force in the region where it becomes attractive. (b) Casimir energy as a function of distance for $k_B T = 10^{-3}\lambda_{SO}$ and $\hbar\Gamma = 0.01\lambda_{SO}$. The gray line corresponds to the $n = 0$ Matsubara contribution (Eq. (5.21)). In both plots, $\Lambda = 0$, $e\ell E_z = \lambda_{SO}$, and $\mu = \{0.5, 1.25, 1.5\}\lambda_{SO}$ (solid blue, dashed red, and dash-dotted green lines, respectively).

for smaller values of temperature ($k_B T / \lambda_{SO} \simeq 10^{-3}$, which corresponds to $T \sim 2, 3K$ for plumbene and smaller for other materials) the force is attractive, reaching the zero-temperature limit only for $k_B T / \lambda_{SO} \simeq 10^{-4}$. [175]. For $k_B T \simeq \lambda_{SO}$, the strength of the interaction reaches a maximum value and then rapidly becomes attractive due to thermal transitions between different Landau levels.

This behaviour of the finite-temperature Casimir energy can be described analytically by considering only the contribution of the $n = 0$ Matsubara frequency in Eq. (4.25). Since for $\Gamma = 0$ and small values of ξ we have $\sigma_{xx} = \sigma'_{xx}(0)\xi$, we get a contribution from both the longitudinal and Hall conductivities. By expanding the reflection matrices in ξ , taking the limit $\xi \rightarrow 0$, and keeping the lowest order contribution in α , we get $\mathbb{R}_{sp} = \mathbb{R}_{ps} \approx 2\pi\sigma_{xy}/c$, $\mathbb{R}_{ss} \approx 0$, and $\mathbb{R}_{pp} \approx 2\pi\sigma'_{xx}k_{||}$ (notice that the conductivities depend on temperature). Hence, we obtain

$$\frac{E}{E_g} = -\frac{16\pi^2\sigma_{1,xy}\sigma_{2,xy}}{\hbar c\alpha}k_B T d + \frac{12\pi^2\sigma'_{1,xx}\sigma'_{2,xx}}{\hbar c\alpha}\frac{k_B T}{d}. \quad (5.20)$$

The dotted lines in Fig. 5.8a were obtained from the previous equation, and we note that there is a good agreement between this approximation and the numerical calculations. Eq. (5.20) highlights that the repulsive Casimir interaction arises from the Hall conductivity, which holds information about topology and quantum Hall physics, while the attractive counterpart is due to the longitudinal conductivity. In contrast to the zero-temperature limit, the positive and negative terms of eq. (5.20) have different distance scaling laws. As a consequence, the Casimir force becomes attractive at a temperature slightly lower than that associated to the situation $E = 0$, as shown in the right inset of Fig. 5.8a. In the regime where $k_B T \ll \lambda_{SO}$ but T is high enough so that keeping only the $n = 0$ term is still a good approximation, we can discard the second term of eq. (5.20) and assume that $\sigma_{i,xy} \approx 2\sigma_0 C_i / \pi$, which leads to $E/E_g = -(4\alpha c k_B T d / \hbar) C_1 C_2$. This shows that applying a magnetic field on the materials increases the robustness of the topological features arising in the Casimir force, which are now present even at high temperatures ($k_B T \sim 0.1\lambda_{SO}$). For instance, let us consider two stanene monolayers at $T = 300K$ and separated by a distance $d = 20\mu\text{m}$. By evaluating the Casimir force per unit area for $\Lambda = 0$ and $e\ell E_z = \lambda_{SO}$, we obtain $F \approx 0.1\text{nPa}$ (repulsive) at $\mu = 1.25\lambda_{SO}$ and $F \approx 0.2\text{nPa}$ (repulsive) at $\mu = 1.5\lambda_{SO}$, while the zero-temperature graphene-graphene Casimir pressure is given by $F_g \approx 0.05\text{nPa}$ (attractive). On the left inset of Fig. 5.8a, the slope of each curve is proportional to the square of its corresponding Chern number, being higher for larger values of μ .

The picture is not the same if we add dissipation to the system. In this case, $\sigma_{xx}(0) \neq 0$ and the limit $\xi \rightarrow 0$ of the reflection matrices yields $\mathbb{R}_{ss} = \mathbb{R}_{sp} = \mathbb{R}_{ps} = 0$ and $\mathbb{R}_{pp} = 1$. Hence, regardless of the topological phase of the materials, the $n = 0$ contribution to the Casimir energy is given by

$$\frac{E}{E_g} = \frac{2\zeta(3)}{\hbar c \alpha} k_B T d, \quad (5.21)$$

which is exactly the same result as in the absence of a magnetic field. Note that there is no dependence on the conductivities and, more importantly, the result is the same for

any non-zero value of Γ . Fig. 5.8b shows that, in this situation, even for temperatures of $k_B T / \lambda_{SO} = 10^{-3}$ the Casimir force is always attractive, as the case when $B = 0$. Hence, in order to see repulsion in a dissipative system one has to decrease the temperature to the sub-kelvin regime, which poses a serious difficult in measuring the Casimir force.

This discrepancy between the results obtained for a dissipationless and a dissipative system is no coincidence. Having a finite dissipation, even if arbitrarily small, is fundamentally different from having no dissipation. For metallic materials, this is equivalent to describe the system using a plasma ($\Gamma = 0$) or a Drude ($\Gamma \neq 0$) model, which leads to significantly different final results [204]. In principle, the Drude model is the most straightforward approach for taking into account the relaxation properties of conduction electrons, and should be applicable in the quasistatic limit (which corresponds to the high temperature regime of the Casimir force). In fact, a few experiments [205, 206] show that the Casimir force is consistent with the calculations using this model. However, the plasma model approach, which usually appears in the literature in infrared optical phenomena, was shown to best describe the Casimir force between metals in most of the experiments [207–210]. Which model is the correct one to use when calculating the Casimir force is an open problem that still awaits its ending chapters. Here we provide a full description of the Casimir interaction between dissipative and dissipationless graphene family topological insulators and comment that the Drude versus plasma discussion can be extended to non-metallic systems. We emphasize that this extremely different behaviour of the dissipationless Casimir force in the graphene family does not show up when $B = 0$, where it was shown that both models differ only by a factor 2 (as the case of metallic plates) [175]. Hence, the addition of a magnetic field to the problem allows one not only to avoid difficulties concerning temperature but also to clearly discriminate both descriptions and investigate fundamental questions in physics.

Chapter 6

Conclusions and final remarks

In the last few decades we have witnessed an exponential progress in materials science. On top of that, two-dimensional matter and their related nanostructures have emerged as a key asset to build new disruptive devices, with applications in the fields of nano-optics, nanophotonics, plasmonics, biology and the tech industry as a whole. In this thesis we presented novel approaches for enhancing, screening and tuning quantum light-matter interactions in low-dimensional materials. In particular, we achieved fine control of the two-quanta spontaneous emission phenomenon and the Casimir effect using state-of-the-art material platforms such as atomically thin nanostructures and two-dimensional Dirac materials. We believe this thesis will find its importance not only as contributions for the scientific community, but also as a reference for study and development of new ideas.

The first part of the thesis (Chapters I, II, and III) addressed one- and two-quanta spontaneous emission. After the brief review of one-quantum SE presented in chapter I, in chapter II we discussed the main aspects of its second order counterpart, namely, the TQSE. Despite being orders of magnitude slower than typical one-photon SE in free-space, the TQSE phenomenon can be relevant when the former is forbidden by selection rules, such as the case of hydrogenic atoms in the $2s$ state. Furthermore, it is possible to significantly enhance this phenomenon by using materials that present a high near-field local density of states. This motivated us to develop a first principle understanding of the TQSE Purcell effect and search for material systems that enable competition between

the first and second order decay paths. We started by deriving an alternative formula for computing the TQSE rate of an excited emitter near a surface of arbitrary shape, which was written in terms of the electromagnetic field modes [67]. With this formula, we analyzed the TQSE of an emitter between two parallel perfect mirrors and showed that the TQSE cannot be completely suppressed for $s \rightarrow s$ transitions. This is to be contrasted to the suppression of the one-photon SE that may occur for an atom between two parallel perfect mirrors if the atom is appropriately prepared [36]. We also explicitly demonstrated the equivalence of our formula with the Green's tensor equation for calculating the TQSE rate usually found in the literature. Then we compared both methods and showed that, although the TQSE rate calculation by using the Green's function method is straightforward, the field modes approach has the advantage of clarifying the physics of the problem and provides an easier way to compute the angular distribution of the emitted photons. Another important equation that we demonstrated relates the TQSE to the one-quantum SE, and allows us to compute the spectral density function in any situation where the one-quantum SE rate is known. We applied this formalism for an emitter near a homogeneous semi-infinite dielectric medium and verified that an interesting behaviour of the TQSE spectral distribution shows up near the resonance frequencies of the dielectric. This result motivated us to try to control the two-quanta emitted frequencies with active materials, discussed in chapter III.

Chapter III is dedicated to the study of TQSE in low-dimensional plasmonic materials. We started by analyzing the one- and two-quanta SE of an atom close to an infinite graphene sheet. In this section we discussed how graphene tunable plasmons may increase both phenomena and allow them to compete with each other, opening the road to possible experimental realization of entangled plasmons generation. We investigated the spontaneous emission of two plasmons by single quantum emitters in one-dimensional carbon nanomaterials such as SWCNTs and GCWs [119]. We have shown that SWCNTs increase the emission rate by more than twelve orders of magnitude compared to the rate

in free-space and with average lifetimes of the order of a few dozens of nanoseconds. Such impressive enhancements are possible due to the large confinement of the fundamental plasmonic mode in a broad frequency range. In order to extend our investigation to wider plasmonic nanowires, we considered the case of a dielectric cylinder coated with a graphene monolayer. We demonstrated the role of different plasmonic modes supported by the nanowire in TPSE, which results in a rich, tunable broadband spectrum of emission, with sharp resonances at the plasmons' minimum excitation frequencies. We concluded that GCWs enable bespoke tailoring of the spectral lineshapes while significantly minimizing the emitter's lifetime. We also developed a comprehensive study of the dominant two-quanta decay channels in finite-sized ultra-thin plasmonic nanostructures with arbitrary shape and material properties [134]. We unravelled an intricate interplay between Fano and Lorentzian lineshapes in single, dual, and even multiband emission. Giant emission of photon-pairs are enabled by localized surface plasmons, which naturally leak into photonic modes and result in radiative TQSE several orders of magnitude larger than via ordinary SPPs. We also studied the particular case of an emitter close to a graphene nanodisk, where we achieved more efficient photon production rates through two-quanta transitions than via standard one-photon processes. We believe this work highlights the potential that TQSE and two-dimensional plasmonic nanostructures have for photonics.

The second part of the thesis is concerned with the Casimir effect. In chapter IV we presented a brief introduction to the subject, giving a special attention to the Lifshitz formula that is the basis for all calculations performed in the next chapter. In chapter V we discussed the Casimir physics of two-dimensional materials. We first presented the results for the graphene-graphene Casimir interaction, which is $\sim \alpha$ times smaller than the standard Casimir force between perfect metals (with α being the fine structure constant). We demonstrated that force quantization and sign changes can be achieved by applying a magnetic field to the system, results which are consequences of the quantum Hall effect in graphene. Then we discussed the Casimir effect between graphene family materials, which

are two-dimensional topological insulators that present many topological phase transitions under the influence of a circularly polarized laser and an external electrostatic field. Interestingly, their zero-temperature retarded Casimir force is repulsive and proportional to the product of their corresponding Chern numbers. Next, we presented a complete study of the Casimir effect between graphene family materials when we apply another external agent, namely, a uniform magnetic field [179]. In this case, the Casimir interaction can be made attractive or repulsive by properly doping the materials. This remarkable possibility of switching the sign of the Casimir force in the flatland is exclusively due to the interplay between photo-induced topological phase transitions and quantum Hall physics brought by the presence of a magnetic field. Furthermore, the chemical potential can be used as a substitute of the circularly polarized laser field, which may be very useful to avoid heating the materials due to photo-absorption. Finally, we analyzed the thermal effects on the Casimir energy, which proved to be significantly different from previous studies using the graphene family materials. We have shown that a dissipative model imply a rather trivial high temperature Casimir force, where no topological physics is present. However, the picture is very different for dissipationless systems. In this case, we found repulsive forces of the order of the zero-temperature graphene-graphene interaction, even at room temperatures, and the topological features are not completely lost. Since some experiments show that the Casimir force is in agreement with the plasma (dissipationless) model and others with the Drude (dissipative) model, we emphasize the importance of our findings in the dissipationless limit. Indeed, a huge difference between both situations suggests a good way of testing which model correctly describes the Casimir interaction in the extended graphene family.

Bibliography

- [1] D. B. Hough and L. R. White, “The calculation of hamaker constants from liftshitz theory with applications to wetting phenomena,” *Advances in Colloid and Interface Science*, vol. 14, no. 1, pp. 3–41, 1980. xi, xii, 18, 37
- [2] P. W. Milonni, *The quantum vacuum: an introduction to quantum electrodynamics*. Academic press, 2013. xix, 3, 5, 6, 75, 77
- [3] D. P. Craig and T. Thirunamachandran, *Molecular quantum electrodynamics: an introduction to radiation-molecule interactions*. Courier Corporation, 1984. xix, 20, 21, 22
- [4] M. E. Peskin, *An introduction to quantum field theory*. CRC Press, 2018. xix
- [5] A. Einstein, “Zur quantentheorie der strahlung,” *Phys. Z.*, vol. 18, pp. 121–128, 1917. xix
- [6] P. A. Dirac, “The quantum theory of the emission and absorption of radiation,” *Proc. R. Soc. Lond. A*, vol. 114, no. 767, pp. 243–265, 1927. xix, 1, 4
- [7] P. Milonni, “Why spontaneous emission?,” *American Journal of Physics*, vol. 52, no. 4, pp. 340–343, 1984. xx, 1
- [8] E. Purcell, “Em purcell, phys. rev. 69, 681 (1946).,” *Phys. Rev.*, vol. 69, p. 681, 1946. xx, 1

- [9] S. A. Maier, *Plasmonics: fundamentals and applications*. Springer Science & Business Media, 2007. xx, 38
- [10] N. Rivera, I. Kaminer, B. Zhen, J. D. Joannopoulos, and M. Soljačić, “Shrinking light to allow forbidden transitions on the atomic scale,” *Science*, vol. 353, no. 6296, pp. 263–269, 2016. xx, 18, 22, 33, 39, 45, 50, 57, 64, 74
- [11] M. Göppert-Mayer, “Über elementarakte mit zwei quantensprüngen,” *Annalen der Physik*, vol. 401, no. 3, pp. 273–294, 1931. xx, 21
- [12] G. Breit and E. Teller, “Metastability of hydrogen and helium levels.,” *The Astrophysical Journal*, vol. 91, p. 215, 1940. xx, 22, 23
- [13] A. Hayat, P. Ginzburg, and M. Orenstein, “Observation of two-photon emission from semiconductors,” *Nature photonics*, vol. 2, no. 4, p. 238, 2008. xxi, 26, 70
- [14] N. Rivera, G. Rosolen, J. D. Joannopoulos, I. Kaminer, and M. Soljačić, “Making two-photon processes dominate one-photon processes using mid-ir phonon polarizations,” *Proceedings of the National Academy of Sciences*, p. 201713538, 2017. xxi, 29, 35, 39, 57, 74
- [15] H. B. Casimir, “On the attraction between two perfectly conducting plates,” in *Proc. Kon. Ned. Akad. Wet.*, vol. 51, p. 793, 1948. xxi, 75
- [16] M. Bordag, G. L. Klimchitskaya, U. Mohideen, and V. M. Mostepanenko, *Advances in the Casimir effect*, vol. 145. OUP Oxford, 2009. xxi, 76
- [17] C. Farina, “The casimir effect: some aspects,” *Brazilian journal of physics*, vol. 36, no. 4A, pp. 1137–1149, 2006. xxi, 75, 77
- [18] V. Parsegian and A. Van der Waals Forces, “Handbook for biologists, chemists, engineers, and physicists,” *Cambridge University Pr*, 2006. xxi

- [19] J. Israelachvili, “Intermolecular and surface forces: revised third edition. new york city,” 2011. xxi
- [20] R. A. DiStasio, O. A. von Lilienfeld, and A. Tkatchenko, “Collective many-body van der waals interactions in molecular systems,” *Proceedings of the National Academy of Sciences*, vol. 109, no. 37, pp. 14791–14795, 2012. xxi
- [21] K. Autumn, Y. A. Liang, S. T. Hsieh, W. Zesch, W. P. Chan, T. W. Kenny, R. Fearing, and R. J. Full, “Adhesive force of a single gecko foot-hair,” *Nature*, vol. 405, no. 6787, pp. 681–685, 2000. xxi, 76
- [22] K. Autumn, M. Sitti, Y. A. Liang, A. M. Peattie, W. R. Hansen, S. Sponberg, T. W. Kenny, R. Fearing, J. N. Israelachvili, and R. J. Full, “Evidence for van der waals adhesion in gecko setae,” *Proceedings of the National Academy of Sciences*, vol. 99, no. 19, pp. 12252–12256, 2002. xxi, 76
- [23] M. Sedighi and G. Palasantzas, “Influence of low optical frequencies on actuation dynamics of microelectromechanical systems via casimir forces,” *Journal of Applied Physics*, vol. 117, no. 14, p. 144901, 2015. xxi
- [24] J. R. Rodrigues, A. Gusso, F. S. Rosa, and V. R. Almeida, “Rigorous analysis of casimir and van der waals forces on a silicon nano-optomechanical device actuated by optical forces,” *Nanoscale*, vol. 10, no. 8, pp. 3945–3952, 2018. xxi
- [25] G. Klimchitskaya, U. Mohideen, and V. Mostepanenko, “The casimir force between real materials: Experiment and theory,” *Reviews of Modern Physics*, vol. 81, no. 4, p. 1827, 2009. xxi, 76
- [26] L. Woods, D. A. R. Dalvit, A. Tkatchenko, P. Rodriguez-Lopez, A. W. Rodriguez, and R. Podgornik, “Materials perspective on casimir and van der waals interactions,” *Reviews of Modern Physics*, vol. 88, no. 4, p. 045003, 2016. xxi, 75, 79

- [27] A. W. Rodriguez, F. Capasso, and S. G. Johnson, “The casimir effect in microstructured geometries,” *Nature photonics*, vol. 5, no. 4, pp. 211–221, 2011. xxi
- [28] L. Tang, M. Wang, C. Ng, M. Nikolic, C. T. Chan, A. W. Rodriguez, and H. B. Chan, “Measurement of non-monotonic casimir forces between silicon nanostructures,” *Nature Photonics*, vol. 11, no. 2, pp. 97–101, 2017. xxi
- [29] A. G. Grushin and A. Cortijo, “Tunable casimir repulsion with three-dimensional topological insulators,” *Physical review letters*, vol. 106, no. 2, p. 020403, 2011. xxi
- [30] P. Rodriguez-Lopez and A. G. Grushin, “Repulsive casimir effect with chern insulators,” *Physical review letters*, vol. 112, no. 5, p. 056804, 2014. xxi
- [31] J. Ma, Q. Zhao, and Y. Meng, “Magnetically controllable casimir force based on a superparamagnetic metamaterial,” *Physical Review B*, vol. 89, no. 7, p. 075421, 2014. xxii
- [32] K. Drexhage, “Beeinflussung der fluoreszenz eins europiumchelates durch einen spiegel,” *Ber. Bunsenges. Phys. Chem.*, vol. 70, p. 1179, 1966. 1
- [33] K. Drexhage, “Influence of a dielectric interface on fluorescence decay time,” *Journal of luminescence*, vol. 1, pp. 693–701, 1970. 1
- [34] K. H. Drexhage, “Monomolecular layers and light,” *Scientific American*, vol. 222, no. 3, pp. 108–120, 1970. 1
- [35] D. Kleppner, “Inhibited spontaneous emission,” *Physical Review Letters*, vol. 47, no. 4, p. 233, 1981. 2
- [36] R. G. Hulet, E. S. Hilfer, and D. Kleppner, “Inhibited spontaneous emission by a rydberg atom,” *Physical review letters*, vol. 55, no. 20, p. 2137, 1985. 2, 11, 109

- [37] S. Haroche, “Les houches, session liii (1990), fondamental systems in quantum optics, éd j. dalibard, jm raimond et j. zinn-justin,” 1992. 2, 7, 62
- [38] S. Haroche and J.-M. Raimond, *Exploring the quantum: atoms, cavities, and photons*. Oxford university press, 2006. 2, 11
- [39] S. Haroche, “Nobel lecture: Controlling photons in a box and exploring the quantum to classical boundary,” *Reviews of Modern Physics*, vol. 85, no. 3, p. 1083, 2013. 2
- [40] P. Lodahl, S. Mahmoodian, and S. Stobbe, “Interfacing single photons and single quantum dots with photonic nanostructures,” *Reviews of Modern Physics*, vol. 87, pp. 347–400, may 2015. 2
- [41] Z.-Y. Li, L.-L. Lin, and Z.-Q. Zhang, “Spontaneous emission from photonic crystals: full vectorial calculations,” *Physical review letters*, vol. 84, no. 19, p. 4341, 2000. 2
- [42] J. R. Lakowicz, “Radiative decay engineering 5: metal-enhanced fluorescence and plasmon emission,” *Analytical biochemistry*, vol. 337, no. 2, pp. 171–194, 2005. 2
- [43] Y. V. Vladimirova, V. V. Klimov, V. M. Pastukhov, and V. N. Zadkov, “Modification of two-level-atom resonance fluorescence near a plasmonic nanostructure,” *Physical Review A*, vol. 85, no. 5, p. 053408, 2012. 2
- [44] W. Kort-Kamp, F. Rosa, F. Pinheiro, and C. Farina, “Spontaneous emission in the presence of a spherical plasmonic metamaterial,” *Physical Review A*, vol. 87, no. 2, p. 023837, 2013. 2
- [45] G. Song, J.-p. Xu, and Y.-p. Yang, “Spontaneous emission of a two-level system near the interface of topological insulators,” *EPL (Europhysics Letters)*, vol. 105, no. 6, p. 64001, 2014. 2
- [46] M. Pelton, “Modified spontaneous emission in nanophotonic structures,” *Nature Photonics*, vol. 9, no. 7, p. 427, 2015. 2

- [47] W. Kort-Kamp, B. Amorim, G. Bastos, F. A. Pinheiro, F. Rosa, N. Peres, and C. Farina, “Active magneto-optical control of spontaneous emission in graphene,” *Physical Review B*, vol. 92, no. 20, p. 205415, 2015. 2, 39
- [48] R. Chikkaraddy, B. De Nijs, F. Benz, S. J. Barrow, O. A. Scherman, E. Rosta, A. Demetriadou, P. Fox, O. Hess, and J. J. Baumberg, “Single-molecule strong coupling at room temperature in plasmonic nanocavities,” *Nature*, vol. 535, no. 7610, pp. 127–130, 2016. 2
- [49] S. Sanders, A. May, A. Alabastri, and A. Manjavacas, “Extraordinary enhancement of quadrupolar transitions using nanostructured graphene,” *ACS Photonics*, 2018. 2, 39
- [50] D. Szilard, W. Kort-Kamp, F. Rosa, F. Pinheiro, and C. Farina, “Hysteresis in the spontaneous emission induced by VO_2 phase change,” *JOSA B*, vol. 36, no. 4, pp. C46–C51, 2019. 2
- [51] P. Gonçalves, T. Christensen, N. Rivera, A.-P. Jauho, N. A. Mortensen, and M. Soljačić, “Plasmon–emitter interactions at the nanoscale,” *Nature communications*, vol. 11, no. 1, pp. 1–13, 2020. 2
- [52] C. Cohen-Tannoudji, J. Dupont-Roc, and G. Grynberg, *Photons and atoms: introduction to quantum electrodynamics*. Wiley Online Library, 1989. 2, 3
- [53] C. Cohen-Tannoudji, J. Dupont-Roc, G. Grynberg, and P. Thickstun, *Atom-photon interactions: basic processes and applications*. Wiley Online Library, 1992. 2
- [54] A. A. Gilbert Grynberg and C. Fabre, *Introduction to quantum optics: from the semi-classical approach to quantized light*. Cambridge, UK: Cambridge University Press, 2010. 2, 11

- [55] J. J. Sakurai and J. J. Napolitano, *Modern quantum mechanics*. Pearson Higher Ed, 2014. 3, 20
- [56] M. Le Bellac, *Quantum physics*. Cambridge University Press, 2011. 4
- [57] P. W. Milonni and P. Knight, “Spontaneous emission between mirrors,” *Optics Communications*, vol. 9, no. 2, pp. 119–122, 1973. 6
- [58] J. D. Joannopoulos, S. G. Johnson, J. N. Winn, and R. D. Meade, *Photonic crystals*. Princeton university press, 2011. 11
- [59] E. Yablonovitch, “Inhibited spontaneous emission in solid-state physics and electronics,” *Physical review letters*, vol. 58, no. 20, p. 2059, 1987. 11
- [60] S. M. Barnett and P. M. Radmore, *Methods in theoretical quantum optics*, vol. 15. Oxford University Press, 2002. 11
- [61] S. Scheel and S. Y. Buhmann, “Macroscopic qed-concepts and applications,” *arXiv preprint arXiv:0902.3586*, 2009. 12
- [62] L. Novotny and B. Hecht, *Principles of nano-optics*. Cambridge university press, 2012. 12, 14, 15, 16, 17, 32, 34, 62
- [63] S. Y. Buhmann, “Macroscopic quantum electrodynamics,” in *Dispersion Forces I*, pp. 45–107, Springer, 2012. 12, 35
- [64] A. Zangwill, *Modern electrodynamics*. Cambridge University Press, 2013. 13, 16, 17, 76, 89
- [65] L. Mandel and E. Wolf, *Optical coherence and quantum optics*. Cambridge university press, 1995. 15

- [66] S.-A. Biehs, P. Ben-Abdallah, F. S. Rosa, K. Joulain, and J.-J. Greffet, “Nanoscale heat flux between nanoporous materials,” *Optics express*, vol. 19, no. 105, pp. A1088–A1103, 2011. 16
- [67] Y. Muniz, F. da Rosa, C. Farina, D. Szilard, and W. Kort-Kamp, “Quantum two-photon emission in a photonic cavity,” *Physical Review A*, vol. 100, no. 2, p. 023818, 2019. 20, 26, 109
- [68] M. Lipeles, R. Novick, and N. Tolk, “Direct detection of two-photon emission from the metastable state of singly ionized helium,” *Physical Review Letters*, vol. 15, no. 17, p. 690, 1965. 23
- [69] J. Shapiro and G. Breit, “Metastability of 2 s states of hydrogenic atoms,” *Physical Review*, vol. 113, no. 1, p. 179, 1959. 23
- [70] H. Krüger and A. Oed, “Measurement of the decay-probability of metastable hydrogen by two-photon emission,” *Physics Letters A*, vol. 54, no. 3, pp. 251–253, 1975. 23
- [71] V. Florescu, S. Patrascu, and O. Stoican, “Systematic study of 1s-ns and 1s-nd two-photon transitions of hydrogenlike atoms,” *Physical Review A*, vol. 36, no. 5, p. 2155, 1987. 23, 31
- [72] D. R. Bates and B. Bederson, *Advances in atomic and molecular physics*, vol. 20, vol. 20. Academic Press, 1985. 24
- [73] B. H. Bransden, C. J. Joachain, and T. J. Plivier, *Physics of atoms and molecules*. Pearson Education India, 2003. 24
- [74] J. Chluba and R. Sunyaev, “Two-photon transitions in hydrogen and cosmological recombination,” *Astronomy & Astrophysics*, vol. 480, no. 3, pp. 629–645, 2008. 25

- [75] Y. Bennett and I. Freund, “Two-photon x-ray emission from inner-shell transitions,” *Physical Review Letters*, vol. 49, no. 8, p. 539, 1982. 26
- [76] Y. B. Bennett and I. Freund, “Two-photon inner-shell transitions in molybdenum,” *Physical Review A*, vol. 30, no. 1, p. 299, 1984. 26
- [77] A. Hayat, P. Ginzburg, and M. Orenstein, “High-rate entanglement source via two-photon emission from semiconductor quantum wells,” *Physical Review B*, vol. 76, no. 3, p. 035339, 2007. 26, 39
- [78] H. M. Van Driel, “Semiconductor optics: On the path to entanglement,” *Nature Photonics*, vol. 2, no. 4, p. 212, 2008. 26
- [79] Y. Ota, S. Iwamoto, N. Kumagai, and Y. Arakawa, “Spontaneous two-photon emission from a single quantum dot,” *Physical review letters*, vol. 107, no. 23, p. 233602, 2011. 26, 70
- [80] A. N. Poddubny, P. Ginzburg, P. A. Belov, A. V. Zayats, and Y. S. Kivshar, “Tailoring and enhancing spontaneous two-photon emission using resonant plasmonic nanostructures,” *Physical Review A*, vol. 86, no. 3, p. 033826, 2012. 33, 71
- [81] A. Sommerfeld, “Ueber die fortpflanzung elektrodynamischer wellen längs eines drahtes,” *Annalen der Physik*, vol. 303, no. 2, pp. 233–290, 1899. 38
- [82] J. Zenneck, “Über die fortpflanzung ebener elektromagnetischer wellen längs einer ebenen leiterfläche und ihre beziehung zur drahtlosen telegraphie,” *Annalen der Physik*, vol. 328, no. 10, pp. 846–866, 1907. 38
- [83] H. Barlow and A. Cullen, “Surface waves,” *Proceedings of the IEE-Part III: Radio and Communication Engineering*, vol. 100, no. 68, pp. 329–341, 1953. 38
- [84] R. Warnock, “On the propagation of electrodynamic waves along a wire by a. sommerfeld,” *Electromagnetics*, vol. 39, no. 5, pp. 281–324, 2019. 38

- [85] M. A. Green and S. Pillai, "Harnessing plasmonics for solar cells," *Nature photonics*, vol. 6, no. 3, pp. 130–132, 2012. 38
- [86] P. Mandal and S. Sharma, "Progress in plasmonic solar cell efficiency improvement: A status review," *Renewable and sustainable energy reviews*, vol. 65, pp. 537–552, 2016. 38
- [87] K. A. Willets, A. J. Wilson, V. Sundaresan, and P. B. Joshi, "Super-resolution imaging and plasmonics," *Chemical reviews*, vol. 117, no. 11, pp. 7538–7582, 2017. 38
- [88] A. Bezryadina, J. Zhao, Y. Xia, X. Zhang, and Z. Liu, "High spatiotemporal resolution imaging with localized plasmonic structured illumination microscopy," *ACS nano*, vol. 12, no. 8, pp. 8248–8254, 2018. 38
- [89] Y. He, S. Su, T. Xu, Y. Zhong, J. A. Zapien, J. Li, C. Fan, and S.-T. Lee, "Silicon nanowires-based highly-efficient sers-active platform for ultrasensitive dna detection," *Nano Today*, vol. 6, no. 2, pp. 122–130, 2011. 38
- [90] A. G. Brolo, "Plasmonics for future biosensors," *Nature Photonics*, vol. 6, no. 11, pp. 709–713, 2012. 38
- [91] F. Peng, Y. Su, Y. Zhong, C. Fan, S.-T. Lee, and Y. He, "Silicon nanomaterials platform for bioimaging, biosensing, and cancer therapy," *Accounts of chemical research*, vol. 47, no. 2, pp. 612–623, 2014. 38
- [92] P. D. Howes, R. Chandrawati, and M. M. Stevens, "Colloidal nanoparticles as advanced biological sensors," *Science*, vol. 346, no. 6205, p. 1247390, 2014. 38
- [93] K. J. Russell, T.-L. Liu, S. Cui, and E. L. Hu, "Large spontaneous emission enhancement in plasmonic nanocavities," *Nature Photonics*, vol. 6, no. 7, pp. 459–462, 2012. 38

- [94] C. Belacel, B. Habert, F. Bigourdan, F. Marquier, J.-P. Hugonin, S. Michaelis de Vasconcellos, X. Lafosse, L. Coolen, C. Schwob, C. Javaux, *et al.*, “Controlling spontaneous emission with plasmonic optical patch antennas,” *Nano letters*, vol. 13, no. 4, pp. 1516–1521, 2013. 38
- [95] T. B. Hoang, G. M. Akselrod, C. Argyropoulos, J. Huang, D. R. Smith, and M. H. Mikkelsen, “Ultrafast spontaneous emission source using plasmonic nanoantennas,” *Nature communications*, vol. 6, no. 1, pp. 1–7, 2015. 38, 57, 71
- [96] J. J. Baumberg, J. Aizpurua, M. H. Mikkelsen, and D. R. Smith, “Extreme nanophotonics from ultrathin metallic gaps,” *Nature materials*, vol. 18, no. 7, pp. 668–678, 2019. 38
- [97] P. Gonçalves, T. Christensen, N. Rivera, A.-P. Jauho, N. A. Mortensen, and M. Soljačić, “Plasmon–emitter interactions at the nanoscale,” *Nature communications*, vol. 11, no. 1, pp. 1–13, 2020. 39, 57
- [98] L. Dal Negro, Y. Chen, S. Gorsky, and F. Sgrignuoli, “Aperiodic bandgap structures for enhanced quantum two-photon sources,” *JOSA B*, vol. 38, no. 9, pp. C94–C104, 2021. 39
- [99] A. Nevet, N. Berkovitch, A. Hayat, P. Ginzburg, S. Ginzach, O. Sorias, and M. Orenstein, “Plasmonic nanoantennas for broad-band enhancement of two-photon emission from semiconductors,” *Nano letters*, vol. 10, no. 5, pp. 1848–1852, 2010. 39, 71
- [100] A. K. Geim and K. S. Novoselov, “The rise of graphene,” in *Nanoscience and technology: a collection of reviews from nature journals*, pp. 11–19, World Scientific, 2010. 39

- [101] A. N. Grigorenko, M. Polini, and K. Novoselov, “Graphene plasmonics,” *Nature photonics*, vol. 6, no. 11, pp. 749–758, 2012. 39, 41
- [102] F. J. Garcia de Abajo, “Graphene plasmonics: challenges and opportunities,” *Acs Photonics*, vol. 1, no. 3, pp. 135–152, 2014. 39, 46, 47
- [103] F. H. Koppens, D. E. Chang, and F. J. Garcia de Abajo, “Graphene plasmonics: a platform for strong light–matter interactions,” *Nano letters*, vol. 11, no. 8, pp. 3370–3377, 2011. 39
- [104] V. N. Popov, “Carbon nanotubes: properties and application,” *Materials Science and Engineering: R: Reports*, vol. 43, no. 3, pp. 61–102, 2004. 39
- [105] L. Martín-Moreno, F. J. G. de Abajo, and F. J. García-Vidal, “Ultraefficient coupling of a quantum emitter to the tunable guided plasmons of a carbon nanotube,” *Physical review letters*, vol. 115, no. 17, p. 173601, 2015. 39, 46, 48, 52
- [106] R. A. Maniyara, D. Rodrigo, R. Yu, J. Canet-Ferrer, D. S. Ghosh, R. Yongsunthon, D. E. Baker, A. Rezikyan, F. J. García de Abajo, and V. Pruneri, “Tunable plasmons in ultrathin metal films,” *Nature Photonics*, vol. 13, no. 5, pp. 328–333, 2019. 39, 60, 70
- [107] Z. M. Abd El-Fattah, V. Mkhitaryan, J. Brede, L. Fernández, C. Li, Q. Guo, A. Ghosh, A. R. Echarri, D. Naveh, F. Xia, *et al.*, “Plasmonics in atomically thin crystalline silver films,” *ACS nano*, vol. 13, no. 7, pp. 7771–7779, 2019. 39, 60, 70
- [108] A. Manjavacas and F. G. De Abajo, “Tunable plasmons in atomically thin gold nanodisks,” *Nature communications*, vol. 5, no. 1, pp. 1–7, 2014. 39, 60
- [109] P. A. D. Gonçalves and N. M. Peres, *An introduction to graphene plasmonics*. World Scientific, 2016. 40, 42

- [110] C. Itzykson and J.-B. Zuber, *Quantum field theory*. Courier Corporation, 2012. 40
- [111] L. Ju, B. Geng, J. Horng, C. Girit, M. Martin, Z. Hao, H. A. Bechtel, X. Liang, A. Zettl, Y. R. Shen, *et al.*, “Graphene plasmonics for tunable terahertz metamaterials,” *Nature nanotechnology*, vol. 6, no. 10, pp. 630–634, 2011. 40
- [112] M. L. Cohen and S. G. Louie, *Fundamentals of condensed matter physics*. Cambridge University Press, 2016. 40
- [113] L. Falkovsky and A. Varlamov, “Space-time dispersion of graphene conductivity,” *The European Physical Journal B*, vol. 56, no. 4, pp. 281–284, 2007. 40
- [114] L. Falkovsky, “Optical properties of graphene,” in *Journal of Physics: conference series*, vol. 129, p. 012004, IOP Publishing, 2008. 40
- [115] T. Stauber, N. Peres, and A. Geim, “Optical conductivity of graphene in the visible region of the spectrum,” *Physical Review B*, vol. 78, no. 8, p. 085432, 2008. 40
- [116] V. Gusynin, S. Sharapov, and J. Carbotte, “On the universal ac optical background in graphene,” *New Journal of Physics*, vol. 11, no. 9, p. 095013, 2009. 40
- [117] T. Stauber, N. Peres, and A. C. Neto, “Conductivity of suspended and non-suspended graphene at finite gate voltage,” *Physical Review B*, vol. 78, no. 8, p. 085418, 2008. 41
- [118] A. C. Neto, F. Guinea, N. M. Peres, K. S. Novoselov, and A. K. Geim, “The electronic properties of graphene,” *Reviews of modern physics*, vol. 81, no. 1, p. 109, 2009. 41
- [119] Y. Muniz, P. Abrantes, L. Martín-Moreno, F. Pinheiro, C. Farina, and W. Kort-Kamp, “Entangled two-plasmon generation in carbon nanotubes and graphene-coated wires,” *Physical Review B*, vol. 105, no. 16, p. 165412, 2022. 45, 57, 109

- [120] A. Moradi, “Optical properties of two-walled carbon nanotubes: quasi-static approximation,” *The European Physical Journal Plus*, vol. 135, no. 7, pp. 1–14, 2020. 46
- [121] H. Li, S. Li, H. Liu, and X. Wang, “Analysis of electromagnetic scattering from plasmonic inclusions beyond the quasi-static approximation and applications,” *ESAIM: Mathematical Modelling and Numerical Analysis*, vol. 53, no. 4, pp. 1351–1371, 2019. 46
- [122] I. S. Gradshteyn and I. M. Ryzhik, *Table of integrals, series, and products*. Academic press, 2014. 48, 137
- [123] G. W. Ford and W. H. Weber, “Electromagnetic interactions of molecules with metal surfaces,” *Physics Reports*, vol. 113, no. 4, pp. 195–287, 1984. 48
- [124] M. Riso, M. Cuevas, and R. A. Depine, “Tunable plasmonic enhancement of light scattering and absorption in graphene-coated subwavelength wires,” *Journal of Optics*, vol. 17, no. 7, p. 075001, 2015. 49
- [125] Y. V. Bludov, A. Ferreira, N. M. Peres, and M. I. Vasilevskiy, “A primer on surface plasmon-polaritons in graphene,” *International Journal of Modern Physics B*, vol. 27, no. 10, p. 1341001, 2013. 49
- [126] E. Ganesh, “Single walled and multi walled carbon nanotube structure, synthesis and applications,” *International Journal of Innovative Technology and Exploring Engineering*, vol. 2, no. 4, pp. 311–320, 2013. 49
- [127] J. Ma, J. N. Wang, and X. X. Wang, “Large-diameter and water-dispersible single-walled carbon nanotubes: synthesis, characterization and applications,” *Journal of Materials Chemistry*, vol. 19, no. 19, pp. 3033–3041, 2009. 49

- [128] K. I. Bolotin, K. J. Sikes, Z. Jiang, M. Klima, G. Fudenberg, J. Hone, P. Kim, and H. Stormer, “Ultrahigh electron mobility in suspended graphene,” *Solid state communications*, vol. 146, no. 9-10, pp. 351–355, 2008. 50
- [129] C. R. Dean, A. F. Young, I. Meric, C. Lee, L. Wang, S. Sorgenfrei, K. Watanabe, T. Taniguchi, P. Kim, K. L. Shepard, *et al.*, “Boron nitride substrates for high-quality graphene electronics,” *Nature nanotechnology*, vol. 5, no. 10, pp. 722–726, 2010. 50
- [130] X. Zeng, Z. Liao, M. Al-Amri, and M. S. Zubairy, “Controllable waveguide via dielectric cylinder covered with graphene: Tunable entanglement,” *EPL (Europhysics Letters)*, vol. 115, no. 1, p. 14002, 2016. 52, 53
- [131] X. He, Z.-b. Liu, D. Wang, M. Yang, T. Y. Hu, and J.-G. Tian, “Saturable absorber based on graphene-covered-microfiber,” *IEEE Photonics Technology Letters*, vol. 25, no. 14, pp. 1392–1394, 2013. 53
- [132] B. Zhu, G. Ren, Y. Gao, Y. Yang, Y. Lian, and S. Jian, “Graphene-coated tapered nanowire infrared probe: a comparison with metal-coated probes,” *Optics Express*, vol. 22, no. 20, pp. 24096–24103, 2014. 53
- [133] A. Rose, T. B. Hoang, F. McGuire, J. J. Mock, C. Ciraci, D. R. Smith, and M. H. Mikkelsen, “Control of radiative processes using tunable plasmonic nanopatch antennas,” *Nano letters*, vol. 14, no. 8, pp. 4797–4802, 2014. 57
- [134] Y. Muniz, A. Manjavacas, C. Farina, D. A. R. Dalvit, and W. Kort-Kamp, “Two-photon spontaneous emission in atomically thin plasmonic nanostructures,” *Physical Review Letters*, vol. 125, no. 3, p. 033601, 2020. 57, 58, 110
- [135] F. J. G. de Abajo and A. Manjavacas, “Plasmonics in atomically thin materials,” *Faraday discussions*, vol. 178, pp. 87–107, 2015. 57, 58

- [136] R. Yu, J. D. Cox, J. Saavedra, and F. J. García de Abajo, “Analytical modeling of graphene plasmons,” *ACS Photonics*, vol. 4, no. 12, pp. 3106–3114, 2017. 58
- [137] A. L. Fetter, “Magnetoplasmons in a two-dimensional electron fluid: Disk geometry,” *Physical Review B*, vol. 33, no. 8, p. 5221, 1986. 60, 136, 138
- [138] V. D. Karanikolas, C. A. Marocico, and A. L. Bradley, “Tunable and long-range energy transfer efficiency through a graphene nanodisk,” *Physical Review B*, vol. 93, no. 3, p. 035426, 2016. 60
- [139] M. Tamagnone, A. Ambrosio, K. Chaudhary, L. A. Jauregui, P. Kim, W. L. Wilson, and F. Capasso, “Ultra-confined mid-infrared resonant phonon polaritons in van der waals nanostructures,” *Science advances*, vol. 4, no. 6, p. eaat7189, 2018. 61
- [140] P. Bharadwaj and L. Novotny, “Spectral dependence of single molecule fluorescence enhancement,” *Optics Express*, vol. 15, no. 21, pp. 14266–14274, 2007. 63
- [141] A. E. Miroshnichenko, S. Flach, and Y. S. Kivshar, “Fano resonances in nanoscale structures,” *Reviews of Modern Physics*, vol. 82, no. 3, p. 2257, 2010. 67
- [142] B. Luk'yanchuk, N. I. Zheludev, S. A. Maier, N. J. Halas, P. Nordlander, H. Giessen, and C. T. Chong, “The fano resonance in plasmonic nanostructures and metamaterials,” *Nature materials*, vol. 9, no. 9, pp. 707–715, 2010. 67
- [143] M. F. Limonov, M. V. Rybin, A. N. Poddubny, and Y. S. Kivshar, “Fano resonances in photonics,” *Nature Photonics*, vol. 11, no. 9, pp. 543–554, 2017. 67
- [144] H. Wang, H. Hu, T.-H. Chung, J. Qin, X. Yang, J.-P. Li, R.-Z. Liu, H.-S. Zhong, Y.-M. He, X. Ding, *et al.*, “On-demand semiconductor source of entangled photons which simultaneously has high fidelity, efficiency, and indistinguishability,” *Physical review letters*, vol. 122, no. 11, p. 113602, 2019. 70

- [145] P. Lodahl, A. Floris van Driel, I. S. Nikolaev, A. Irman, K. Overgaag, D. Vanmaekelbergh, and W. L. Vos, “Controlling the dynamics of spontaneous emission from quantum dots by photonic crystals,” *Nature*, vol. 430, no. 7000, pp. 654–657, 2004. 71
- [146] F. London, “Zur theorie und systematik der molekularkräfte,” *Zeitschrift für Physik*, vol. 63, no. 3-4, pp. 245–279, 1930. 75
- [147] H. Casimir and D. Polder, “The influence of retardation on the london-van der waals forces,” *Physical Review*, vol. 73, no. 4, p. 360, 1948. 75
- [148] K. A. Milton, *The Casimir effect: physical manifestations of zero-point energy*. World Scientific, 2001. 75
- [149] H. Casimir, “Sur les forces van der waals-london,” *Journal de Chimie Physique*, vol. 46, pp. 407–410, 1949. 75
- [150] E. Lifshitz *et al.*, “Sov. phys. jetc,” *Sov. Phys. JETP*, vol. 2, pp. 73–83, 1956. 76
- [151] E. M. Lifshitz, M. Hamermesh, *et al.*, “The theory of molecular attractive forces between solids,” in *Perspectives in Theoretical Physics*, pp. 329–349, Elsevier, 1992. 76
- [152] M. Bordag, U. Mohideen, and V. M. Mostepanenko, “New developments in the casimir effect,” *Physics reports*, vol. 353, no. 1-3, pp. 1–205, 2001. 76
- [153] D. Dalvit, P. Milonni, D. Roberts, and F. da Rosa, eds., *Casimir Physics*. Springer Berlin Heidelberg, 2011. 76
- [154] M. J. Sparnaay, “Measurements of attractive forces between flat plates,” *Physica*, vol. 24, no. 6-10, pp. 751–764, 1958. 76

- [155] S. K. Lamoreaux, “Demonstration of the casimir force in the 0.6 to 6 μ m range,” *Physical Review Letters*, vol. 78, no. 1, p. 5, 1997. 76, 79
- [156] S. Lamoreaux, “Erratum: Demonstration of the casimir force in the 0.6 to 6 μ m range [phys. rev. lett. 78, 5 (1997)],” *Physical Review Letters*, vol. 81, no. 24, p. 5475, 1998. 76
- [157] R. Decca, D. López, E. Fischbach, G. Klimchitskaya, D. Krause, and V. M. Mostepanenko, “Precise comparison of theory and new experiment for the casimir force leads to stronger constraints on thermal quantum effects and long-range interactions,” *Annals of Physics*, vol. 318, no. 1, pp. 37–80, 2005. 76
- [158] A. Lambrecht, P. A. M. Neto, and S. Reynaud, “The casimir effect within scattering theory,” *New Journal of physics*, vol. 8, no. 10, p. 243, 2006. 77
- [159] G. B. Arfken and H. J. Weber, *Mathematical methods for physicists*. AAPT, 1999.
- 78
- [160] M. Hartmann, G.-L. Ingold, and P. A. M. Neto, “Plasma versus drude modeling of the casimir force: beyond the proximity force approximation,” *Physical review letters*, vol. 119, no. 4, p. 043901, 2017. 79
- [161] G.-L. Ingold and A. Lambrecht, “Casimir effect from a scattering approach,” *American Journal of Physics*, vol. 83, no. 2, pp. 156–162, 2015. 79
- [162] F. Intravaia and A. Lambrecht, “Surface plasmon modes and the casimir energy,” *Physical review letters*, vol. 94, no. 11, p. 110404, 2005. 82
- [163] F. Intravaia, C. Henkel, and A. Lambrecht, “Role of surface plasmons in the casimir effect,” *Physical Review A*, vol. 76, no. 3, p. 033820, 2007. 82
- [164] D. Drosdoff and L. M. Woods, “Casimir forces and graphene sheets,” *Physical Review B*, vol. 82, no. 15, p. 155459, 2010. 86, 87, 88

- [165] V. V. Gobre and A. Tkatchenko, “Scaling laws for van der waals interactions in nanostructured materials,” *Nature communications*, vol. 4, no. 1, pp. 1–6, 2013. 86
- [166] A. Banishev, H. Wen, J. Xu, R. Kawakami, G. Klimchitskaya, V. Mostepanenko, and U. Mohideen, “Measuring the casimir force gradient from graphene on a sio 2 substrate,” *Physical Review B*, vol. 87, no. 20, p. 205433, 2013. 86
- [167] S. Tsoi, P. Dev, A. L. Friedman, R. Stine, J. T. Robinson, T. L. Reinecke, and P. E. Sheehan, “van der waals screening by single-layer graphene and molybdenum disulfide,” *Acs Nano*, vol. 8, no. 12, pp. 12410–12417, 2014. 86
- [168] M. Goerbig, “Electronic properties of graphene in a strong magnetic field,” *Reviews of Modern Physics*, vol. 83, no. 4, p. 1193, 2011. 86, 89
- [169] W.-K. Tse and A. MacDonald, “Quantized casimir force,” *Physical review letters*, vol. 109, no. 23, p. 236806, 2012. 86, 90, 91, 92, 101
- [170] T. Cysne, W. Kort-Kamp, D. Oliver, F. Pinheiro, F. Rosa, and C. Farina, “Tuning the casimir-polder interaction via magneto-optical effects in graphene,” *Physical Review A*, vol. 90, no. 5, p. 052511, 2014. 86
- [171] M. Z. Hasan and C. L. Kane, “Colloquium: topological insulators,” *Reviews of modern physics*, vol. 82, no. 4, p. 3045, 2010. 86
- [172] Y. Ando, “Topological insulator materials,” *Journal of the Physical Society of Japan*, vol. 82, no. 10, p. 102001, 2013. 86
- [173] M. Ezawa, “Monolayer topological insulators: silicene, germanene, and stanene,” *Journal of the Physical Society of Japan*, vol. 84, no. 12, p. 121003, 2015. 86, 92, 93, 94, 101
- [174] W. J. d. M. Kort-Kamp, “Topological phase transitions in the photonic spin hall effect,” *Physical review letters*, vol. 119, no. 14, p. 147401, 2017. 86, 93

- [175] P. Rodriguez-Lopez, W. J. Kort-Kamp, D. A. Dalvit, and L. M. Woods, “Casimir force phase transitions in the graphene family,” *Nature communications*, vol. 8, no. 1, pp. 1–9, 2017. 87, 95, 100, 105, 107
- [176] A. K. Geim and I. V. Grigorieva, “Van der waals heterostructures,” *Nature*, vol. 499, no. 7459, pp. 419–425, 2013. 87
- [177] Y.-C. Lin, N. Lu, N. Perea-Lopez, J. Li, Z. Lin, X. Peng, C. H. Lee, C. Sun, L. Calderin, P. N. Browning, *et al.*, “Direct synthesis of van der waals solids,” *Acs Nano*, vol. 8, no. 4, pp. 3715–3723, 2014. 87
- [178] N. B. Le, T. D. Huan, and L. M. Woods, “Interlayer interactions in van der waals heterostructures: electron and phonon properties,” *ACS applied materials & interfaces*, vol. 8, no. 9, pp. 6286–6292, 2016. 87
- [179] Y. Muniz, C. Farina, and W. Kort-Kamp, “Casimir forces in the flatland: Interplay between photoinduced phase transitions and quantum hall physics,” *Physical Review Research*, vol. 3, no. 2, p. 023061, 2021. 87, 97, 111
- [180] J. F. Dobson, A. White, and A. Rubio, “Asymptotics of the dispersion interaction: analytic benchmarks for van der waals energy functionals,” *Physical review letters*, vol. 96, no. 7, p. 073201, 2006. 87
- [181] G. Gómez-Santos, “Thermal van der waals interaction between graphene layers,” *Physical Review B*, vol. 80, no. 24, p. 245424, 2009. 87, 88
- [182] J. Sarabadani, A. Naji, R. Asgari, and R. Podgornik, “Many-body effects in the van der waals–casimir interaction between graphene layers,” *Physical Review B*, vol. 84, no. 15, p. 155407, 2011. 87

- [183] G. Klimchitskaya, V. Mostepanenko, and B. E. Sernelius, “Two approaches for describing the casimir interaction in graphene: Density-density correlation function versus polarization tensor,” *Physical Review B*, vol. 89, no. 12, p. 125407, 2014. 87
- [184] M. Bordag, I. Fialkovskiy, and D. Vassilevich, “Enhanced casimir effect for doped graphene,” *Physical Review B*, vol. 93, no. 7, p. 075414, 2016. 87, 88
- [185] K. S. Novoselov, A. K. Geim, S. V. Morozov, D. Jiang, M. I. Katsnelson, I. Grigorieva, S. Dubonos, and a. Firsov, “Two-dimensional gas of massless dirac fermions in graphene,” *nature*, vol. 438, no. 7065, pp. 197–200, 2005. 89
- [186] Y. Zhang, Y.-W. Tan, H. L. Stormer, and P. Kim, “Experimental observation of the quantum hall effect and berry’s phase in graphene,” *nature*, vol. 438, no. 7065, pp. 201–204, 2005. 89
- [187] V. Gusynin and S. Sharapov, “Transport of dirac quasiparticles in graphene: Hall and optical conductivities,” *Physical Review B*, vol. 73, no. 24, p. 245411, 2006. 89, 90
- [188] V. Gusynin, S. Sharapov, and J. Carbotte, “Magneto-optical conductivity in graphene,” *Journal of Physics: Condensed Matter*, vol. 19, no. 2, p. 026222, 2006. 89
- [189] W.-K. Tse and A. MacDonald, “Magneto-optical and magnetoelectric effects of topological insulators in quantizing magnetic fields,” *Physical Review B*, vol. 82, no. 16, p. 161104, 2010. 90
- [190] W.-K. Tse and A. MacDonald, “Magneto-optical faraday and kerr effects in topological insulator films and in other layered quantized hall systems,” *Physical Review B*, vol. 84, no. 20, p. 205327, 2011. 90

- [191] P. Vogt, P. De Padova, C. Quaresima, J. Avila, E. Frantzeskakis, M. C. Asensio, A. Resta, B. Ealet, and G. Le Lay, “Silicene: compelling experimental evidence for graphenelike two-dimensional silicon,” *Physical review letters*, vol. 108, no. 15, p. 155501, 2012. 92
- [192] M. Dávila, L. Xian, S. Cahangirov, A. Rubio, and G. Le Lay, “Germanene: a novel two-dimensional germanium allotrope akin to graphene and silicene,” *New Journal of Physics*, vol. 16, no. 9, p. 095002, 2014. 92
- [193] F.-f. Zhu, W.-j. Chen, Y. Xu, C.-l. Gao, D.-d. Guan, C.-h. Liu, D. Qian, S.-C. Zhang, and J.-f. Jia, “Epitaxial growth of two-dimensional stanene,” *Nature materials*, vol. 14, no. 10, pp. 1020–1025, 2015. 92
- [194] A. Castellanos-Gomez, “Why all the fuss about 2d semiconductors?,” *Nature Photonics*, vol. 10, no. 4, pp. 202–204, 2016. 92
- [195] Z. Ni, Q. Liu, K. Tang, J. Zheng, J. Zhou, R. Qin, Z. Gao, D. Yu, and J. Lu, “Tunable bandgap in silicene and germanene,” *Nano letters*, vol. 12, no. 1, pp. 113–118, 2012. 93
- [196] L. Stille, C. J. Tabert, and E. J. Nicol, “Optical signatures of the tunable band gap and valley-spin coupling in silicene,” *Physical Review B*, vol. 86, no. 19, p. 195405, 2012. 93
- [197] M. Ezawa, “Photoinduced topological phase transition and a single dirac-cone state in silicene,” *Physical review letters*, vol. 110, no. 2, p. 026603, 2013. 93
- [198] M. B. Farias, W. J. Kort-Kamp, and D. A. Dalvit, “Quantum friction in two-dimensional topological materials,” *Physical Review B*, vol. 97, no. 16, p. 161407, 2018. 93

- [199] P. Abrantes, T. P. Cysne, D. Szilard, F. Rosa, F. Pinheiro, and C. Farina, “Probing topological phase transitions via quantum reflection in the graphene family materials,” *Physical Review B*, vol. 104, no. 7, p. 075409, 2021. 93
- [200] Y. A. Bychkov and E. I. Rashba, “Oscillatory effects and the magnetic susceptibility of carriers in inversion layers,” *Journal of physics C: Solid state physics*, vol. 17, no. 33, p. 6039, 1984. 94
- [201] A. Manchon, H. C. Koo, J. Nitta, S. Frolov, and R. Duine, “New perspectives for rashba spin-orbit coupling,” *Nature materials*, vol. 14, no. 9, pp. 871–882, 2015. 94
- [202] P. Ledwith, W. J. d. M. Kort-Kamp, and D. A. R. Dalvit, “Topological phase transitions and quantum hall effect in the graphene family,” *Physical Review B*, vol. 97, no. 16, p. 165426, 2018. 98
- [203] J. Karch, P. Olbrich, M. Schmalzbauer, C. Zoth, C. Brinsteiner, M. Fehrenbacher, U. Wurstbauer, M. Glazov, S. Tarasenko, E. Ivchenko, *et al.*, “Dynamic hall effect driven by circularly polarized light in a graphene layer,” *Physical review letters*, vol. 105, no. 22, p. 227402, 2010. 101
- [204] G. Klimchitskaya and V. Mostepanenko, “Casimir free energy of metallic films: Discriminating between drude and plasma model approaches,” *Physical Review A*, vol. 92, no. 4, p. 042109, 2015. 107
- [205] D. Garcia-Sanchez, K. Y. Fong, H. Bhaskaran, S. Lamoreaux, and H. X. Tang, “Casimir force and in situ surface potential measurements on nanomembranes,” *Physical review letters*, vol. 109, no. 2, p. 027202, 2012. 107
- [206] A. Sushkov, W. Kim, D. Dalvit, and S. Lamoreaux, “Observation of the thermal casimir force,” *Nature Physics*, vol. 7, no. 3, pp. 230–233, 2011. 107

- [207] R. Decca, E. Fischbach, G. Klimchitskaya, D. Krause, D. López, and V. Mostepanenko, “Improved tests of extra-dimensional physics and thermal quantum field theory from new casimir force measurements,” *Physical Review D*, vol. 68, no. 11, p. 116003, 2003. 107
- [208] R. Decca, D. López, E. Fischbach, G. Klimchitskaya, D. Krause, and V. Mostepanenko, “Tests of new physics from precise measurements of the casimir pressure between two gold-coated plates,” *Physical Review D*, vol. 75, no. 7, p. 077101, 2007. 107
- [209] A. Banishev, G. Klimchitskaya, V. Mostepanenko, and U. Mohideen, “Casimir interaction between two magnetic metals in comparison with nonmagnetic test bodies,” *Physical Review B*, vol. 88, no. 15, p. 155410, 2013. 107
- [210] G. Bimonte, D. López, and R. S. Decca, “Isoelectronic determination of the thermal casimir force,” *Physical Review B*, vol. 93, no. 18, p. 184434, 2016. 107

Appendix A

Plasmon wave functions of a nanodisk

In this appendix we obtain the PWFs directly from equation (3.30) for the case of a plasmonic nanodisk. The PWFs in polar coordinates can be written as a radial function $R_{ln}(u)$ times an angular function of the form $e^{il\phi}$. We also expand the term $|\mathbf{u} - \mathbf{u}'|^{-1}$ in terms of Bessel functions, namely [137]

$$\frac{1}{|\mathbf{u} - \mathbf{u}'|} = \int_0^\infty dp \sum_{m=-\infty}^{\infty} J_{|m|}(up) J_{|m|}(u'p) e^{im(\phi-\phi')}. \quad (\text{A.1})$$

In this way, equation (3.30) reduces to

$$2\pi \nabla_{\mathbf{u}}^2 \int_0^{1/2} du' u' \int_0^\infty dp J_{|l|}(up) J_{|l|}(u'p) R_{ln}(u') e^{il\phi} = \frac{1}{\eta_{ln}} R_{ln}(u) e^{il\phi}. \quad (\text{A.2})$$

In order to deal with the Laplacian, we write the right-hand side of the previous equation as $\frac{1}{\eta_{ln}} \int_0^{1/2} du' u' R_{ln}(u') \frac{\delta(u'-u)}{u'} e^{il\phi}$ and then recall that the Green's function of the radial part of the Poisson equation in cylindrical coordinates satisfies $\nabla_{\mathbf{u}}^2 G_l(u, u') e^{il\phi} = -\frac{\delta(u'-u)}{u'} e^{il\phi}$. Hence,

$$\int_0^{1/2} du' u' \int_0^\infty dp J_{|l|}(up) J_{|l|}(u'p) R_{ln}(u') = -\frac{1}{2\pi\eta_{ln}} \int_0^{1/2} du' u' R_{ln}(u') G_l(u, u'). \quad (\text{A.3})$$

The radial part of the PWFs can be further expanded as

$$R_{ln}(u) = (2u)^{|l|} \sum_{m'} a_{m'}^{ln} P_m^{(|l|,0)}(1 - 8u^2), \quad (\text{A.4})$$

where $a_m^{ln'}$ are to be determined and $P_m^{(\alpha,\beta)}(x)$ are the Jacobi Polynomials. Multiplying both sides by $(2u)^{|l|+1}P_m^{(|l|,0)}(1-8u^2)$, making the change of variables $x = 2u$, $x' = 2u'$, and $p \rightarrow 2p$, and using the relations [122]

$$\int_0^1 dx x^{|l|+1} P_m^{(|l|,0)}(1-2x^2) J_{|l|}(px) = \frac{J_{|l|+2m+1}(p)}{p}, \quad (\text{A.5})$$

$$\int_0^\infty dp \frac{J_{|l|+2m+1}(p) J_{|l|+2m'+1}(p)}{p^2} = \frac{(-1)^{m-m'+1}}{\pi [4(m-m')^2 - 1] [|l| + m + m' + 1/2] [|l| + m + m' + 3/2]}, \quad (\text{A.6})$$

allows us to immediately solve the left-hand side (LHS) of equation (A.3) once we integrate in x . We have

$$\text{LHS} = \frac{1}{2} \sum_{m'} \mathbb{K}_{mm'}^l a_m^{ln'}, \quad (\text{A.7})$$

where

$$\mathbb{K}_{mm'}^l = \frac{(-1)^{m-m'+1}}{\pi [4(m-m')^2 - 1] [|l| + m + m' + 1/2] [|l| + m + m' + 3/2]}, \quad m, m' = 0, 1, 2, 3\dots \quad (\text{A.8})$$

The right-hand side (RHS) of equation (A.3) can be solved in the same way once we plug the expression for $G_l(u, u')$ and use the orthogonality relation [122]

$$\int_0^1 dx x^{2|l|+1} P_i^{(|l|,0)}(1-2x^2) P_j^{(|l|,0)}(1-2x^2) = \frac{\delta_{ij}}{2(|l| + 2j + 1)}. \quad (\text{A.9})$$

For $l \neq 0$, $G_l(u, u') = \frac{1}{2|l|} [(uu')^{|l|} + (u_</u_>)^{|l|}]$, where $u_> = \max(u, u')$ and $u_< = \min(u, u')$.

Therefore, after integration over x , we obtain

$$\text{RHS} = -\frac{1}{8\pi\eta_{ln}} \sum_{m'} \mathbb{G}_{mm'}^l a_m^{ln}, \quad (\text{A.10})$$

where

$$\begin{aligned} \mathbb{G}_{mm'}^l &= \frac{\delta_{m0}\delta_{m'0}}{8|l|(|l|+1)^2} + \frac{\delta_{mm'}}{4(|l|+2m')(|l|+2m'+1)(|l|+2m'+2)} \\ &+ \frac{\delta_{m+1,m'}}{8(|l|+2m+1)(|l|+2m+2)(|l|+2m+3)} \\ &+ \frac{\delta_{m,m'+1}}{8(|l|+2m'+1)(|l|+2m'+2)(|l|+2m'+3)}, \quad m, m' = 0, 1, 2, 3\dots \end{aligned} \quad (\text{A.11})$$

For $l = 0$, $G_l(x, x') = -\ln(x_>)$ and the calculations are not as straightforward [137]. The result is the same as for $l \neq 0$, but the matrix \mathbb{G}^l does not have the first term ($m, m' \neq 0$) of the RHS of the previous equation. Finally, by combining Eqs. (A.7) and (A.10), we obtain an eigenvalue equation for the vector $\mathbf{a}^{ln} = \{a_m^{ln}\}$,

$$\mathbb{G}^l \mathbf{a}^{ln} = -4\pi\eta_{ln} \mathbb{K}^l \mathbf{a}^{ln}. \quad (\text{A.12})$$

We solved this eigenvalue equation numerically for up to $m, m' = 300$, obtaining satisfactory convergence. The normalization of \mathbf{a}^{ln} is obtained by enforcing Eq. (3.32) to be satisfied, resulting in a normalization factor given by $\sqrt{8/\pi \mathbf{a}^{ln} \mathbb{G}^l \mathbf{a}^{ln}}$.

Finally, several of the results we demonstrated in sections 3.3.1 and 3.3.2 admit simple semi-analytical expressions in the case of the nanodisk. In particular,

$$\mathbf{F}_{ln}(\mathbf{R}_e) = \pi D \nabla_{\mathbf{R}_e} e^{il\phi_e} \sum_m a_m^{ln} \int_0^\infty \frac{dp}{p} e^{-2pz_e/D} J_{|l|} \left(\frac{2r_e p}{D} \right) J_{|l|+2m+1}(p). \quad (\text{A.13})$$

For the case analyzed in the main text of a dipole placed at the symmetry axis of the nanodisk, the integral above can be solved analytically, resulting in

$$\begin{aligned} F_{ln,x}(z_e) &= \pi \delta_{|l|1} \sum_{m=0}^{\infty} a_m^{1n} \frac{\left(\sqrt{\frac{4z_e^2}{D^2} + 1} - \frac{2z_e}{D} \right)^{2(m+1)}}{\sqrt{\frac{4z_e^2}{D^2} + 1}} = -i F_{ln,y}(z_e), \\ F_{ln,z}(z_e) &= -2\pi \delta_{l0} \sum_{m=1}^{\infty} a_m^{0n} \frac{\left(\sqrt{\frac{4z_e^2}{D^2} + 1} - \frac{2z_e}{D} \right)^{2m+1}}{\sqrt{\frac{4z_e^2}{D^2} + 1}}. \end{aligned} \quad (\text{A.14})$$

Also,

$$\boldsymbol{\zeta}_{ln} := \frac{\pi}{32} \delta_{|l|1} a_0^{1n} (\hat{\mathbf{x}} + \text{sgn}(l) i \hat{\mathbf{y}}) \quad (\text{A.15})$$

and

$$\mathbf{d}_{a,ind}(z_e, \omega) = \frac{\pi}{16} \sum_n \frac{a_0^{1n} F_{1n,x}(z_e)}{1/\eta_{1n} - 1/\eta(\omega)} [\mathbf{d}_a - (\mathbf{d}_a \cdot \hat{\mathbf{z}}) \hat{\mathbf{z}}], \quad (\text{A.16})$$

which gives us a straightforward way to compute the radiative and non-radiative contributions for the spontaneous emission rate in this situation. We point that it is clear from

these expressions that only the dipole modes ($l = 1$) contribute to the x and y Purcell factors and only the dark modes ($l = 0$) contribute to the z Purcell factor, which has a radiative part equal to 1.

Appendix B

List of publications during Ph. D. thesis work

- Y. Muniz, D. Szilard, W. J. M. Kort-Kamp, F. S. S. Rosa, and C. Farina, *Quantum two-photon emission in a photonic cavity*, Phys. Rev. A **100**, 023818 (2019)
- Y. Muniz, A. Manjavacas, C. Farina, D. A. R. Dalvit, and W. J. M. Kort-Kamp, *Two-photon spontaneous emission in atomically thin plasmonic nanostructures*, Phys. Rev. Lett. **125**, 033601 (2020).
- Y. Muniz, C. Farina, and W. J. M. Kort-Kamp, *Casimir forces in the flatland: Interplay between photoinduced phase transitions and quantum hall physics*, Phys. Rev. Research, **3**, 023061 (2021).
- Y. Muniz, P. Abrantes, L. Martín-Moreno, F. Pinheiro, C. Farina, and W. J. M. Kort-Kamp, *Entangled two-plasmon generation in carbon nanotubes and graphene coated wires*, Phys. Rev. B, **105**, 165412 (2022).